ENGINEERING OF CARBON ELECTRONIC DEVICES USING FOCUSED ELECTRON BEAM INDUCED DEPOSITION (FEBID) OF GRAPHITIC NANOJOINTS

A Dissertation
Presented to
The Academic Faculty

by

Songkil Kim

In Partial Fulfillment
of the Requirements for the Degree
Doctor of Philosophy in the
School of Mechanical Engineering

Georgia Institute of Technology
December, 2014

ENGINEERING OF CARBON ELECTRONIC DEVICES USING FOCUSED ELECTRON BEAM INDUCED DEPOSITION (FEBID) OF GRAPHITIC NANOJOINTS

Approved by:

Dr. Andrei G. Fedorov, Advisor
School of Mechanical Engineering
Georgia Institute of Technology

Dr. Satish Kumar
School of Mechanical Engineering
Georgia Institute of Technology

Dr. Vladimir V. Tsukruk
School of Materials Science and Engineering
Georgia Institute of Technology

Dr. Baratunde A. Cola
School of Mechanical Engineering
Georgia Institute of Technology

Dr. Seung Soon Jang
School of Materials Science and Engineering
Georgia Institute of Technology

Date Approved: November 10, 2014

ACKNOWLEDGEMENTS

First I would like to thank my family for their support and guidance in all my pursuits throughout my entire life. Second I would like to thank my advisor, Professor Fedorov, for being a mentor in my Ph.D study as well as in my life during the past five years.

Financial supports for this research have been provided by Semiconductor Research Corporation (GRC Contract 2011-OJ-2221), AFOSR BIONIC Center (Award No. FA9550-09-1-0162) and U.S. Department of Energy, Office of Basic Energy Sciences, Division of Materials Sciences and Engineering (Award Number DE-SC0010729).

TABLE OF CONTENTS

LIST OF FIGURES

SUMMARY

While carbon nanotubes (CNTs) and graphene show promise as unique electronic materials, large contact resistance between CNTs/graphene and metal has been a barrier preventing application of these materials to electronic devices. Focused Electron Beam Induced Deposition (FEBID) is an emerging chemical vapor deposition (CVD) method, which enables resist-free "direct-write" additive nanomanufacturing using a variety of materials with a high degree of spatial and time-domain control. FEBID offers a unique opportunity to engineer MWCNT/graphene-metal interfaces with nanoscale resolution. This thesis concerns development and characterization of the FEBID technique to improve interfacial properties at MWCNT/graphene-metal junctions by forming graphitic nanojoints using hydrocarbon precursors. A fabrication protocol for ultralow-resistant, Ohmic contacts at MWCNT-metal junctions with FEBID graphitic nanojoints was developed, based on an in-depth topological/ compositional/electrical material characterization, yielding high performance "end" contacts to multiple conducting channels of MWCNT interconnect. Using the FEBID technique as a contact fabrication tool, three fabrication strategies of electrical contacts between the mechanically exfoliated multilayer graphene and a metal interconnect using graphitic nanojoints were proposed and demonstrated experimentally, suggesting one of them, the post-deposited FEBID graphitic interlayer formation, as the most efficient strategy. A patterned CVD grown monolayer graphene, which is a promising material for large area graphene device fabrication, was contacted to metal electrodes through the FEBID graphitic interlayer, whose formation and chemical coupling to graphene and metal were theoretically and experimentally explored. The effects of FEBID process on the graphitic interlayer formation and graphene electronic devices were demonstrated through electrical measurements, including the transmission line method (TLM) measurements for separate evaluation of sheet and contact resistances. Modifications of the graphene channel as well as interfacial properties of the graphene-metal junctions were achieved, highlighting a

unique promise of the FEBID technique as a tool for enhancing chemical, thermo-mechanical, and electrical properties of graphene-metal interfaces along with controllable tuning of doping states of the graphene channel.

CHAPTER 1

INTRODUCTION

As the feature sizes of electronic devices decrease to nano-scale, copper resistivity increases due to electron scattering at the surface and grain boundaries, and wire type structures become more vulnerable to electromigration damage [1-4]. Alternative materials, such as carbon nanotubes (CNTs) and graphene are being explored owing to their unique electronic transport characteristics, as well as their excellent mechanical and thermal properties [4-9]. Graphene is a one-atom-thick planar sheet of sp^2-bonded carbon atoms densely packed into a 2D honeycomb lattice [7]. It can be wrapped up to 0-D fullerences, rolled to 1-D carbon nanotube, and stacked to 3-D graphite depending on edge geometries. Many studies have been performed to assess a potential of graphene/CNT-based materials and structures for nanoelectronic devices. However, several fundamental limitations still provide significant roadblocks to application of these materials to real device platforms [4].

International Technology Roadmap for Semiconductors (ITRS) identifies the main challenges for CNT and graphene applications to electronic devices [4]. Among them, the most significant challenge is a large electrical contact resistance between CNTs/graphene and metal electrodes. Recently, substantial progress has been made in assessing the contact resistance of metal contacts to single-walled CNTs (SWCNTs) [10,11]. It was found that contact resistance to a metallic SWCNT can be reduced down to the quantum limit (~6.5 kΩ) with the channel length scaled down to 15 nm [10]. Even with this notable achievement, there are still a number of competing factors that need to be considered and technical challenges to be overcome in order to achieve the superior electrical performance promised by the CNTs. These include selective growths of semiconducting and metallic SWCNTs, high density integration of SWCNT bundles and low-resistance contact fabrication connecting all the individual SWCNTs in the bundles [4].

One of compelling alternatives is to utilize a multi-walled CNT (MWCNT) as an interconnect link and to make connection to multiple conducting shells, acting as parallel conducting channels. However, it is challenging to connect multiple conducting shells of a MWCNT using standard metal deposition processes due to the limited control of directionality (in three dimensions) in a standard contact fabrication process using nanolithography followed by metal evaporation/sputtering [12,13]. Also, metal deposition using sputtering or evaporation only yields a physical contact (*i.e. via* weak van der Waals interactions) to the MWCNT, which results in an inefficient electronic coupling at the Fermi surface [14,15]. Theoretical calculations revealed that physical contact resistance between metal and an open end of a carbon nanotube is on the order of 3~4 kΩ, even for contamination-free interface [9,16]. Thus, alternative fabrication methods have been demonstrated for establishing chemical binding of multiple CNT shells to metal [12,13,17]. For example, a TEM-AFM combination with the piezomotor-driven nano-manipulator was utilized to precisely position an open end of a MWCNT in contact with a tungsten AFM tip; then, the MWCNT and the tip were fused by Joule heating to establish a multiple shell contact to the metal. Such a composite MWCNT-carbide-metal interface resulted in a very low contact resistance of 700 Ω [17]. Obviously, while yielding a high quality electrical contact, this technique is not amenable to the scalable fabrication of electronic devices and the contact area/geometry between a MWCNT and a metal tip is limited to whatever spontaneously forms in the course of an intense heat release at the contact junction with rather poor control over the final outcome.

For graphene, the contact resistance challenges are similar to that of CNTs. Physical contacts of metal to graphene by conventional metal deposition methods resulted in the contact resistivity of 2e-4 Ω-m with Au/Pd/Ti metal contacts [18]. In order to improve contact resistance, double contacts (both at the top and bottom surface) of metal to graphene were suggested, and 40% reduction of contact resistance was achieved compared to a single metal contact to graphene [19]. However, it still resulted in a contact resistivity of an order of 1e-4 Ω-m, which is much higher

than graphene's channel electrical resistivity. Theoretically, based on the density functional theory (DFT) calculations, the primary contribution to the contact resistance is the nature of the electronic coupling relying on the binding properties of the interface, as shown in Figure 1.1 [20,21]. Simulations suggest that the "end-contact" geometry should result in a significantly lower contact resistance than the "side-contact" geometry since the dangling bonds at the edges of MWCNT/graphene will form the covalent bonds to metal resulting in strong electronic coupling between MWCNT/graphene and metal electrodes. For example, Ti "end-contact" interface has 10 times higher binding energy and also 10 times lower contact resistance than the "side-contact" interface between the same materials.

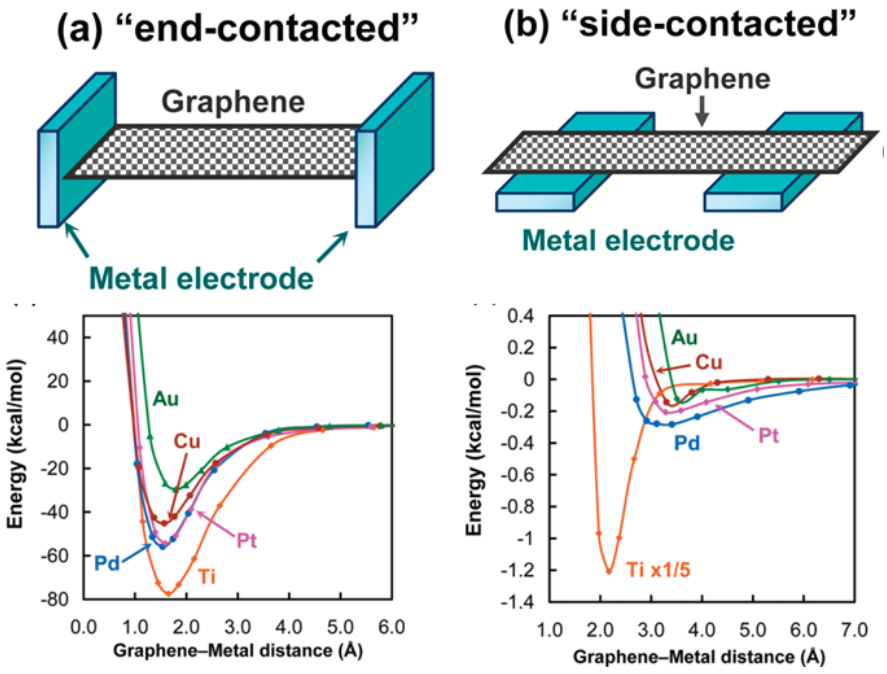

Figure 1.1. (a) End-contacted metal-graphene geometry resulting in chemical (strong coupling) contact and (b) side-contacted metal-graphene geometry having physical (weak coupling) contact, with the corresponding calculated binding properties between them. Reprinted from ref. 21.

However, the end contact is difficult to achieve experimentally using conventional metal deposition methods due to the limited control of directionality and the presence of hydrogen-

terminated edges of graphene, impeding chemical binding to metal. As a possible methodology to establish a highly reactive surface of graphene, oxygen plasma treatment was explored [22,23]. It was suggested that plasma treatments generated defects on graphene basal plane and enhanced the interaction between graphene and metal contacts. Yet, there are significant challenges with this method: 1) difficulty of process control (large un-controlled variation of contact electrical conductivity up to one order of magnitude), and 2) severe degradation of graphene quality due to plasma attack. Therefore, alternative techniques are still needed to reduce contact resistivity without any side-effects of the contact fabrication process on devices.

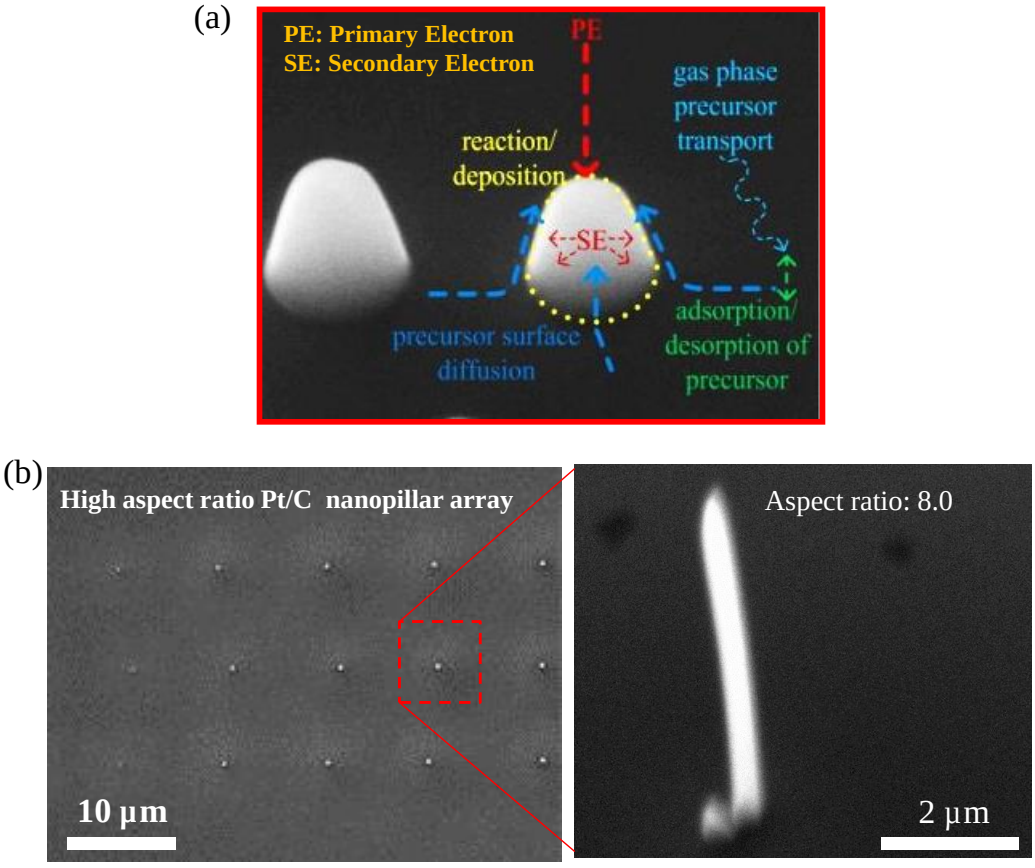

Figure 1.2. SEM images of (a) FEBID carbon nanopillar describing the deposition mechanism from gas phase precursor molecules and (b) Pt/C nanopillar arrays (top view) deposited using a gas injection system for flowing Pt precursor gas (Trimethyl(methylcyclopentadienyl)platinum, $C_5H_4CH_3Pt(CH_3)_3$) with the zoomed-in image of a Pt/C nanopillar (45 degree tilted view).

Focused electron beam induced deposition (FEBID) is an emerging chemical vapor deposition (CVD) method, enabling a resist-free 'direct-write' additive nanomanufacturing using a variety of precursor materials with a high degree of control [24,25]. It is a versatile tool for localized, high-resolution 3D nanofabrication [26,27], including electromechanical welding [28-30], plasmonic nanostructures [31], transistors [32], magnetic sensors [33], and nanocomposites [34]. Figure 1.2(a) demonstrates the deposition mechanism of a FEBID carbon nanopillar from gas phase molecules adsorbed on a base substrate. FEBID process makes a deposit from non-volatile residual species resulting from dissociation of adsorbed precursor molecules by low-energy secondary electrons, which are generated by high energy, primary electrons of the focused beam upon interactions with a substrate [24-27]. Using a gas injection system for feeding various precursor sources into the SEM chamber, high aspect ratio solid nanostructures can be grown at a much faster growth rate, as shown in Figure 1.2(b).

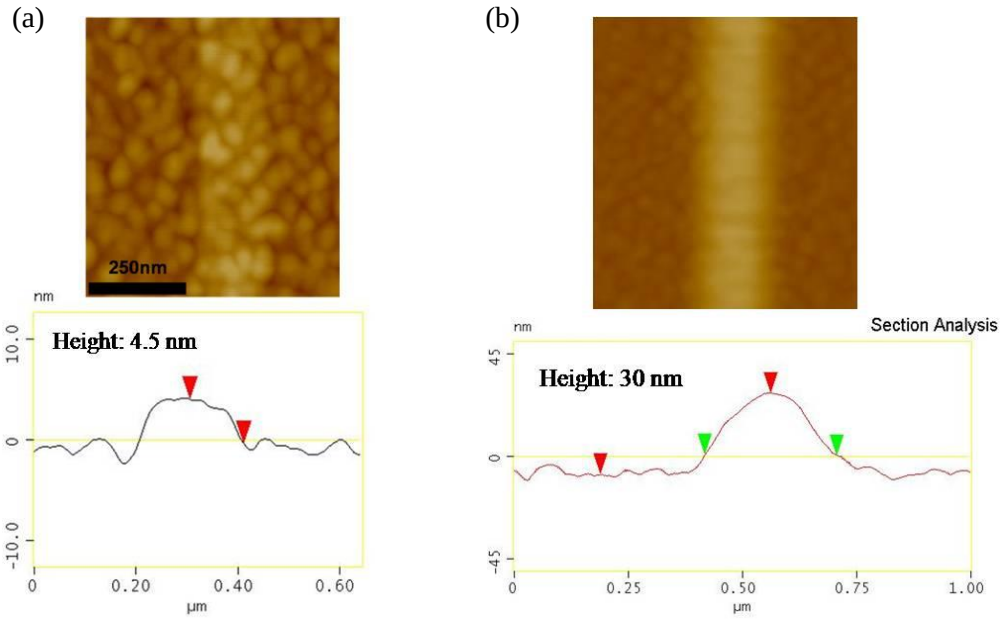

Figure 1.3. AFM images and cross-sectional profiles for FEBID-made carbon line on a copper substrate with deposition time of (a) 30 seconds and (b) 5 minutes, showing an excellent wettability of the carbon-Cu pair.

In the previous work [29], our group has developed a contact fabrication method using focused electron beam induced deposition (FEBID) for the MWCNT-metal interconnect. It has two main advantages for fabricating contact interface between the MWCNT/graphene and metal interconnect. First, it allows the use of a variety of materials for forming a contact junction [35]. Of particular interest here is carbon deposition using readily available hydrocarbon precursors. Carbon is superior as an interfacial material in that an intrinsic resistance of the contact to the MWCNT/graphene can be made negligibly small (for very thin interfacial films) since carbon has good wettability to a MWCNT/graphene [30,36]. Figure 1.3 shows an AFM image and cross-sectional profile of a thin FEBID-made carbon line on a copper substrate. It shows a smooth and continuous interface between the copper substrate and the carbon deposit, indicative of excellent wettability. Second, the MWCNT/graphene-carbon-metal junction should have Ohmic behavior due to similarity of work functions for all three materials involved in forming the junction [14,36,37]. Lastly, deposition of the contact material is precisely controlled (both the rate of growth and the resulting 3D shape) by changing the electron beam current and accelerating voltage [26,29,38] and moving the sample stage. It enables a high degree of 3D control to form both the ‘end-contact’ and ‘side-contact’ interfaces to MWCNT or graphene.

In this thesis research, the overarching goal is to develop and characterize the fabrication protocols for reducing electrical contact resistance through chemical contacts by FEBID graphitic carbon nanostructures at the MWCNT/graphene and metal interfaces. The research is divided into two interrelated themes, one is focusing on MWCNT-metal interface and another one is on FEBID of graphene devices, as shown in Figure 1.4.

In Chapter 2, the fabrication protocol for utility of FEBID graphitic nanojoints is developed for both of the ‘side’ and ‘end’ contacts of MWCNTs to metal electrodes, supported by in-depth topological, compositional and electrical characterizations of the MWCNT-metal interconnect with FEBID graphitic nanojoints. In Chapter 3, application of FEBID is extended to mechanically exfoliated multi-layer graphene-metal interconnects in order to reduce contact resistance at the

graphene-metal junction. Three fabrication protocols for FEBID graphitic nanojoint formation at the junction ('overlayer', 'pre-deposited' and 'post-deposited' interlayers) are developed and characterized, suggesting that 'post-deposited' FEBID carbon interlayer formation is the most reliable/efficient protocol for improving interfacial properties between graphene and metal electrodes. In Chapter 4, a transfer procedure of a CVD monolayer graphene film from Cu foil to a dielectric substrate is optimized in order to minimize defects, wrinkles and cracks of the film and resultantly to fabricate high-performance graphene devices. Next, for in-depth understanding of FEBID utility in CVD monolayer graphene electronic devices, the nature of coupling of the two possible FEBID carbon deposits ('intended' FEBID graphitic interlayer vs. 'unintentional' parasitic carbon contamination) with graphene is theoretically and experimentally explored, complemented by developing a technique for removing parasitic carbon. In Chapter 5, FEBID graphitic interlayer formation is analyzed using comprehensive material characterization *via* the AFM and Raman studies of graphene-metal interfaces modified by FEBID processing. Lastly, electrical characterization of graphene electronic devices is performed, demonstrating the significant improvement of interfacial properties of the graphene-metal junctions achieved with FEBID graphitic interlayer formation.

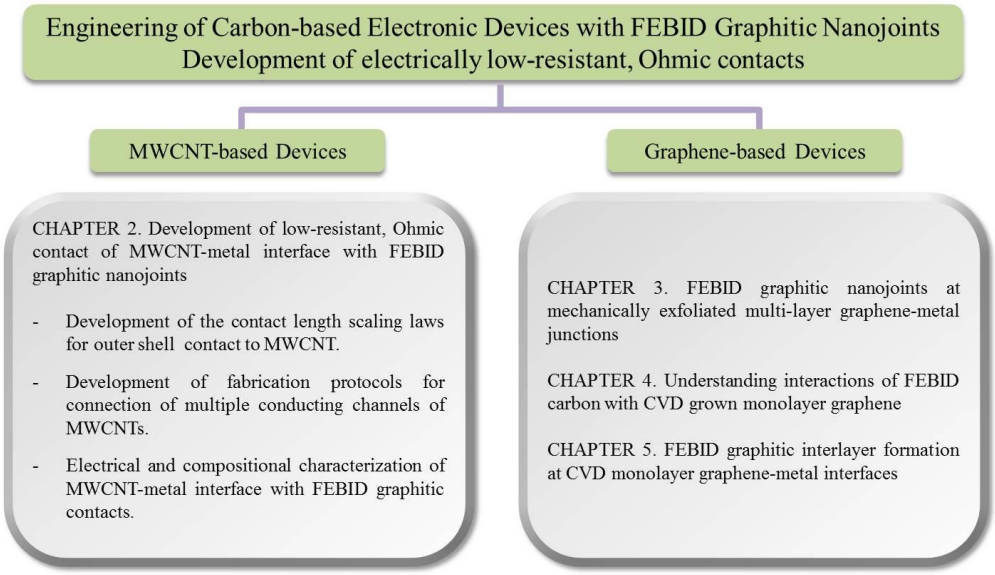

Figure 1.4. Overview of the Ph.D dissertation research.

CHAPTER 2

DEVELOPMENT OF LOW-RESISTANT, OHMIC CONTACT OF MWCNT-METAL INTERFACE WITH FEBID GRAPHITIC NANOJOINTS

2.1 Introduction

Multi-walled CNTs (MWCNTs) are promising candidates for replacement of copper-based interconnects in electronic devices [4]. One of main challenges, impeding interconnect application of MWCNTs, is a large contact resistance to the metal electrodes, which is due to metal contacting to only the outershell of the tubes with weak electronic coupling [12,13,15,39]. In order to reduce the contact resistance as well as the tube channel resistance, connection to multiple conducting shells, acting as parallel conducting channels must be made. However, it is fundamentally difficult to connect multiple conducting shells of a MWCNT using standard metal deposition processes due to the limited control of directionality (in three dimensions) in a standard contact fabrication process [12,13].

Alternative fabrication methods have been demonstrated for establishing chemical binding of multiple CNT shells to metal, such as using a piezomotor-driven nano-manipulator to precisely place the open end of a tube in contact to the metal junction and fuse the contact interface *via* Ohmic heating [12,13,17]. However, this technique is not amenable to the scalable fabrication of electronic devices and the contact area/geometry between a MWCNT and a metal tip is limited to whatever spontaneously forms in the course of an intense heat release at the contact junction with a rather poor control over the final outcome. On the contrary, FEBID is a technique in which a focused electron beam facilitates a CVD process with high degree of spatial and time-domain control [29,40], which enables one to provide the deposit's access to multiple shells. Moreover, this technique can be applied to scalable fabrication of actual multi-interconnect devices by using

a multi-beam system [41] in conjunction with controllable alignment of MWCNTs on prefabricated electrodes.

In this Chapter, we aim to accomplish several objectives: 1) to fabricate FEBID carbon contacts to the outermost shell of a MWCNT in order to understand the geometric effects on the contact resistances and to develop the contact size-dependent scaling laws; 2) to critically evaluate and optimize the FEBID deposit annealing technique to improve electrical conductivity of the carbon contacts; and 3) most importantly, experimentally demonstrate a new fabrication protocol for making connection to multiple shells of the MWCNTs, which yields an ultra-low-resistance Ohmic contact between a MWCNT and metal electrodes. These FEBID and post-deposition advances are supplemented with innovations in other enabling processing steps, such as a controlled assembly/alignment of multiple MWCNTs onto an array of metal electrodes.

2.2 FEBID graphitic nanojoints to the outer shell of MWCNT

2.2.1 Length scaling law for the magnitude of the outer shell contact resistance to MWCNT

In two-point measurements using a setup schematically shown in Figure 2.1(a), total resistance of a MWCNT-metal interconnect with FEBID carbon nanojoints includes several contributions [29],

$$R_{tot} \approx 2R_{aC} + 2R_{aC-metal} + 2R_{aC-MWCNT} + R_{MWCNT} \quad (1)$$

Here, R_{aC} is a resistance of a FEBID carbon nanojoint, $R_{aC\text{-}metal}$ is a resistance of a FEBID carbon nanojoint-metal interface, $R_{aC\text{-}MWCNT}$ is a resistance of a FEBID carbon nanojoint-MWCNT interface, and R_{MWCNT} is a resistance of a MWCNT itself. The components of total resistance in eq. (1) can be expressed in terms of relevant dimensions and intrinsic electrical conductivities of the materials.

$$R_{tot} \approx \frac{2}{L_c}\left(\frac{\rho_{aC}L_1}{L_2} + \frac{\sigma_{aC-metal}}{L_2} + \frac{\sigma_{aC-MWCNT}}{\pi d_{MWCNT}}\right) + R_{MWCNT} \quad (2)$$

Here, ρ_{aC} is the resistivity (Ω-m) of the amorphous FEBID carbon as deposited, $\sigma_{aC\text{-}metal}$ is an interfacial area resistivity (Ω-m^2) between the carbon contact and the metal electrode, $\sigma_{aC\text{-}MWCNT}$ is an interfacial area resistivity (Ω-m^2) between the carbon contact and an outermost shell of a MWCNT, and all the dimensions are described in Figure 2.1(b). Eq. (2) indicates that an interconnect resistance is inversely proportional to a contact length (L_c) of carbon interface to a MWCNT, and asymptotically approaches to the intrinsic resistance of a MWCNT itself in the limit of an ideal contact. The resistance of defect-free MWCNTs can be evaluated by eq. (3) for an outermost shell contact only [10,42].

$$R_{MWCNT} = \frac{h}{2\overline{N}e^2}\left(1 + \frac{L_{ch}}{L_{mfp}}\right) \tag{3}$$

where $h/2e^2$~12.9 kΩ, $\overline{N}$ is the average number of conducting channels in one shell [42], L_{ch} is a channel length of a MWCNT, and L_{mfp} is the mean free path of an electron approximated to be about a factor of a thousand of the CNT diameter [29,42,43].

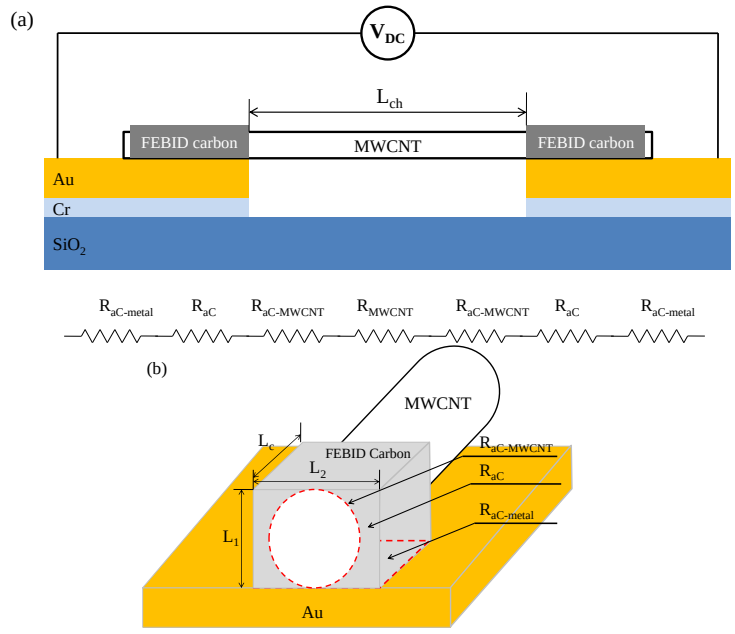

Figure 2.1. Schematics of (a) the device structure and the experimental setup for two-point electrical measurements, and (b) geometry of an FEBID carbon contact and contributing resistances to the overall contact resistance.

To verify the validity of the eq. (2) scaling law, a single MWCNT-metal interconnect was fabricated as shown in Figure 2.2(a). A single MWCNT with a diameter of ~30 nm was first aligned between two ~150 nm thick Au/Cr electrodes using dielectrophoresis (DEP). Next, a series of rectangular-shaped FEBID carbon deposits were fabricated atop of the outermost shell of the MWCNT, electrically and mechanically connecting the tube to the metal electrodes as shown in Figure 2.2(b). For FEBID carbon deposition, Quanta 200 ESEM (FEI, Inc.) operated under ~ 10^{-6} Torr was employed with 'NPGS' (Nanometer Pattern Generation System) software. The electron beam conditions used for the deposition were set to a spot 5 (e-beam current~400 pA) and the beam energy of 25 keV. Residual hydrocarbons adsorbed on substrates were used as a precursor for FEBID of carbon material.

Electrical measurements were conducted by a two-terminal method in vacuum upon a series of pair-wise depositions of FEBID carbon contacts at the MWCNT-metal interfaces. The voltage bias was applied using SRC Model DS345 30 MHz function generator, and the current was collected using Keithley 6485 Picoammeter. The low voltage bias ranging from 0 mV to 80 mV was applied to avoid Joule heating induced damage of the nanotube. Before FEBID carbon contacts, the total resistance of the MWCNT-metal interconnect was measured as ~ 1 GΩ due to high contact resistance ('line' contact of the MWCNT to the electrodes) between them, while the resistance of an ideal MWCNT can be estimated, using eq. (3), to be ~3.75 kΩ for the aligned MWCNT with a diameter of 30 nm and a channel length of 2 μm.

Upon a series of pair-wise depositions of the FEBID carbon contacts on both ends, the I-V measurements for the resulting interconnect were performed. All I-V curves were linear as shown in Figure 2.2(c), indicating an Ohmic contact, which allows computation of the total interconnect resistance from the slope. A contact length for each deposit pair was defined as an average value for two contacts to metal electrodes on both ends. As shown in Figure 2.2(d), after the 1st set of the FEBID carbon contacts (L_c~300 nm), the total resistance dropped to ~3.5 MΩ, which is a reduction of ~ 3 orders of the magnitude as compared to the resistance before FEBID contacts.

Increasing the contact length (L_c) by sequential deposition resulted in the continuous reduction of the total resistance, until it saturated at ~ 1.2 MΩ for over L_c~1.1 µm. These experimental results confirmed the validity of the length scaling law in eq. (2) that the total resistance is inversely proportional to the contact length (L_c) between carbon contacts and MWCNT, *i.e.*, $R_{tot}=P_1/L_c+P_2$, with P_1 denoting the resistivity of contact interfaces and P_2 is a MWCNT channel resistance. By fitting the experimental data to this scaling law, the resistivity (P_1) is found to be ~ 1.0 Ω-m, due to a low electrical conductivity of as-deposited hydrogenated, amorphous FEBID carbon [3,12,22].

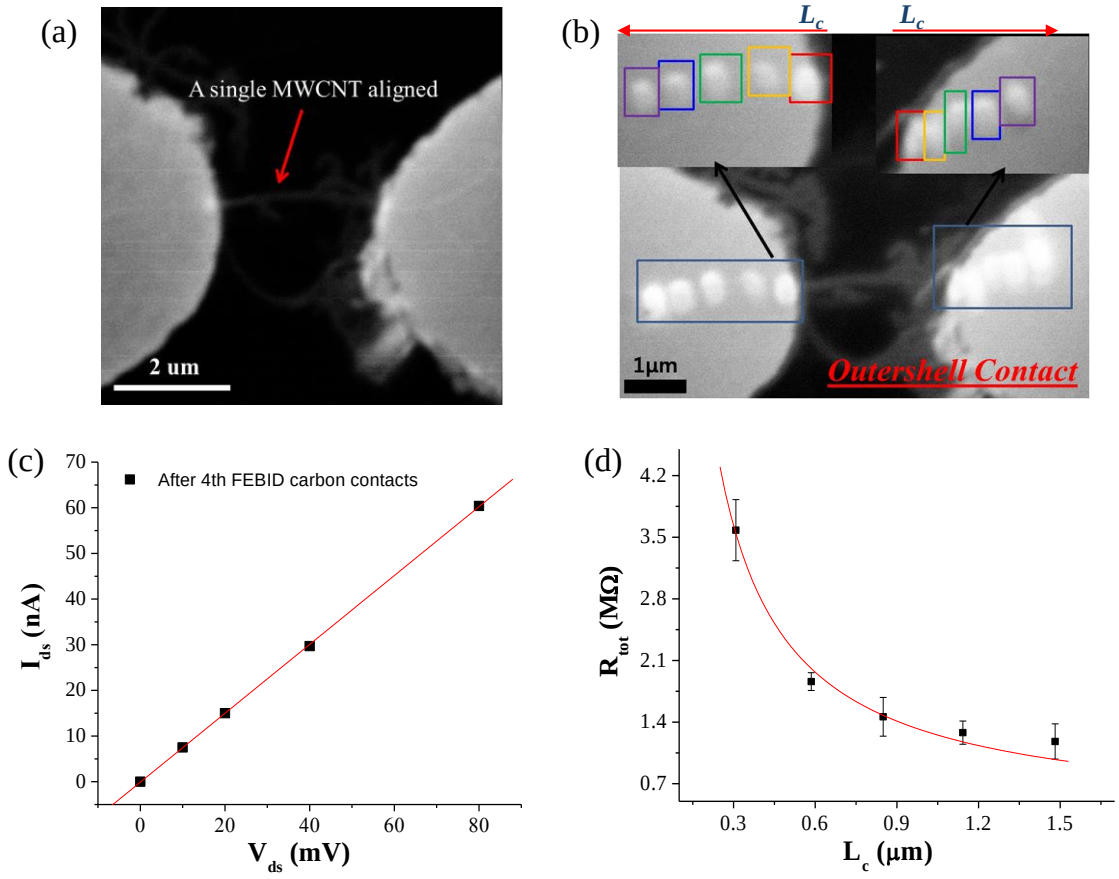

Figure 2.2. (a) A single MWCNT with a diameter of ~30 nm and the length of ~ 2 µm aligned between two electrodes using dielectrophoresis (DEP), (b) a series of FEBID-made carbon contacts to the outer shell of MWCNT, (c) I-V curve after 4th contact-pair fabrication showing linear Ohmic behavior, and (d) the overall interconnect resistance R_{tot} measurement with

increasing the contact length L_c by sequential pair-wise deposition of carbon squares on both ends of a MWCNT demonstrates $R_{tot} \sim P_1/L_c + P_2$ and suggests a need to decrease the intrinsic resistivity (P_1) of the contacts by graphitization of FEBID carbon, along with minimizing the channel resistance of a MWCNT (P_2).

2.2.2 Graphitization of FEBID carbon contacts for low contact resistances

To increase conductivity of FEBID carbon contacts, we graphitized the amorphous FEBID carbon deposits using Joule-heating-induced annealing in vacuum by passing an electric current through a MWCNT interconnect with FEBID-deposited contacts displayed in Figure 2.2(b). As shown in Figure 2.3(a), the total resistance was reduced by an order of magnitude from 1.1 MΩ to 0.18 MΩ due to graphitization of the FEBID carbon contacts. Further increase in the bias voltage beyond 2 V (*i.e.*, higher annealing currents) to stimulate further annealing of the contacts yielded a negative result with the total resistance starting to increase to 230 kΩ, likely due to thermo-mechanical damage of the MWCNT upon excessive Joule heating [44,45].

In order to understand the composition of the carbon deposits, Raman measurement was conducted (Figure 2.3(b)) using a WITec (Alpha 300R) confocal Raman microscope using an Ar+ ion laser (514.5 nm) under minimal laser power (<1 mW) to avoid any laser induced annealing. The Raman data were integrated between 1000 cm^{-1} and 1800 cnm^{-1} to see the D-band and G-band. Lorentzian peak fitting was applied to Raman data in order to obtain G-band and D-band peak positions and D/G peak area ratio. The G-peak position and D/G area ratio are 1575.4 cm^{-1} and 1.95, respectively, suggesting the partially graphitic nature of the FEBID carbon deposits after annealing. The fully graphitized structure resulting from annealing hydrogenated amorphous carbon is known as a nanocrystalline graphite, which has a G-peak position of around 1600 cm^{-1} and D/G ratio of around 2.5 [46]. This supports our observation that damage of the MWCNT due to Joule heating is the most likely cause of an

increase of the overall interconnect resistance before the FEBID carbon contacts can be fully graphitized.

Annealing by Joule heating is rather difficult to control without inducing a parasitic thermo-mechanical damage of the MWCNT, owing to the fact that the resistance of the carbon continuously decreases as it undergoes phase transformation, which results in an increase in the current (and thus heat release). As an alternative, which offers a significantly greater control, we performed thermal annealing in a controlled-environment furnace to avoid any physical damage of the tubes. It is known that FEBID nano-sized carbon deposits start to graphitize at much lower (~350 ℃) than the bulk carbon phase-transition temperature, and formation of a highly densified graphitic deposit (nanocrystalline graphite) occurs at around 450 ℃ in an environmental furnace [46]. Thus, to fully graphitize the FEBID carbon contact, one needs to increase the annealing temperature to 450℃, but the MWCNTs begin to oxidize around this temperature [47]. To avoid the oxidation of MWCNT, we annealed the contacts at 350 ℃ in an environmental furnace, which is the threshold temperature of graphitization of FEBID carbon nanostructures. It is worth to note that there are two contributing factors in determining the carbon structure after an annealing process; a base substrate as a site for a nucleation of the graphitic crystallites and an interfacial area between the FEBID carbon structure and the metal substrate [46]. The optimized annealing temperature in the literature was determined for carbon dot and line deposits on Au/Cr substrate [46]. Presence of MWCNTs beneath the FEBID carbon structure can have an influence on lowering the graphitization threshold temperature and defining a preferred (CNT-like) phase that the carbon accepts upon annealing.

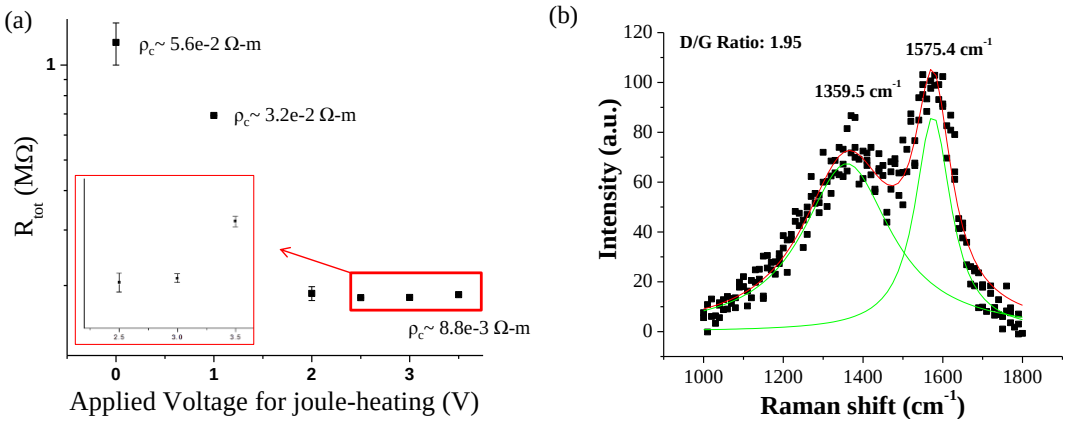

Figure 2.3. (a) Joule-heating-induced annealing of the carbon contacts significantly reduces the total interconnect resistance by graphitization. (b) Raman spectrum of FEBID carbon contacts after Joule-heating-induced annealing, which indicates the partially-graphitized structure of the contacts.

To minimize the influence of the MWCNT resistance on the total interconnect resistance, we utilized a larger diameter MWCNT from a commercial vendor [48], which was fabricated by the arc discharge method. It has a diameter of 75 nm and the channel length of around 2 µm, as shown in Figure 2.4(a), with its outermost shell resistance computed to be about 1.5 kΩ by eq. (3) when it is defect-free. We fabricated square-like carbon contacts on both ends of a tube (insets of Figure 2.4(a)) to establish a contact between the outermost shell of the MWCNT and the metal electrodes. Initially (before FEBID carbon contact deposition) when an isolated MWCNT was aligned between two metal electrodes, the total interconnect resistance was ~1 GΩ. After deposition of the FEBID carbon contacts at the ends of a MWCNT, the resistance dropped significantly down to 13 MΩ. Thermal annealing at 350 ℃ for 30 min in an ambient environment furnace resulted in further reduction of the total interconnect resistance to 26.5 kΩ. This indicates that the contact resistance is at least below 25 kΩ, which is the resistance after subtracting that of the ideal tube itself from the total measured resistance, and it is likely to be much lower due to intrinsic defects in the MWCNT and also because of the presence of kinks further reducing electrical conductance of the tube [49].

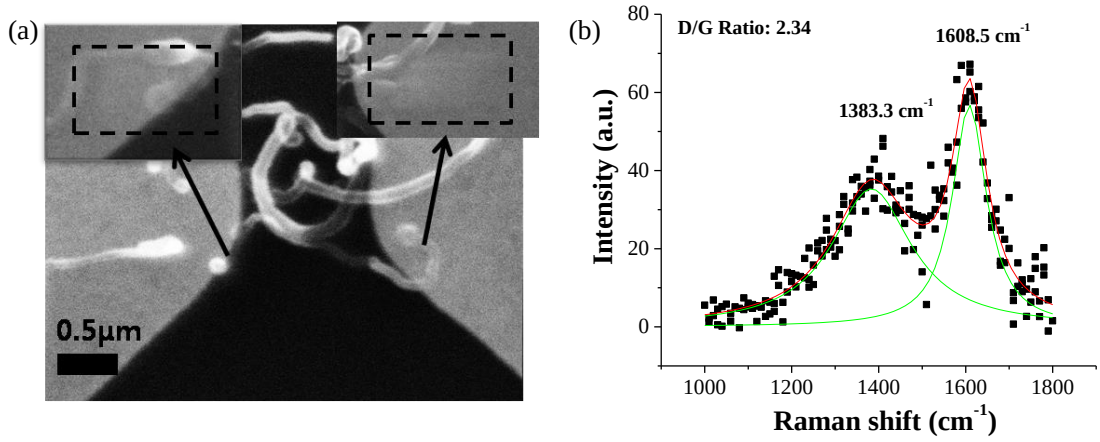

Figure 2.4. (a) FEBID-made carbon contacts (magnified in the insets) to an outermost shell of a larger diameter of a MWCNT (D_{cnt}~75 nm) yielding the total resistance of 26.5 kΩ after thermal annealing at 350 ^{o}C for 30 min, and (b) Raman spectrum indicating the carbon contacts are fully graphitized after the thermal annealing process at 350 ^{o}C for 30 min.

The composition of the FEBID carbon contacts was evaluated using Raman spectroscopy. As shown in Figure 2.4(b), the G-peak position and D/G ratio reveal that the contact has characteristics of a nanocrystalline graphite, suggesting that graphitization of the FEBID carbon structure can be achieved at a much lower annealing temperature in the presence of MWCNTs than in the case of the plain metal substrate [46]. It should be mentioned that all electrical measurements were performed with low bias (0-80 mV) voltage to avoid accidental Joule-heating induced damage of the tube.

2.3 Development and evaluation of a fabrication protocol for connecting multiple conducting channels of MWCNTs

2.3.1 Preparation of open ended MWCNTs

A dense forest of MWCNTs with a diameter ranging from 10 to 35 nm was grown using a conventional chemical vapor deposition (CVD) method on a silicon substrate, as shown in Figure 2.5(a). Initially, capped ends of MWCNTs need to be opened up to expose all shells for making

the contacts to metal electrodes. Thus, the forest of MWCNTs was subjected to an Argon plasma treatment in order to mechanically etch away the end-caps of MWCNTs [50]. After an exposure for 30 min, the length of the MWCNTs reduced from 18 µm to 10 µm, which indicates successful plasma etch resulting in opening the ends of MWCNTs. Interestingly, as shown in the Raman spectra for the MWCNT forests, Figure 2.5(c) and 2.5(d), the quality of the tubes slightly improved after the plasma treatment due to a positive "side-effect" of the amorphous carbon layer removal. The etched MWCNTs were subsequently released from the substrate by mechanical stripping and were dispersed in dimethylformamide (DMF) with the assistance of mild ultrasonication. This process further breaks the MWCNTs along their lengths and results in a solution containing primarily open-ended MWCNTs of shorter length (< 8 µm).

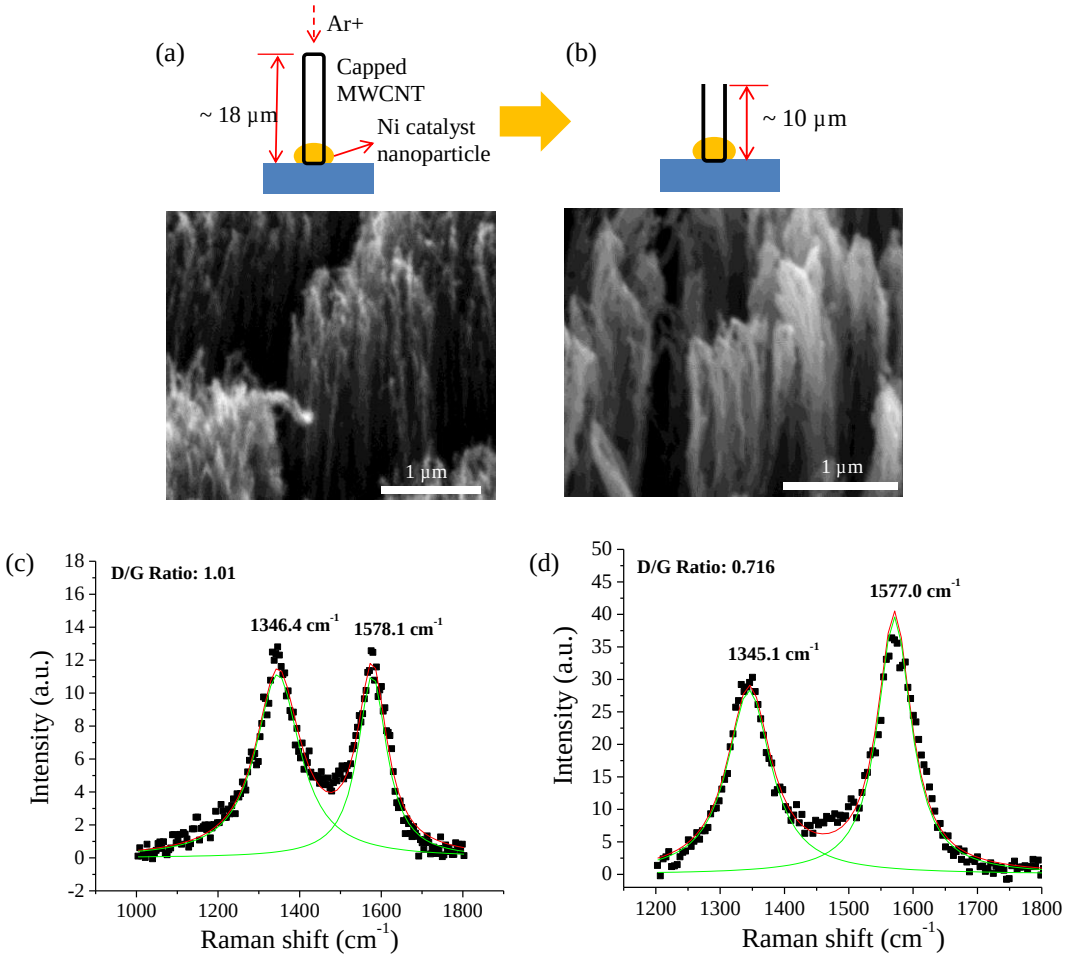

Figure 2.5. SEM images and Raman analysis results for MWCNT forests (a) before and (b) after Ar^+ etching to open one end of the capped MWCNTs. The averaged height of the forests reduced from ~18 µm to ~10 µm, indicating that one end of the tubes were etched away to be opened.

2.3.2 Fabrication protocol for connecting multiple conducting channels of open ended MWCNTs

A robust fabrication protocol has been developed for connection of multiple conducting channels of MWCNTs to metal electrodes with the FEBID graphitic nanojoints. As illustrated in Figure 2.6, the fabrication protocol consists of four steps. As explained in section 2.3.1, one end of the CVD grown vertically aligned MWCNTs was firstly opened up using Ar plasma etching so that multiple conducting shells of MWCNTs were exposed for making connection by FEBID carbon nanojoints. MWCNTs were further broken down into small pieces by releasing MWCNTs from the substrate and dispersing in dimethylformamide (DMF) by ultrasonication, thus opening the other end of MWCNT. After aligning open-ended MWCNTs onto the prefabricated metal interconnect test structure using dielectrophoresis (DEP), FEBID carbon nanojoints were made using the process shown in Figure 2.6(b), connecting multiple conducting channels/shells of MWCNTs to the metal electrodes.

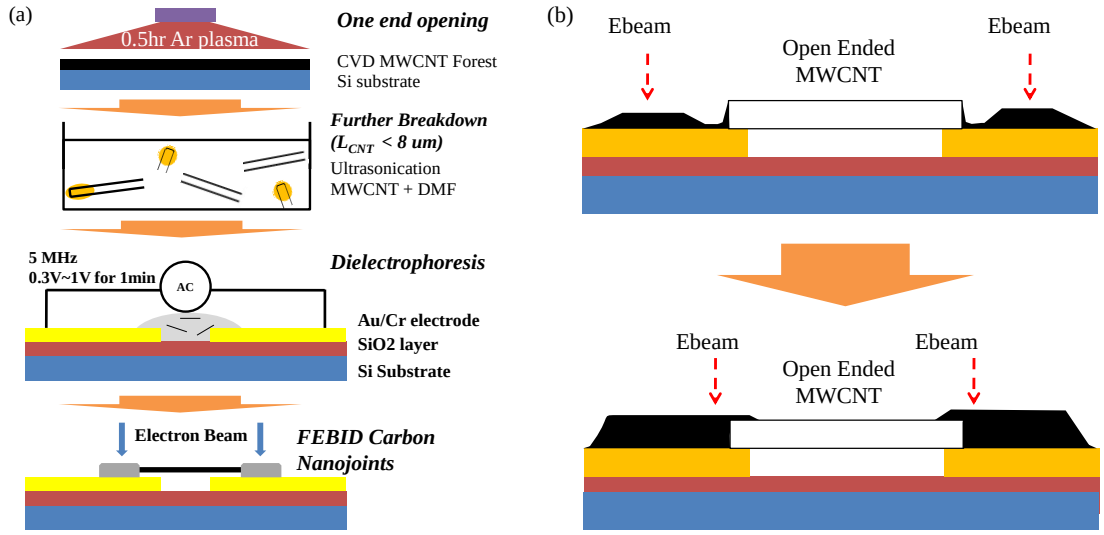

Figure. 2.6. Schematics of fabrication protocol of an ultra-low-resistant MWCNT-metal interconnect via FEBID graphitic nanojoints, including (a) complete sequence of process steps, and (b) details of FEBID graphitic nanojoint fabrication resulting in connection of multiple conducting shells of MWCNT to metal electrodes to form high electric performance interconnect link.

2.4. Establishment of an ultra-low interfacial resistance *via* graphitization of FEBID nanojoints

Using the fabrication protocol as described in the previous section, an ultra-low resistant MWCNT-metal interconnect with FEBID graphitic nanojoints was produced as shown in Figures 2.7(a). Initial composition of FEBID carbon nanojoints is known to be hydrogenated amorphous structure which has high electrical resistivity of an order of 10^3 Ω-m [51,52]. In order to graphitize the FEBID carbon nanojoints, thermal annealing was performed at 350 ˚C followed by two-terminal electrical measurements. Figure 2.7(b) shows the reduction of the device resistance upon increasing the annealing time for graphitization of FEBID carbon deposits. Forming the FEBID amorphous carbon nanojoints increases contact area between the MWCNT and metal electrode, leading to four order of magnitude reduction of electrical resistance from 1 GΩ to 300 kΩ. Upon thermal annealing, the FEBID amorphous carbon nanojoints are graphitized and

densified, increasing their conductivity and connecting metal electrodes to the multiple conducting channels of MWCNT. Initial 10 min annealing significantly reduced the resistance to 1.4 kΩ, almost three times lower than that (~3.8 kΩ) to the outermost shell of the tube alone. This indicates that the multiple shells of the tube are connected *via* the FEBID carbon contacts. Further thermal annealing for additional 20-25 min ultimately reduced the total interconnect resistance to (116.0±0.1) Ω, which is 10^7 times smaller than without FEBID graphitic nanojoints [30].

Figure 2.7(c) shows a representative Raman spectrum of the FEBID carbon nanojoints after thermal annealing for 40 min. In Raman spectrum of carbon structures, D peak corresponds to the breathing mode of sp^2 sites in rings and G-band relates to the stretching vibration of any pair of sp^2 sites in chains or aromatic rings [46,53]. In case of amorphous carbon structures, the D-mode stretch is proportional to the probability of finding a six-fold ring in the cluster, which in turn is proportional to the cluster area. Thus, the development of the D peak indicates ordering of carbon atoms into the sp^2-like networks [53]. Also, the D/G area ratio is known to be a quantitative factor in determining the size of graphitic crystallites in any carbon structure [46]. It is accepted that the increase in the D/G ratio corresponds to the increase in the correlation length of the graphitic crystallites. It was shown that the D/G ratio for carbon materials varies between 0 (100% amorphous carbon) and 2.5 (fully nanocrystalline graphite) [46,53]. In the measured Raman spectrum in Figure 2.7(c), G-band and D-band peak positions and their area ratio (D/G) of the FEBID carbon nanojoints indicate the characteristics of nanocrystalline graphite whose electrical resistivity is on the order of 10^{-6} Ω-m [51]. The inset of Figure 2.7(c) shows the Raman mapping of graphitic contact structures with bright domains corresponding to the highest (graphitic) G-band peak areas.

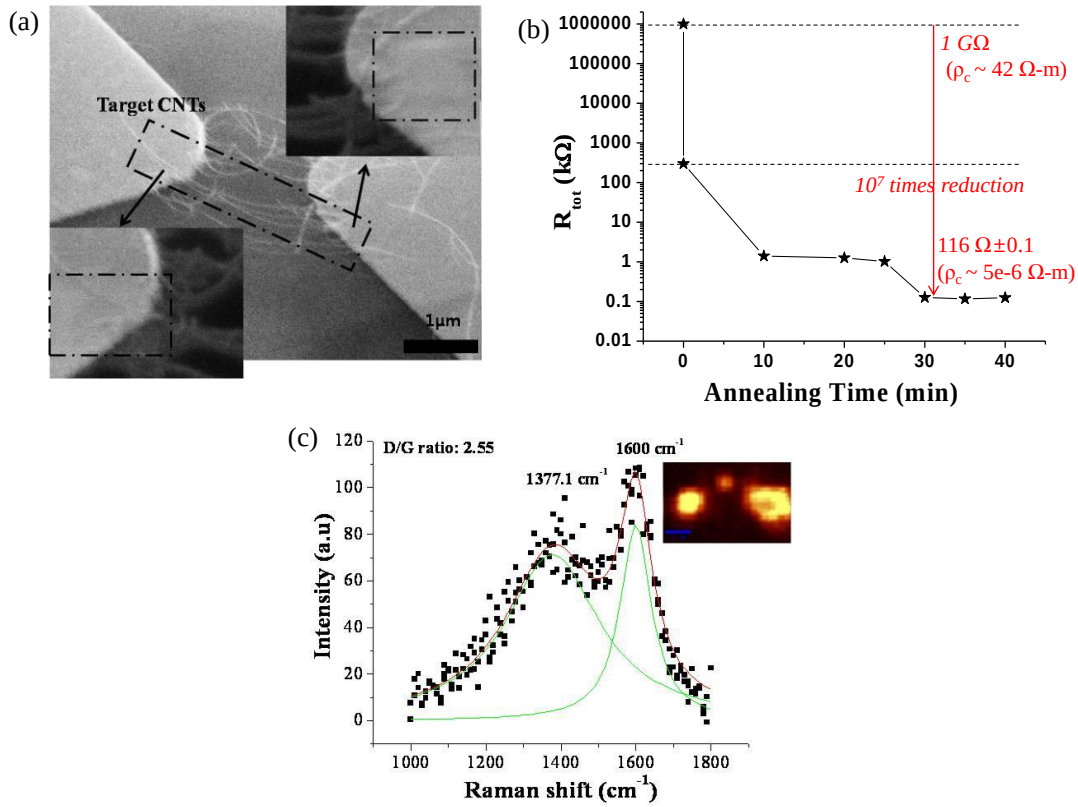

Figure 2.7. (a) SEM image of MWCNT-metal interconnect with FEBID graphitic nanojoints (insets), (b) electrical measurements-three stages of reduction of the overall interconnect resistance with FEBID carbon nanojoint fabrication and subsequent annealing, and (c) Raman spectrum of FEBID graphitic nanojoints indicating the characteristics of nanocrystalline graphite with the inset showing a Raman map of FEBID graphitic contact interface indicating that the deposits are fully graphitized.

2.5 Concluding remarks

In summary, we demonstrated a capability of graphitized FEBID carbon to produce a low-resistance Ohmic contact to multiple shells of MWCNT in the context of making high-performance electrical interconnect structures for the next generation electronic circuits. The carbon contact shape and size effect on the MWCNT-metal interconnect performance were evaluated along with other contributing factors, such as the phase composition of the carbon joint and the MWCNT channel conductance. The low (350 ℃) temperature annealing technique for graphitizing initially hydrogenated amorphous FEBID carbon contacts in the presence of

MWCNT, acting as a preferred phase nucleation site, was demonstrated allowing significant reduction of the contact resistance without damaging carbon nanotubes. Ultimately, a fabrication protocol for making an FEBID carbon connection to the multiple inner shells of a MWCNT was developed, resulting in an experimentally demonstrated contact resistance down to 116 Ω.

CHAPTER 3

FEBID GRAPHITIC NANOJOINTS AT MECHANICALLY EXFOLIATED MULTI-LAYER GRAPHENE-METAL JUNCTIONS

3.1 Introduction

Extensive investigations of graphene-metal interfaces have been performed both theoretically and experimentally in the past decade [6,7,18-23]. Based on the literature review, it can be concluded that the intrinsic contact resistance depends on electronic coupling at graphene and metal interfaces, which is defined by the binding properties (*i.e.* physical/van der Waals vs. chemical/covalent bonding). Among possible contact metals, Ti was found to be the best candidate featuring the lowest Ohmic contact resistance with strong binding energy of -6 kcal/mol for the "side-contact" and -80 kcal/mol for the "end-contact" interface to graphene [21].

In order to understand how FEBID carbon interacts with graphene, FEBID processing of a methane molecule on a graphene basal plane was modeled by sequentially removing a hydrogen atom ('dissociation') and optimizing graphene structure with FEBID intermediate species ('adsorption'), using density functional theory (DFT) calculation. DFT is a well-developed quantum mechanics simulation tool for atomistic understanding of molecular interactions of materials, such as binding and electronic properties [16,20,21]. As shown in Figure 3.1, electron beam induced deposition of each intermediate (CH_3, CH_2, CH, C) establishes strong chemical binding to the basal plane ('side-contact') of graphene with modification of the graphene's atomic structure. For example, FEBID carbon deposition on graphene yields the binding energy of -55.35 kcal/mol, which is much stronger than that of the 'side-contact' of Ti to graphene and comparable to that of the 'end-contact' of Ti to graphene. This result implies that FEBID carbon contact should help improve contact interface between graphene and metal electrodes.

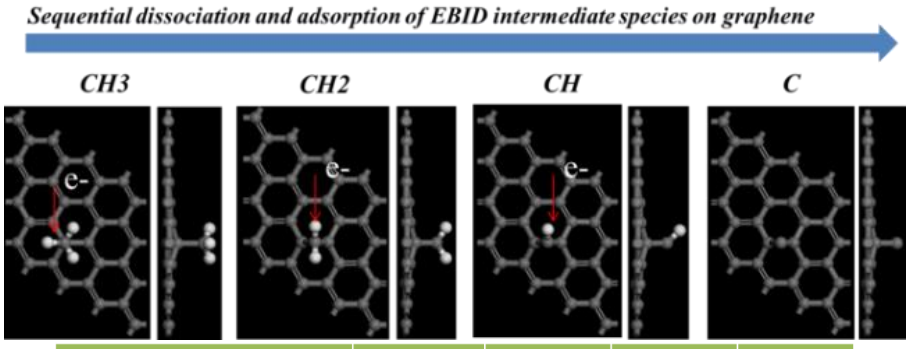

Species	CH3	CH2	CH	C
Binding Distance (A)	1.58	1.29	1.23	1.31
Binding Energy (kcal/mol)	-42.6	-98.1	-64.5	-55.35

Figure 3.1. DFT simulation results for focused electron beam induced sequential dissociation and adsorption of FEBID radical intermediates on the basal plane of graphene. The table shows the binding properties for each intermediate radical and graphene.

3.2 Fabrication protocols for FEBID graphitic nanojoints at the graphene-metal heterogeneous junctions

We have extended application of FEBID to making graphene-metal interconnects in order to reduce contact resistance at the graphene-metal interface. Three fabrication protocols for forming a multilayer (ML) graphene-metal interconnect *via* FEBID 'overlayer' (Device structure I), "post-deposited" (Device structure II) and "pre-deposited" (Device structure III) 'interlayers' were developed, as described in Figure 3.2. ML graphene was obtained by mechanical exfoliation from highly ordered pyrolytic graphite (HOPG) using a scotch tape on SiO_2 (90 nm)/Si substrate.

The smallest thickness of the ML graphene samples used in this work was ~3 nm, which corresponds to ~9 layers of graphene sheets. Thus, all the ML graphene samples are expected to have no response to perpendicular external electric field, which means that electrical conductivity should be constant regardless of the gate voltage (V_g) modulation [54]. Also, since the work functions (WFs) of all three contact materials are similar in range (graphene: 4.6 eV, amorphous

carbon: 4.5 eV, and Cr/Au: 4.3 eV), all the devices should exhibit close to Ohmic behavior [14,36,55]. This was confirmed by three-terminal (d: drain, s: source, g: gate) electrical measurements (I_{ds}-V_{ds} & I_{ds}-V_g) for all the device structures, and accordingly, we evaluated the device resistance from I_{ds}-V_{ds} using the linear fitting based on Ohm's law. All electrical measurements were conducted by a two-terminal method at a fixed gate voltage of V_g=0 V.

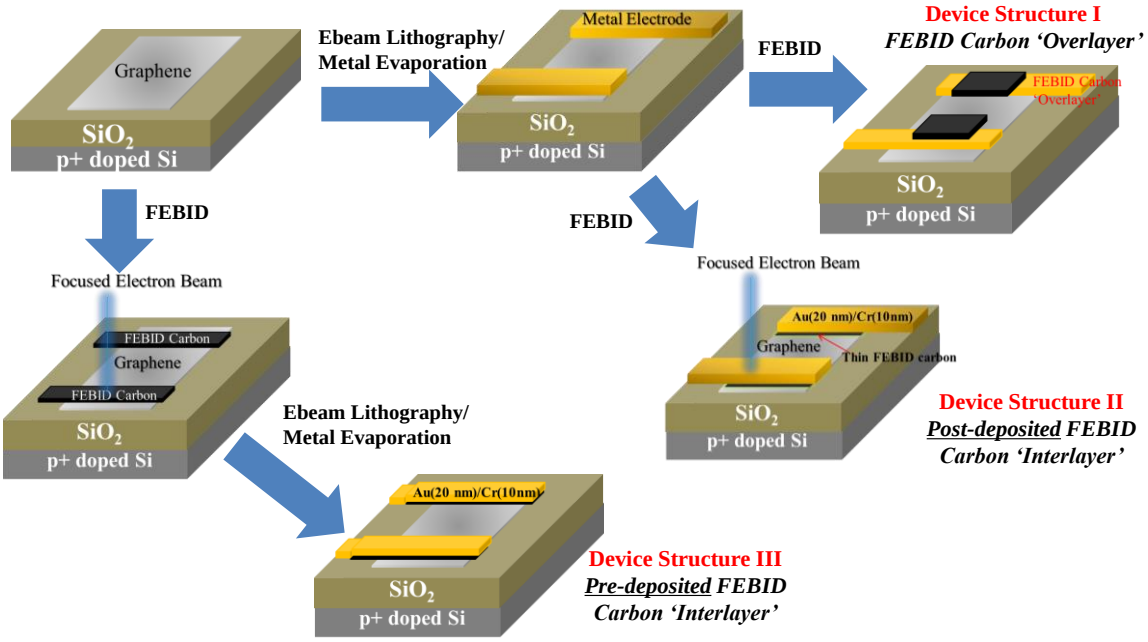

Figure 3.2. Schematic of the three strategies for fabrication of graphene-metal interconnects *via* FEBID graphitic nanojoints.

3.3 Device structure I: FEBID carbon 'overlayer' nanojoint

3.3.1 Device fabrication

Device structure I adds an additional conductive path through the FEBID carbon 'overlayer' nanojoints between the ML graphene and metal electrodes. An interconnect between the 38 nm thick ML graphene and metal electrodes, as shown in Figure 3.3(a), was fabricated using e-beam lithography followed by Au (20 nm)/Ti (10nm) deposition using e-beam evaporator and lift-off

procedure. The ML graphene was characterized using a confocal Raman spectroscopy with minimum laser power (~ 1 mW). In the Raman spectrum of graphene or graphite, the G peak is related to in-plane bond-stretching of sp^2 carbon pairs [53]. The D peak is due to a breathing mode of sp^2 carbon atoms in sixfold rings, and it requires defects for its activation. Thus, the D peak is related to increase of the disorder in sp^2 sites, and thus a low D/G intensity ratio, I(D)/I(G), indicates a high quality of graphene. Accordingly, we can conclude that the ML graphene has high quality with I(D)/I(G)~0 as shown in Figure 3.3(b). Figure 3.3(c) shows the device structure with FEBID carbon 'overlayer' nanojoints covering one third of one graphene-metal contact width. The sectional AFM profile of the device in Figure 3.2(d) shows the thickness profile of metal electrodes and FEBID carbon 'overlayer' nanojoints to graphene, indicating that the FEBID carbon 'overlayers' fully (*i.e.*, with no connectivity breaks) link graphene and metal electrodes forming an electric interconnect.

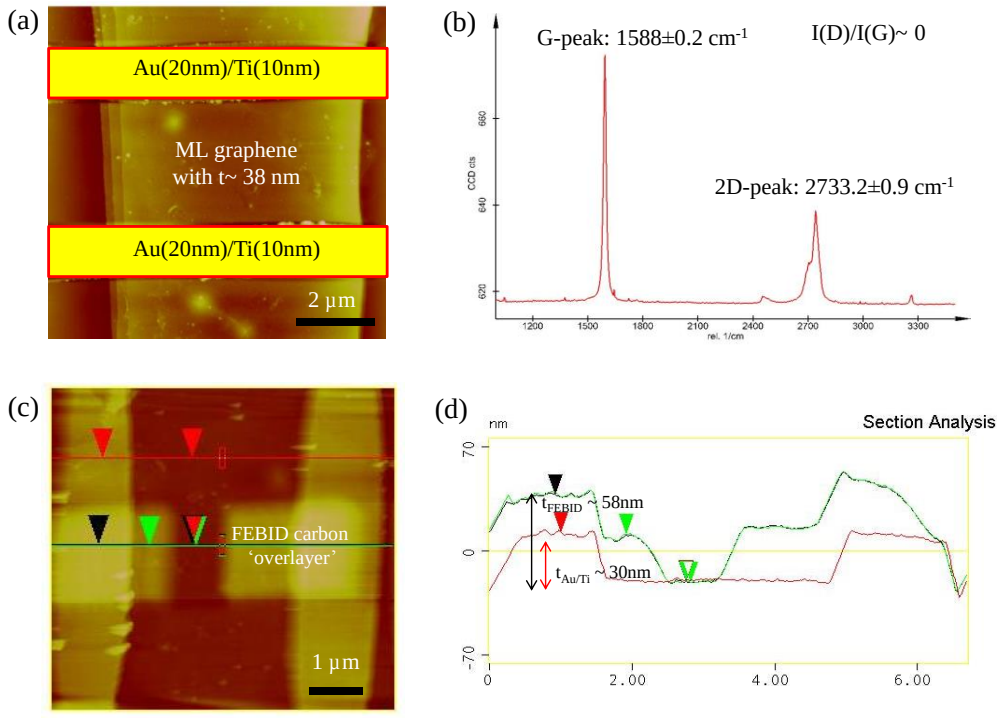

Figure 3.3. (a) AFM image of the as-fabricated ML graphene-metal device, (b) Raman spectrum of ML graphene showing its high quality, (c) AFM image of a device with FEBID carbon

'overlayers' formed at both electrodes and (d) AFM sectional profile showing connection of the ML graphene and metal electrodes *via* FEBID carbon 'overlayers'.

3.3.2 Reduction of the device resistance with an additional conductive path through FEBID graphitic nanojoints

To demonstrate the effect of FEBID carbon 'overlayer' nanojoints on electrical performance of the ML graphene device, two-terminal (drain-to-source) electrical measurements are adequate since gate voltage has no effect on electrical conductivity of the device in the case of multilayer graphene. The I_{ds}-V_{ds} data in Figure 3.4(a) show linear behavior indicating Ohmic contact at the ML graphene-FEBID carbon-Au junctions. Figure 3.4(b) shows the reduction of the device resistance with FEBID 'overlayer' nanojoints and the inset shows the electrical measurement setup. Initial reduction of the device resistance by 14% resulted from forming an additional conductive path for electrons through the FEBID of hydrogenated amorphous carbon (H:aC). Further reduction was achieved by post-deposition thermal annealing of FEBID nanojoints in vacuum (P~10^{-5} Torr) resulting in graphitization and improvement of carbon electrical conductivity. The 1st annealing step was done at 100 $^{\circ}$C (with the temperature ramp rate: 5 $^{\circ}$C/min) during which the dehydrogenation occurs in the as-deposited FEBID H:aC nanojoints [46], which led to reduction of the device resistance by only 4%. After annealing at 310 $^{\circ}$C, an additional decrease of the device resistance by 7% was observed. Overall, this multi-step procedure resulted in 30% reduction of the device resistance with addition of FEBID graphitic conductive path, compared to the as-fabricated standard metal contact.

Figure 3.5 shows the Raman spectra of the FEBID nanojoints, showing transformation of their composition from the amorphous ('as-deposited') to the graphitic ('annealed' at 310 $^{\circ}$C for 15 min with the temperature ramping rate~ 5 $^{\circ}$C/min) structures. As mentioned in Chapter 2, the G peak position and D/G area ratio, A(D)/A(G), are quantitative indicators of the degree of graphitization. For nanocrystalline graphite, it is known that the G peak position is around 1600 cm^{-1} and A(D)/A(G) is about 2.5 [46,53]. For the FEBID deposits, the G peak position and

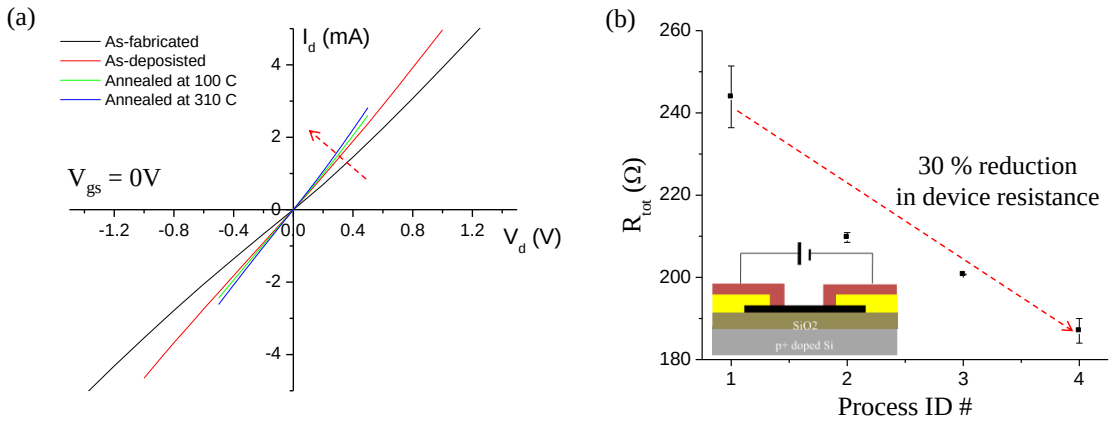

Figure 3.4. (a) Electrical measurements for the ML graphene device with FEBID carbon 'overlayer' using the two-terminal method, and (b) the reduction of the device electrical resistance achieved with FEBID graphitic 'overlayer' nanojoints. (Process ID Process #1: As-fabricated only with metal contacts, #2: As-deposited FEBID contacts, #3: 1st annealing at 100 ˚C in vacuum and #4: 2nd annealing at 310 ˚C in vacuum)

A(D)/A(G) for the annealed nanojoints were measured as 1587.9 cm^{-1} and 1.88, respectively, indicating the partially graphitic structure with an increase of sp^2 carbon network domains. Since the deposits were not fully graphitized, one would expect that additional annealing at an elevated temperature or increasing the annealing time should further improve the contact resistance. Also, it is worth noting that further reduction of the contact resistance can be achieved by increasing contact width of FEBID nanojonits at ML graphene-metal interface. Unfortunately, since the device was broken due to rapidly ramping up the temperature to 530 ˚C (~8.3 ˚C/min) for further graphitization, we could not perform any additional electrical measurements to demonstrate the impact of continuous annealing. It is recommended that care should be exercised in selecting the annealing rate to avoid an excessively rapid increase in temperature, and instead slower annealing for a prolonged time should be used in order to achieve the desired benefit of carbon graphitization while avoing catastrophic damage of a device due to thermomechanical stresses.

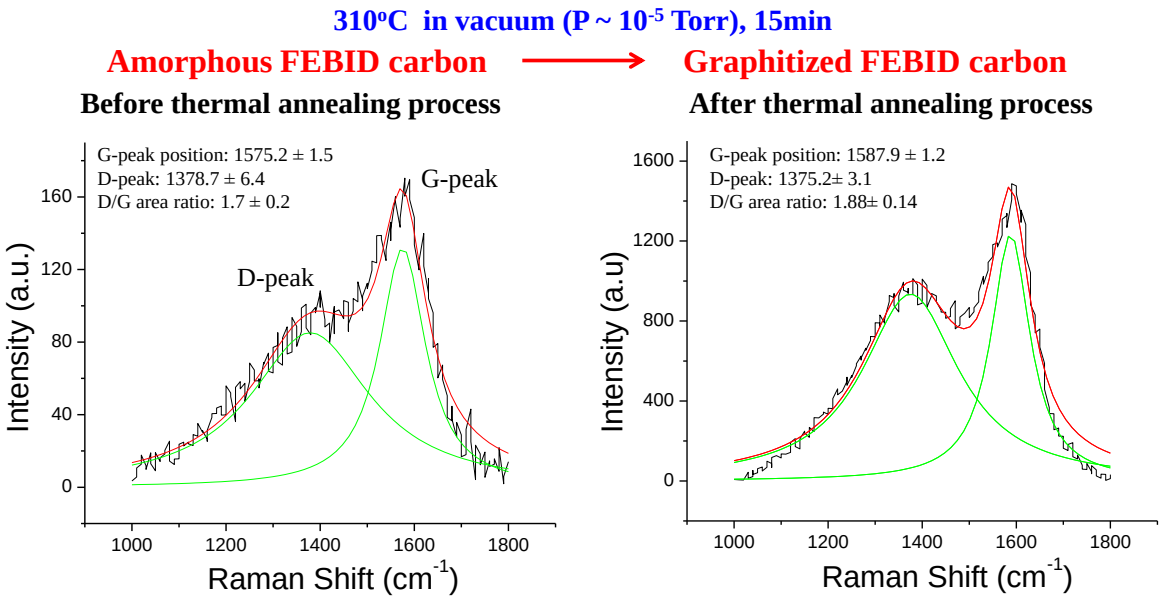

Figure 3.5. Raman spectra before and after thermal annealing at 310 ◦C in vacuum (P~10^{-5} Torr) indicating the transformation of the FEBID carbon contacts from the amorphous to the graphitic structure.

3.4 Device structures II and III: FEBID carbon 'interlayer' nanojoints

3.4.1 Device fabrication

As mentioned earlier, the electrical properties of the graphene-metal contact are determined by the nature of electronic interactions, which are defined by molecular binding at the interface (*i.e*. physical/van der Waals vs. chemical/covalent bonding). Our DFT calculations shown in Figure 3.1 indicate that the carbon atom as an interfacial link has strong chemical binding on the basal plane of graphene, and its binding energy is stronger than that of Ti contacts to graphene, which is the best metallic material with contact resistivity of 2e-4 Ω-m [18,21]. Also, in our previous work, we experimentally showed that the FEBID graphitic nanojoints at open-ended MWCNT-metal interface resulted in contact resistivity of at least ~5e-6 Ω-m, assuming the channel resistance of MWCNT is negligibly small. This suggests that FEBID graphitic nanojoints should also improve intrinsic interfacial properties at the graphene-metal contact. Guided by this

insight, device structures II and III are proposed to improve the intrinsic interfacial property of graphene-metal contact using thin FEBID carbon 'interlayers'.

The fabrication protocols for two device structures are shown in Figure 3.5. Figure 3.5(a) shows the fabrication protocol of a ML graphene-metal interconnect with a 'post-deposited' FEBID interlayer (Device structure II). An AFM image in Figure 3.6(a) shows formation of the FEBID carbon interface to ML graphene with thickness of ~7 nm, corresponding to ~21 layers of graphene. At the targeted graphene regions (red box), metal electrodes were fabricated using e-beam lithography followed by Au(20 nm)/Cr(10 nm) deposition and lift-off procedure. After fabrication of metal electrodes, focused electron beam with spot size 3 (~ 30 pA) and beam energy of 25 keV was exposed on top of ML graphene-metal contact areas to fabricate atomically thin FEBID carbon interlayer using entrapped hydrocarbon contaminants as precursor molecules.

Device structure III described in Figure 3.6(b) was fabricated by firstly depositing a thin FEBID carbon interlayer (thickness~1.4 nm) on ML graphene (thickness~3 nm) followed by Au (20 nm)/Cr (10 nm) deposition on top of FEBID carbon interlayer. While a complete, uniform surface coverage with FEBID carbon interlayer can be guaranteed in this device structure, interfacial coupling between the FEBID carbon interlayer and a metal electrode would be worse than that for a 'post-deposited' FEBID interlayer in the device structure II since metal deposition on 'pre-deposited' FEBID interlayer would result in a weak (physical interaction) binding similar to the standard metal contact to graphene. In order to enhance the interfacial property between FEBID carbon interlayer and metal, we additionally scanned the top of metal-FEBID interlayer-ML graphene contact areas by the focused electron beam, attempting to improve interfacial binding similar to the device structure II with the 'post-deposited' interlayer.

For each ML graphene sample, reference standard metal contacts were also fabricated for side-by-side comparison of electrical performance. For all devices, thermal annealing in vacuum

was performed to graphitize the FEBID carbon interlayers and to improve their electrical conductivity.

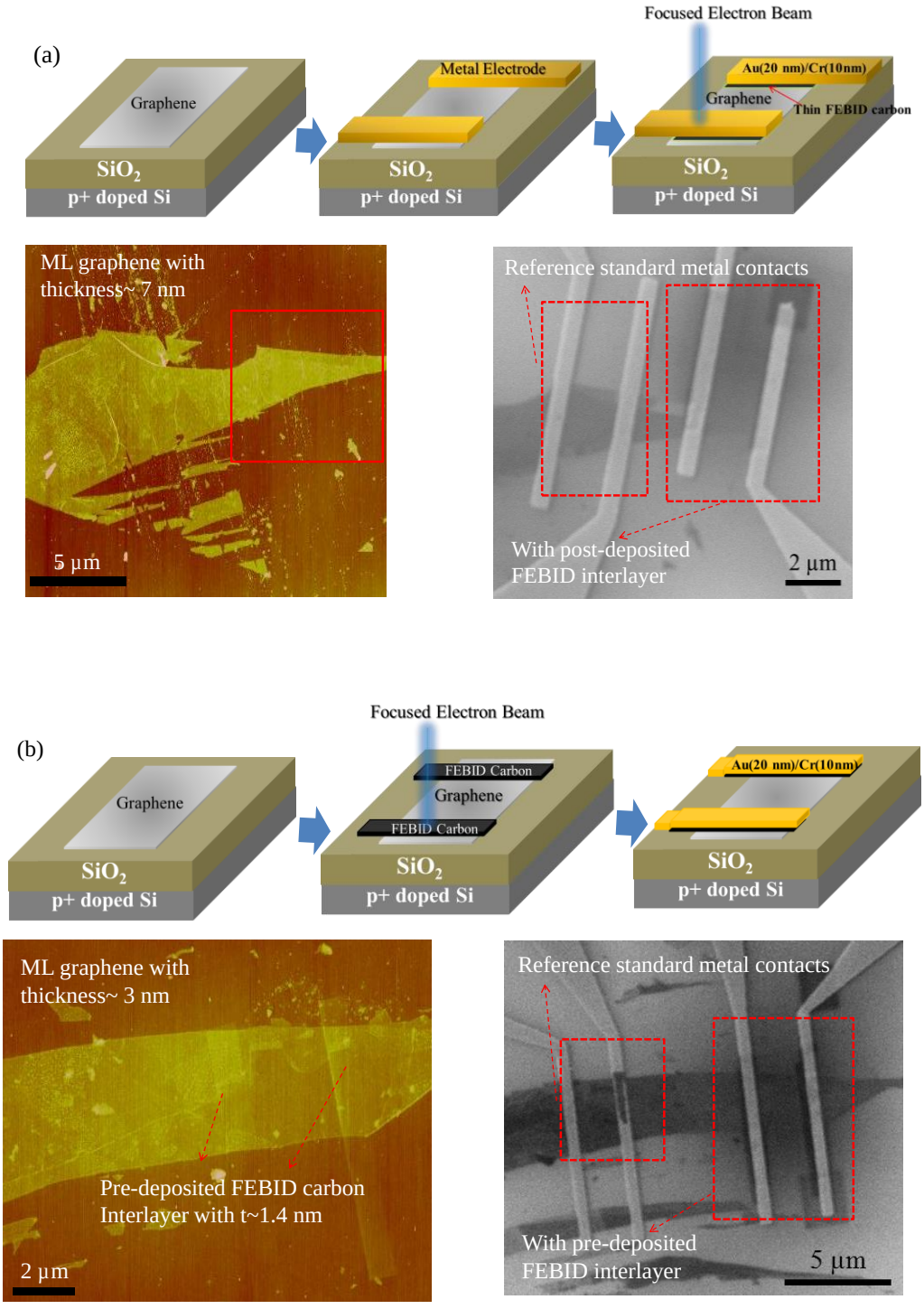

Figure 3.6. Schematics and the corresponding AFM and SEM images for mechanically exfoliated ML graphene devices with (a) post-deposited and (b) pre-deposited FEBID carbon 'interlayer' to improve intrinsic interfacial properties at the ML graphene-metal contacts.

3.4.2 Improved interfacial coupling at the ML graphene-metal contact *via* FEBID carbon interlayer

Figure 3.7 shows the I_{ds}-V_{ds} measurements for all devices at zero back-gate voltage. Figures 3.7(a) and 3.7(b) are for the devices with post-deposited and pre-deposited FEBID carbon interlayer, respectively, while Figures 3.7(c) and 3.7(d) are for the devices with a standard metal contact only for comparison. Focused electron beam scanning over the metal contact area, hereafter defined as 'post-deposition' of FEBID interlayer, improved the electrical conductivity of a device with the pre-deposited FEBID interlayer (Figure 3.7(b)), while it does not appear to make any significant contribution to the device with the post-deposited FEBID interlayer (Figure 3.7(a)). It is clear that 'post-deposition' of a FEBID carbon interlayer improves the interfacial property, but differences in contribution of the FEBID carbon interlayer in the two device structures are due to the parasitic deposition of a thin carbon film on the graphene channel, which introduces scattering sites for electron transport. For the device with a pre-deposited interlayer, the graphene channel is already contaminated by a thin film of FEBID carbon during the pre-deposition and thus further contamination does not influence the electron transport through the graphene channel. However, for the device with a post-deposited interlayer, an unintended thin carbon film on 'clean' graphene channel increases the channel resistance of the as-fabricated device, along with improving the intrinsic interfacial binding and electronic coupling at the graphene-metal contact. Thus, one can expect that there should be a 'trade-off' between an increase of the channel resistance due to the parasitic deposition of carbon vs. the reduction of the contact resistance owing to the improved electronic coupling at the contact interface. Interestingly, despite a negative effect of FEBID carbon on the channel resistance, one finds that the devices with the FEBID interlayers exhibit an improved electrical conductuvity upon thermal annealing in vacuum. On the other hand, annealing of standard metal contacts does degrade performance (Figures 3.7(c) and 3.7(d)), possibly due to interfacial breakdown.

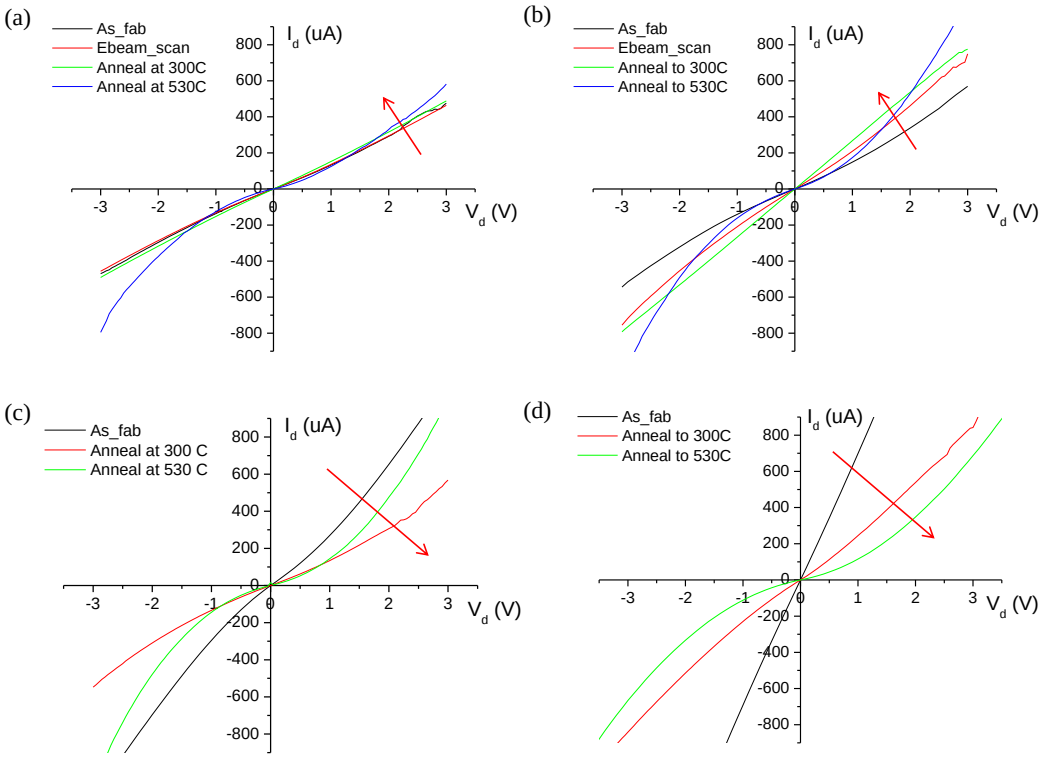

Figure 3.7. Electrical measurements for devices with (a) post-deposited FEBID carbon 'interlayer', (b) pre-deposited FEBID carbon 'interlayer', (c) and (d) standard metal contacts only. All measurements were performed at V_g=0V using two-terminal method, and thermal annealing was performed in vacuum, P~10^{-5} Torr.

In order to clearly identify the contribution of the graphitic interlayer, the linearity of I_{ds}-V_{ds} curves and device resistance normalized by the contact width (yielding the device resistivity) are examined in Figures 3.8(a) and 3.8(b), respectively. Figure 3.8(a) shows the linearity obtained from the linear fitting of I_{ds}-V_{ds} measurements using Ohm's law. Focused electron beam scanning (process ID #2) and thermal annealing at low temperature (310 ˚C) in vacuum (process ID #3) improved the I-V linearity (Ohmic behavior) almost to an ideal limit with a FEBID interlayer, while thermal annealing of devices with standard metal contacts (Figure 3.8(a)), even at low temperature, degraded the linearity of I-V curves. The same trend can be observed in the device resistivity in Figure 3.8(b). This result implies that a FEBID interlayer improves both the electrical and thermo-mechanical properties at the graphene and metal interfaces. However, at high temperature annealing (530 ˚C), the linearity for all devices decreased showing the rectifying

behavior, and the device resistance continues to increase after repeating the bias voltage sweep from -4 V to 4V as shown in Figure 3.8(c), which indicates that the interfaces are degraded when excessive temperature is applied for interface conditioning. Device resistivity after high temperature annealing (process ID #4) in Figure 3.8(b) was obtained from the initial measurement of I_{ds}-V_{ds} before degradation due to repeated electrical biasing. While repeating the bias voltage sweep increases the electrical resistivity of all devices, high temperature annealing (process ID #4) reduces the device resistivity with a FEBID interlayer, as shown in Figure 3.8(b). It is likely owing to graphitization (and improved electrical conductivity) of the interlayer despite the interfacial breakdown. Yet, after repeated measurements, the interfacial breakdown appears to overwhelm the improvement of the interface electrical conductivity due to the FEBID graphitic interlayer, which poses a significant challenge to practical applications of the proposed interface improvement method. These observations motivate additional efforts to understand the mechanism of annealing of a FEBID carbon interlayer and to develop an improved methodology for graphitizing the FEBID carbon "interlayer" interface at low temperature.

3.5 Concluding remarks

In summary, three fabrication protocols for FEBID graphitic nanojoints were developed in order to reduce contact resistance at the mechanically exfoliated multilayer graphene-metal junctions, along with in-depth characterizations of the fabrication protocols for the materials' topological/compositional properties and device performance tests. FEBID carbon 'overlayer' nanojoints are designed to provide additional conductive paths connecting the graphene channel and metal electrodes. FEBID graphitic 'interlayer' nanojoints are intended to improve the intrinsic interfacial property of graphene-metal contacts. Pre-deposited or post-deposited interlayer fabrication schemes depend on whether the FEBID carbon interlayer formation is done before or after metal contact fabrication on graphene. All the fabrication protocols were found to

improve electrical and thermo-mechanical interfacial properties of the graphene-metal junctions after a low-temperature (310 ˚C) thermal annealing in vacuum, while the graphene devices without FEBID graphitic nanojoints degrade upon thermal treatment. However, after a high-temperature (530 ˚C) annealing in vacuum, all the devices, even with FEBID graphitic nanojoints, begin to degrade, which suggests a low-temperature annealing with prolonged duration in order to achieve complete graphitization of the FEBID carbon interlayer.

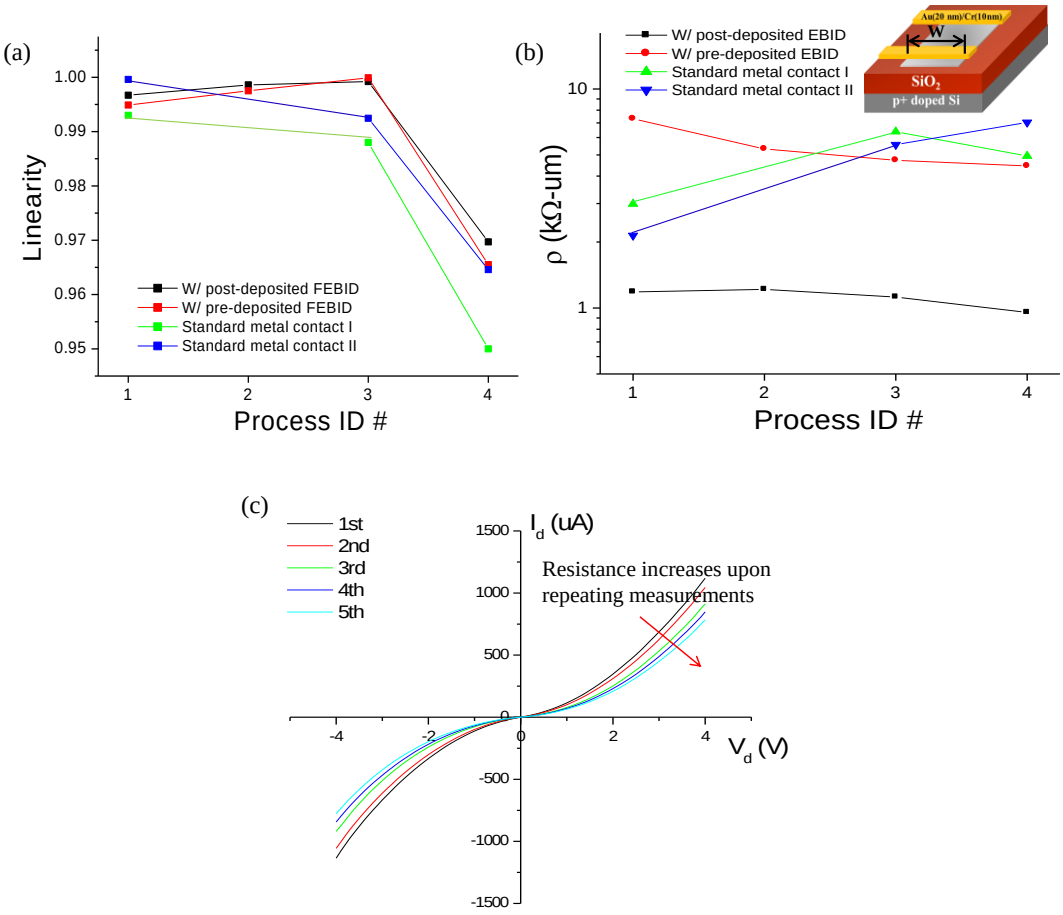

Figure 3.8. (a) Linearity of I_{ds}-V_{ds} curves after each step (process ID) of the experimental process, and (b) device resistivity for all investigated devices. (c) Repeated measurements after high temperature annealing at 530 ˚C by sweeping the bias from -4 V to 4 V, resulting in an increase of the device resistance which indicates the interfacial breakdown. Process ID #1: as-fabricated, #2: focused electron beam scanning over graphene-metal contact area, #3: annealed at 300 ˚C, and #4: annealed at 530 ˚C.

CHAPTER 4

UNDERSTANDING THE INTERACTIONS OF FEBID CARBON WITH CVD GROWN MONOLAYER GRAPHENE

4.1. Overview

While mechanically exfoliated graphene is superior in its structural quality and electronic properties, it has significant challenges such as lack of controls in the number of graphene layers and poor scalability, which limits its applications in industrial settings. On the other hand, a chemical vapor deposition (CVD) method enables a wafer-scale growth of graphene and thus, provides a pathway towards scalability, with the assistance of lithography techniques. It makes it possible control the number of layers, and a CVD graphene has the quality adequate for many device applications [56-58].

In the previous chapter, the fabrication protocol for a FEBID graphitic interlayer between mechanically exfoliated multilayer graphene and metal electrodes was developed in order to improve electro-mechanical properties of the graphene-metal junctions. FEBID processing generally entails unintentional carbon deposition around intended deposition areas due to long-traveling, primary electrons which lose their energy to the level suitable to deposition reaction upon multiple collisions [38]. When applying the developed fabrication protocol to CVD monolayer graphene electronic devices, unintentional carbon deposition can affect device characteristics since a single atomic layer of graphene is very sensitive and can be damaged or easily doped by either foreign species or by external forces. Therefore, prior to applying the protocol for engineering interface properties of graphene-metal junctions, it is required to have in-depth understanding of interactions between FEBID carbon and graphene to achieve control of FEBID conditions for reduction of electrical contact resistance of graphene-metal junctions.

In this chapter, we describe a procedure developed for transferring a CVD monolayer graphene film from Cu foil (growth substrate) to a dielectric substrate (test device) in order to minimize defects, wrinkles and cracks of the graphene film. Using high quality graphene samples obtained using an optimized transfer protocol, we investigate the nature of physico-chemical interactions of two possible FEBID carbon deposit states-'intended' FEBID graphitic interlayer at the area exposed to high energy electrons vs. 'unintentional' parasitic carbon contamination in the areas exposed to low energy secondary electrons only. First-principles calculations using density functional theory (DFT) provide molecular scale understanding of the nature of FEBID carbon adsorption states on graphene, dependent on the energy of electrons contributing to deposition, with experimental confirmation by Raman analysis of graphene with FEBID carbon patterns. This fundamental understanding led to the development of a post-deposition Raman laser ablation technique to remove physisorbed parasitic FEBID carbon contamination from active areas of graphene electronic devices, which is essential for advancing the FEBID utility in engineering the interfacial properties of the graphene-metal contacts. Furthermore, this work contributes to enhancing the FEBID capabilities for high resolution carbon patterning of graphene for chemical functionalization for developing next-generation graphene-based electronic and chemical sensing devices.

4.2. Introduction

CVD graphene is generally grown on a Cu foil, which provides nucleation sites for forming graphene's hexagonal structure. Therefore, as-grown graphene should be first released from copper and transferred to a dielectric substrate in order to fabricate graphene electronic devices. One of graphene transfer methods is PMMA (Poly(methyl methacrylate))-mediated wet transfer method [57,58] with an etching solution to dissolve Cu foils. While this method is very simple and widely utilized, it can result in degradation of graphene film quality *via* the formation of wrinkles and cracks due to multiple steps of the transfer process. Thus, optimization of the

transfer process for minimizing the wrinkles and cracks is essential to achieve high quality graphene film and thus better performance of electronic devices.

On a graphene surface, which forms two-dimensional hexagonal lattice structure of sp^2 bonded carbon atoms, high energy electron irradiation can affect adsorption of precursor molecules and fragments of precursor dissociation reaction since it can modify local structure of graphene. A range of point-like defects can be controllably generated, ranging from vacancies or Stone-Wales (SW) defects to sp^3-type defects, depending on the beam energy and dose [28,59]. These structural modifications of the highly inert graphene surface can reduce activation barriers for chemisorption of reactive radicals dissociated by electron beam at the room temperature [28,60]. Unlike for a bulk substrate, chemisorption of reactive species on graphene has a significant impact in that it can tune the graphene's electronic properties, including opening a band gap and enhancing spin-orbit coupling [61-63].

Among a variety of possible "active" species suitable for functionalization, recent theoretical studies revealed that controlled chemisorption of carbon atoms or hydrocarbon radicals are particularly effective in modifying the electronic and magnetic properties of graphene [64-68]. Depending on adsorption state configuration and surface coverage, electromagnetic properties of graphene can be modulated, which illustrates the importance of controlled deposition of carbon atoms to enable applications of graphene for electronic and spintronic devices. Thus, nanoscale "direct-write" deposition by focused electron beam (FEBID) using hydrocarbon precursors provides an intriguing opportunity for controlled covalent functionalization of graphene by individual carbon atoms, resulting in localized, high resolution patterning of a graphene substrate. In turn, this makes it possible to achieve an electron beam-confined modification of electromagnetic properties of graphene based materials, since FEBID-produced carbon deposits can be easily transformed from insulating amorphous to conducting graphitic structures with an assist of annealing techniques [32,46,69,70].

Intrinsic resolution of FEBID carbon patterning on graphene is comparable to a diameter of the focused primary electron beam down to a few nanometers, which stresses its superiority in control of the patterning resolution [71,72]. However, such a high resolution is only feasible on suspended graphene. When graphene is supported by a bulk substrate such as SiO_2/Si, as relevant to its application in electronic devices, unintentional hydrocarbon deposition and broadening of target patterns are inevitable due to a wide-range spatial distribution of secondary electrons [24-27,71,72]. This degrades the resolution of patterning, impeding a desirable level of spatial control of graphene functionalization and, as mentioned earlier, it contaminates the graphene conduction channel giving rise to the increase of electrical resistance of graphene devices. Thus, for successful application of the FEBID technique to real device platforms, it is important to eliminate unintentional (parasitic) carbon deposits without introducing any structural defects or damage to graphene, which require the first-principles understanding of carbon-graphene interactions under different FEBID conditions.

4.3 Optimization of a graphene transfer method

The two factors determining graphene film quality upon transfer onto a SiO_2/Si substrate are wrinkles and cracks. While the cracks result from transfer procedures, the wrinkles can also originate from the roughness of graphene-supporting Cu foil during graphene growth. A high temperature (~1000 ◦C) condition for graphene growth results in long, straight line deformations of Cu foil as shown in Figure 4.1(a). It ends up generating similarly shaped wrinkles on transferred graphene, as shown in Figure 4.1(b). It is unavoidable unless the low temperature condition is used for graphene growth. In this chapter, we only focus on the optimization of the graphene transfer procedure, as the CVD graphene samples were provided by collaborators from the Air Force Research Laboratory (AFRL). As shown in Figures 4.1(c), the transfer procedure results in cracks and wrinkles with random directions having microscale lengths with nanoscale

heights. Unlike the long, straight line wrinkles coming from the Cu foil, those defects can be minimized *via* optimizing the transfer procedures.

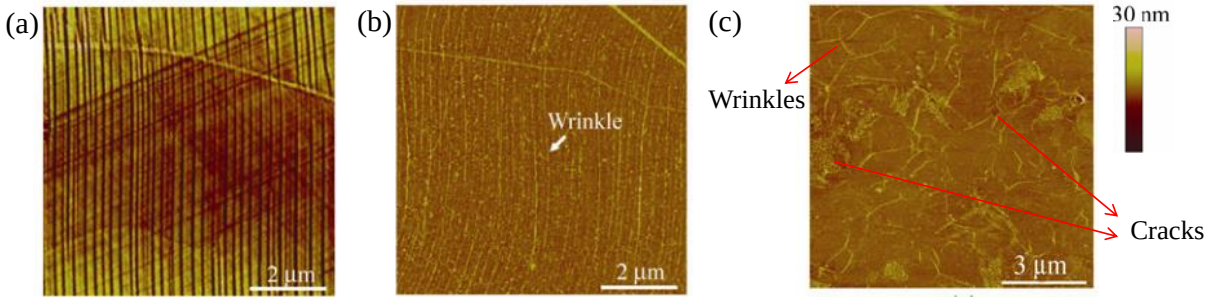

Figure 4.1. (a) AFM image of Cu foil after CVD graphene growth at 1000 ˚C, showing long, straight line deformations resulting in (b) the corresponding wrinkles on graphene transferred onto a 300 nm SiO_2/Si substrate. (c) AFM image of randomly-distributed, microscale wrinkles and cracks generated due to the multiple steps of the transfer procedures. Reprinted from ref. [73].

The general PMMA-mediated wet transfer method is described in Figure 4.2. 4 w/w% PMMA solution in toluene is spin-coated on a graphene/Cu foil sample with 3000 rpm for ~ 1 min, which results in ~200 nm thickness of the coated PMMA layer. A PMMA/graphene/Cu foil sample is post-baked on a hot plate at 180 ˚C for ~ 1min, in order to evaporate the solvent and harden the PMMA layer. PMMA coating on graphene/Cu enables graphene to be visible after Cu etching and also lowers the possibility that graphene film is torn during the transfer procedures. Then, the sample is placed into 0.05 g/ml ammonium persulfate/DI water solution, which is an etchant of Cu. The Cu foil completely dissolves into the solution after ~3 hrs, and only the PMMA/graphene remains floating on the solution surface. By scooping it out of the solution with a SiO_2/Si substrate, the PMMA/graphene film is transferred onto the substrate. In order to remove water and establish better contact between the PMMA/graphene and the substrate before removing the PMMA layer, the sample is heated to 180 ˚C on a hot plate. Finally, the PMMA layer is removed using acetone heated to 80 ˚C, and the graphene film is washed several times using DI water to remove the residual solvent and solutes. This method is widely accepted for

graphene transfer, but significant density of cracks can occur during removal of the PMMA layer [58]. To overcome this problem, an improved transfer method (called 'improved PMMA-mediated wet transfer method') was developed adding an additional PMMA coating step to the transferred PMMA/graphene sample before removing the 1st PMMA layer [58]. The additional PMMA liquid was found to redissolute the 1st PMMA layer on graphene and mechanically relaxes the underlying graphene film, leading to a better contact with the SiO_2/Si substrate upon transfer and which, in turns, reduces the number and size of cracks [58].

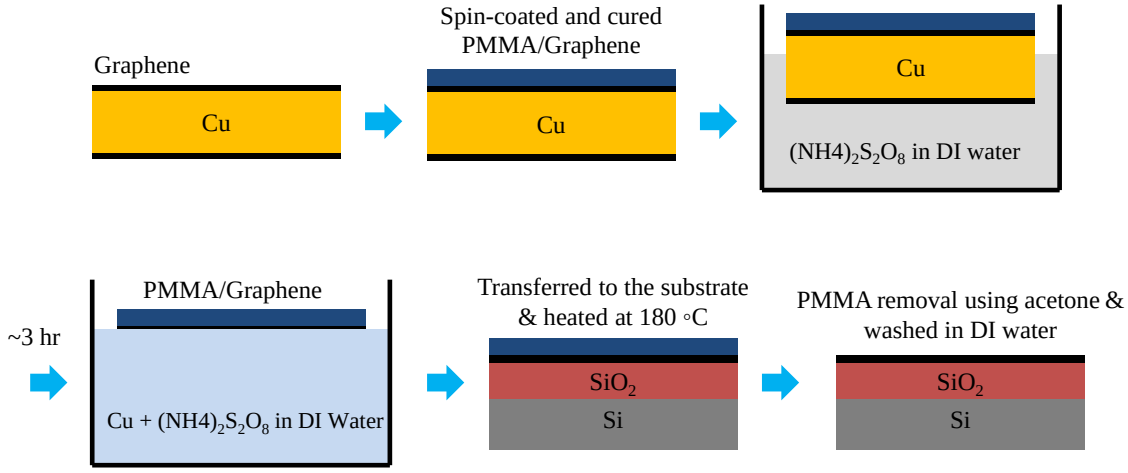

Figure 4.2. Schematic of the PMMA-mediated wet transfer method.

We first utilized the 'improved PMMA-mediated wet transfer method' to reduce the number of cracks. Figure 4.3(a) shows SEM images of graphene transferred onto the SiO_2/Si substrate. While some cracks are found on the graphene film, most area of the film is very continuous, and thus, can be utilized for electronic device fabrication. However, as shown in the AFM images (Figures 4.3(b) and (c)), the film quality and thickness are not uniform throughout, with a high density of micro-scale wrinkles, which may degrade the performance of graphene devices.

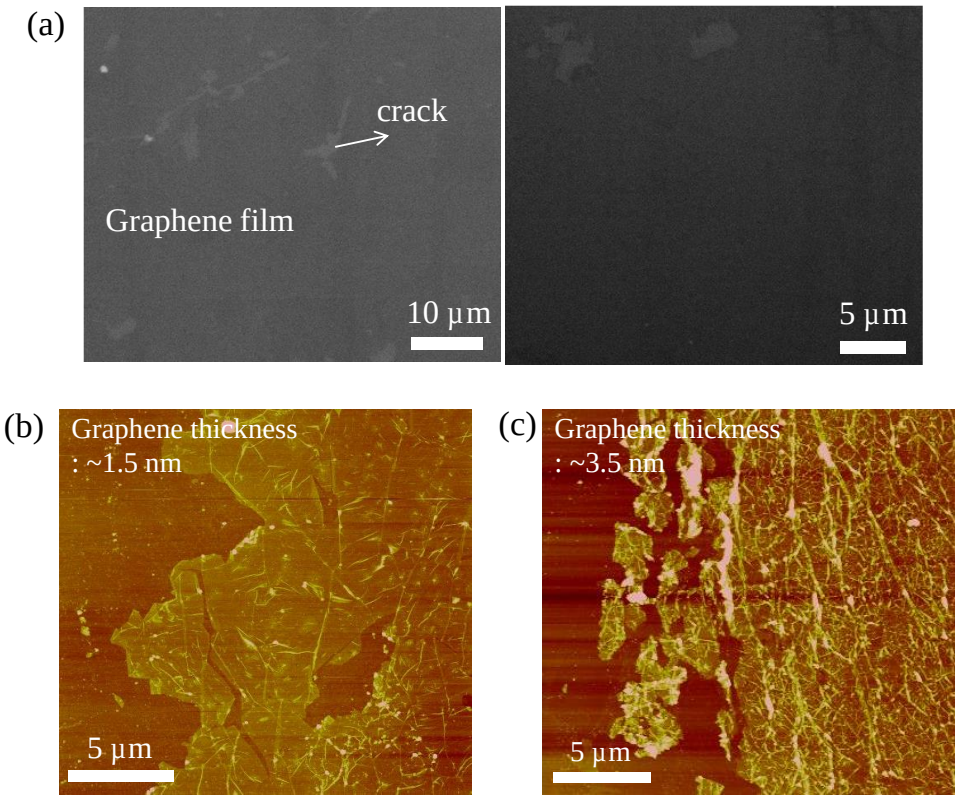

Figure 4.3. (a) SEM images of the graphene film transferred onto a 300 nm SiO_2/Si substrate, and AFM images of graphene in the areas with (b) the lowest and (c) the highest densities of wrinkles. The z-scale of AFM images is 50 nm.

In order to achieve the better graphene quality, one additional step was added to the transfer procedure, along with investigating the effect of the water evaporation rate on the final outcome of the quality of graphene film, as shown in Figure 4.4. Graphene also grows on the back side of Cu foil, which is possibly detrimental to the quality of the film when it is transferred from copper to a device substrate. Thus, before dissolving the Cu foil, graphene present on the back side of Cu foil was etched away by exposing to O_2 plasma at the pressure of 50 mTorr for 40 s. Then, the Cu foil was cut into three pieces in order to study the effect of the water evaporation rate (controlled by changing the temperature of the PMMA/graphene transferred onto the SiO_2/Si substrate) on the transferred graphene film quality. Three different temperature conditions were considered when evaporating water after transferring PMMA/graphene onto the SiO_2/Si substrate. The

PMMA/graphene samples were heated to (1) 180 ˚C for rapid evaporation, (2) 50 ˚C for intermediate evaporation, and (3) being tilted at a room temperature so that water can flow out slowly from the space between the PMMA/graphene and the substrate. After plasma etching of graphene on the back side of Cu foil, all three films have uniform distribution of the wrinkles (height < 10 nm) and the thickness with 1.5 nm ~ 2.0 nm. Even at the intermediate evaporation rate, significant wrinkles can be seen on the graphene film (Figure 4.5(b)), comparable to those at the rapid evaporation rate (Figure 4.5(a)). However, when water is removed from a tilted sample at room temperature, the graphene film has been found to have much lower density of wrinkles (Figure 4.5(c)).

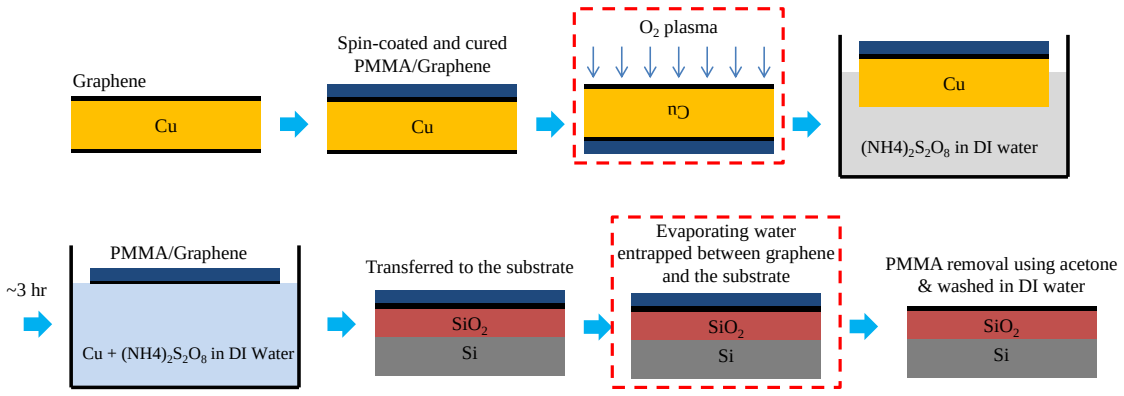

Figure 4.4. Schematic of the PMMA-mediated wet transfer method with additional steps of removing any graphene or carbon structures on the back side of Cu foil and carefully controlled slow evaporation of water entrapped between graphene and the substrate.

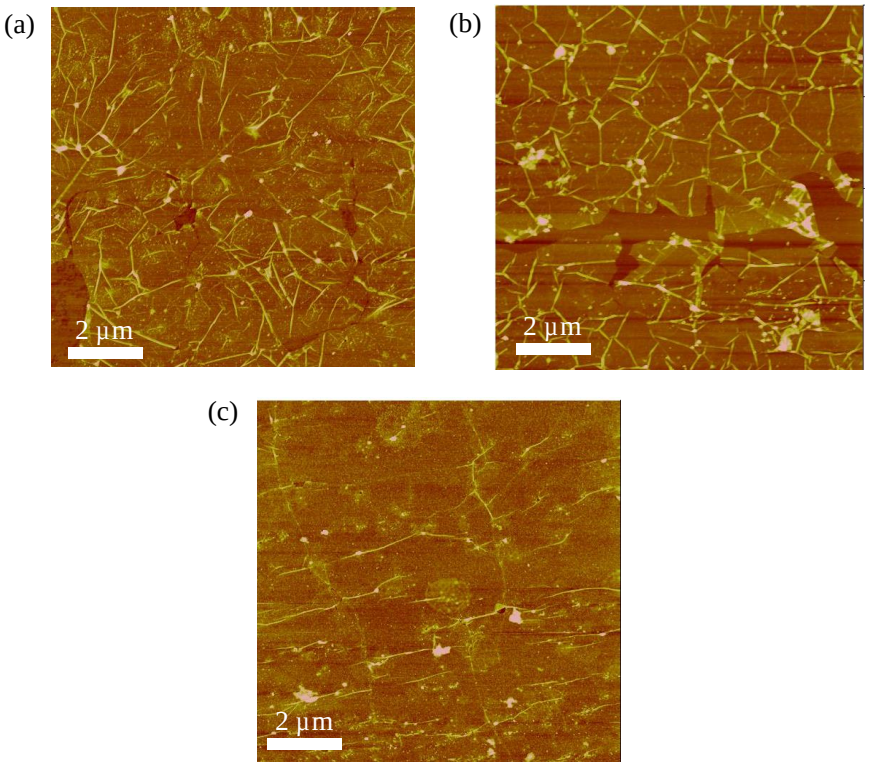

Figure 4.5. AFM images showing the distribution of wrinkles on the graphene films transferred onto the 300 nm SiO_2/Si substrates with (a) rapid evaporation (at 180 ◦C), (b) intermediate rate evaporation (at 50 ◦C) and (c) slow evaporation (tilted at a room temperature) of water entrapped between PMMA/graphene and the SiO_2/Si substrates. The z-scale of the images is 20 nm.

Optical microscope images shown in Figure 4.6 also suggest the superiority of the tilted drying method in that it can significantly reduce the number of cracks. Figures 4.6(a) shows the graphene film transferred with an intermediate water evaporation rate (heated to 50 ˚C). A lot of cracks are found on the graphene film which is detrimental to have consistent, highly reliable performance of graphene-metal devices and interconnects, especially critical for contact resistance measurements using transmission line method (TLM). On the contrary, the graphene film transferred with the tilted drying method at a room temperature in Figure 4.6(b) has a much lower density of cracks, which enables us to fabricate reliable TLM device structures for contact resistance measurements.

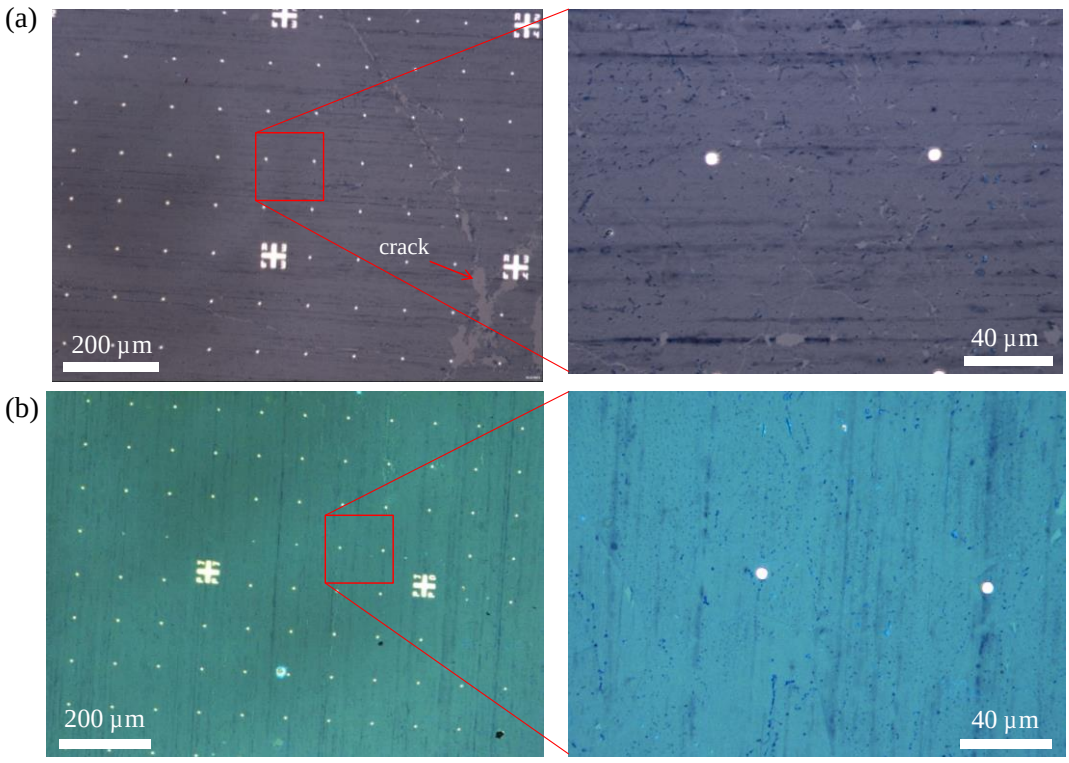

Figure 4.6. Optical microscope images of graphene films transferred with (a) intermediate evaporation rate (at 50 ˚C) and (b) slow evaporation rate (tilted at a room temperature) of water entrapped between PMMA/graphene and the SiO_2/Si substrates, which shows the density of cracks generated during the transfer procedure.

The graphene film in Figure 4.6(b) was characterized for its structural quality (presence of defects on the graphene's hexagonal crystalline structure) using a confocal Raman spectroscopy, as shown in Figure 4.7. As explained previously, the structural quality can be evaluated with the intensity ratio of D to G peaks, I(D)/I(G), in the Raman spectrum. Smaller I(D)/I(G) represents fewer defects and a higher quality of graphene. I(D)/I(G) of the graphene film was found as ~0.18, which corresponds to the distance between two defects, L_D~ 26 nm and the number density of the defects ~ 464 /µm^2 [74]. The intensity ratio of 2D to G peaks indicates the number of graphene layers, along with a 2D peak shape [75]. In the Raman spectrum, I(2D)/I(G) was found as ~2.5 and a 2D peak has a sharp single peak, indicative of a monolayer graphene [75]. In conclusion, the PMMA-mediated graphene transfer process was successfully optimized to obtain a high quality monolayer graphene film on a SiO_2/Si substrate for fabrication of graphene

electronic devices, with minimal number and size of wrinkles and cracks which are inevitably generated during the transfer process.

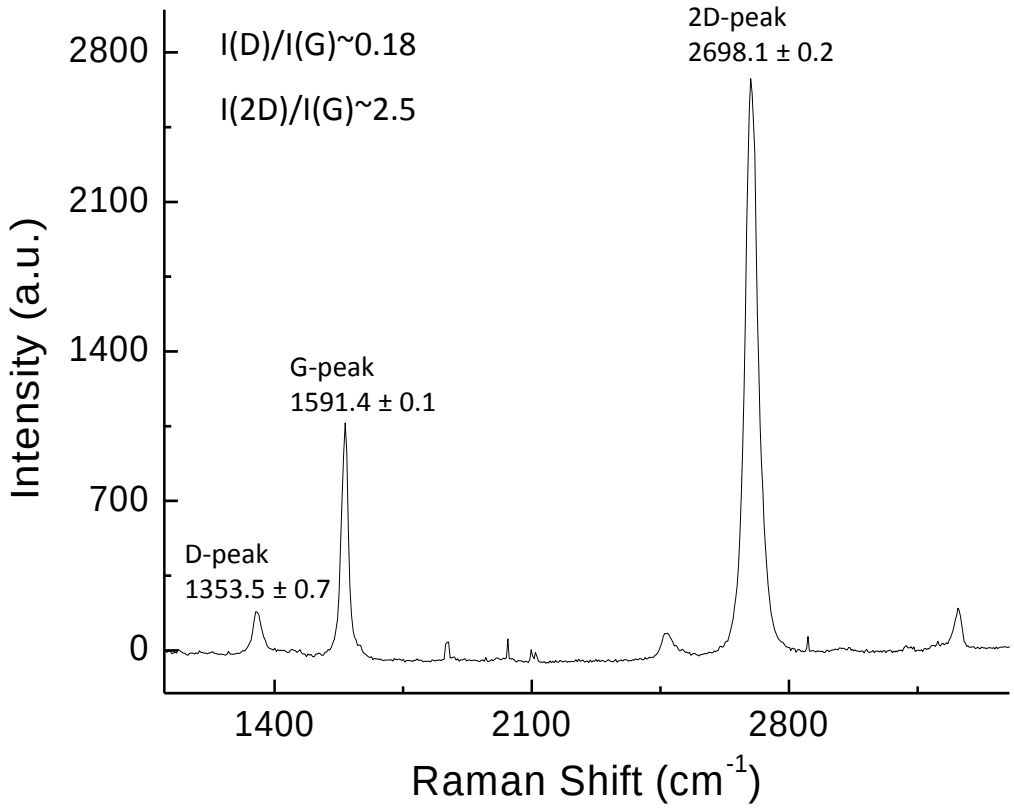

Figure 4.7. Raman spectrum of the graphene film in Figure 4.6(b), showing its structural quality and the number of graphene layers.

4.4 Theoretical investigation of interactions between FEBID carbon and graphene

First-principles calculations using density functional theory (DFT) were conducted to investigate the effect of sp^3-type graphene defects on molecular adsorption of FEBID produced hydrocarbon radicals and carbon on graphene. All the DFT calculations were done using a commercial package, Materials Studio. In DFT calculations, geometry optimization was performed using Generalized Gradient Approximation (GGA) Perdew-Burke-Ernzerhof (PBE) functional [64,65,76] for the exchange correlation potential of interaction electrons with double

numerical basis set in the DMol3 [77]. Self-consistent field (SCF) convergence, 10^{-5} Ha, was obtained at 9x9x1 Monkhorst-Pack (MP) k-point grid [78].

4.4.1 Formation of electron beam induced sp^3-type defects on graphene

Figure 4.8(a) shows a side view of a 4x4 supercell of graphene with one puckered carbon atom, which is defined as a sp^3-type defect characterized by its height, *h*. This type of a structural defect in graphene can be generated by supplying external energy greater than its formation energy. One of the external energy sources can be high energy electron irradiation. When an electron strikes a carbon atom of graphene, it transfers energy and can resultantly form a defect on graphene depending on transmitted energy. The maximum transferrable energy by an electron to carbon can be estimated based on the Mckinley-Feshbach approximation, $T_{max}=2E(E+2m_ec^2)/Mc^2$, where E is a striking electron energy, m_e is a mass of an electron, M is a mass of a carbon atom and c is a speed of light [79,80]. For examples, the maximum energy of 4.8 eV can be transferred by an electron striking graphene with energy of 25 keV, which is a typical energy of primary electrons in FEBID. Figure 4.8(b) shows the formation energy (E_f) of sp^3-type defect on graphene, which is the energy required to generate the defect and also indicates how much energetically unstable the graphene's structure is. The formation energy is calculated as the total energy difference between defected and defect-free graphene, $E_f=E_{total}$(defected)–E_{total}(defect-free) [81]. The defected graphene was characterized by a defect height, *h*, which is a parameter input to the DFT calculations. As the defect height increases, the formation energy rapidly increases, indicating that much more external energy is required for defect generation. Because of local increase in lattice energy upon defect formation, this state of graphene is thermodynamically unstable, and a foreign species can be strongly adsorbed to the defect site in order to energetically stabilize the graphene structure. As marked in Figure 4.8(b), the defect with height up to 0.85 Å can be generated with the electron energy of 25 keV.

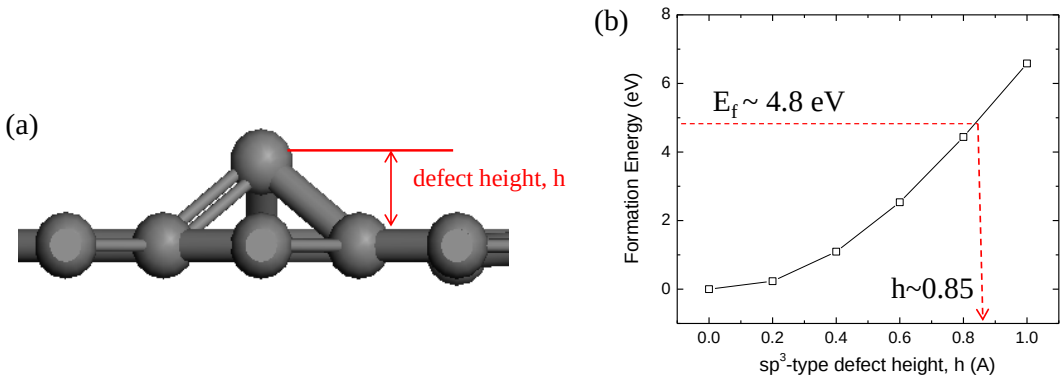

Figure 4.8. (a) A side view of 4x4 supercell of graphene with a sp^3-type defect height, h, and (b) the formation energy of the defect on graphene upon increasing height as a parameter input for DFT calculations.

4.4.2 DFT simulations of the effect of electron beam induced sp^3-type graphene defects on molecular adsorption

Density functional theory (DFT) calculations were performed to study adsorption of an isolated CH_3 radical onto a 4x4 supercell of graphene. A CH_3 radical is first in a sequence of intermediate species CH_n (n=1,2,3) in transformation of methane precursor (CH_4) to atomic carbon (C) by FEBID process. As a reference state, CH_3 radical is placed on top of a carbon atom of graphene with the initial distance ~ 3 Å [82]. Adsorption structures were obtained for various sp^3-type defect heights (h) on graphene used as a configuration input parameter in DFT calculations to define the threshold height leading to chemisorption. To assess only the effect of the defect height on adsorption, we fixed the coordinates of all carbon atoms in defected graphene, while a CH_3 radical was not constrained. Figures 4.9(a) and 4.9(b) show a representative physisorption state of a CH_3 radical on a defect-free graphene and its chemisorption state on the defected graphene, respectively, which was obtained through the DFT calculations. The two different adsorption states depend on defect heights determining reactivity of a CH_3 radical to graphene. In order to investigate the effect of defect heights on adsorption of CH_3 to graphene, the binding distance ($d_{Gr\text{-}CH3}$) and energy (E_b) were plotted in Figure 4.9(c). The

binding distance was defined as the distance between CH_3 and graphene denoted in Figure 4.9(a). The binding energy (E_b) is calculated as $E_b=E_{total}$(hybrid system)$-E_{total}$(graphene)$-E_{total}(CH_3)$ [78]. It shows a threshold *h*-value for chemisorption is ~0.37 Å. Below this threshold height, CH_3 physisorbs on graphene with the binding distance (d_{Gr-CH3}) over ~3 Å and the binding energy (E_b) below ~120 meV [83]. Otherwise, it chemisorbs on graphene with more than 13 times greater binding energy than that for the physisorption state. In Figure 4.9(d), the total energy for each structure is plotted to define the energy barrier for transition from physisorption to chemisorption *via* formation of a sp^3-type defect. The energy barrier was found as ~0.9 eV, which corresponds to the formation energy of a sp^3-type defect with *h*~0.37 Å as shown in Figure 4.8(a). It implies that chemisorption of a CH_3 radical can be facilitated by exposing graphene to the energetic primary beam electrons with energy of at least ~ 5 keV, leading to formation of structural defects with *h*~0.37 Å on graphene as active sites for chemisorption. Therefore, the primary electron energy of 25 keV (transferring 4.8 eV to a carbon atom of graphene), which is typical for the primary beam in FEBID, is enough to establish chemisorption of a CH_3 radical to graphene. It is worth to note that the transfer energy for the 25 keV electron is not large enough to generate the SW defects or a knock-on damage (vacancy formation) in graphene, which have energy barriers of 10 eV and 18-20 eV for their formation, respectively [79]. Thus, it can be expected that the primary electrons with energy of 25 keV generate sp^3-type defects on graphene which along with simultaneous dissociation of CH_4 molecules to CH_3 radicals by secondary electrons results in chemisorption of CH_3 onto graphene. Once CH_3 is chemisorbed, sequential dissociation of H atoms by secondary electrons can lead to covalent bonding of each intermediate species CH_n (n=1,2) to graphene, as shown in Figure 4.9(e). The final product of an FEBID sequence with the CH_4 precursor is a carbon atom covalently bound on the bridge site (C-C bond) of graphene [66-68,79] with very strong binding energy of ~2.4 eV, which is much stronger than that of the 'side-

contact' of Ti to graphene and comparable to that of the 'end-contact' of Ti to graphene known to have the lowest contact resistance among various candidates of a conventional metal contact.

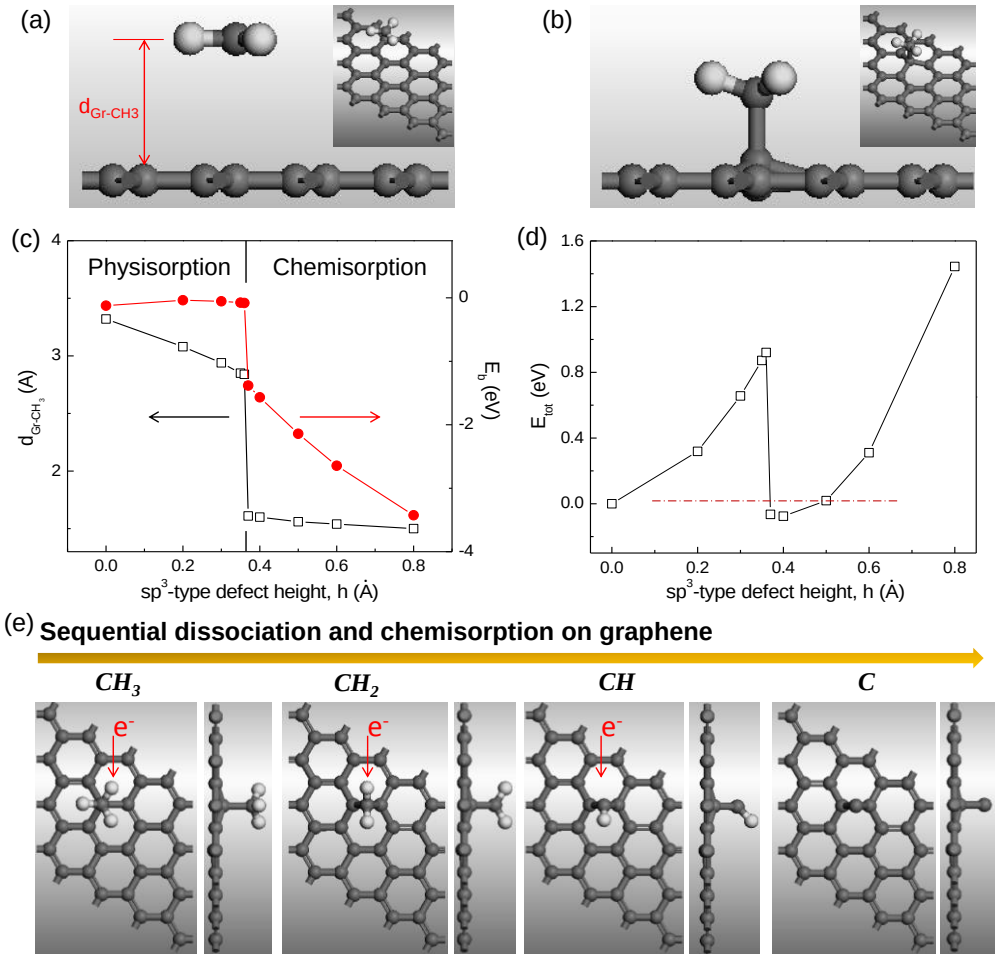

Figure 4.9. Adsorption states of a representative FEBID radical (CH_3) on graphene: (a) Physisorption on defect-free graphene and (b) chemisorption on graphene with a sp^3-type defect site generated by high energy electron beam irradiation. Insets show the tilted views of the two adsorption structures.; (c) Demonstration of transition from physisorption to chemisorption with dramatic change in binding distance and energy, induced by an increase of the graphene defect height, and (d) total energy changes showing an energy barrier for transition to the chemisorption state; (e) Chemisorbed structures of FEBID intermediate species resulting from dissociation of methane precursor on graphene by sequential cleaving of H atoms.

4.5 Identification of FEBID carbon adsorption states (coupling) using Raman spectroscopy

Using DFT calculations, we showed two possible adsorption states of hydrocarbon radicals on graphene, depending on the primary electron energy and resulting formation of sp^3-type defects in graphene. To experimentally demonstrate different adsorption states of FEBID carbon deposits on graphene, we performed a complimentary Raman analysis of FEBID deposits on graphene. Raman spectroscopy is a standard tool for characterizing amorphous to crystalline carbon nanostructures [46,53,84]. In the Raman spectrum of carbon structures, signature characteristics are the G and D peaks appearing around 1500-1630 cm^{-1} and 1300-1400 cm^{-1}, respectively [46,53,70]. The G peak is related to in-plane bond-stretching of sp^2 carbon pairs [53]. The D peak is due to a breathing mode of sp^2 carbon atoms in sixfold rings and it requires defects for its activation. Thus, a D peak in the spectrum is indicative of disorder in graphene/graphite, as well as the presence of graphitic domains in amorphous carbon [46,53,74,84]. As-deposited FEBID carbon is an amorphous mixture of sp^2 and sp^3 sites with hydrogen content up to 60% [46,53]. It can be thought as a hybrid composite structure of two separate carbon materials, with different interactions between the domain of different bond hybridization. In a Raman spectrum, chemisorption of FEBID carbon (or intermediate hydrocarbon radicals) on graphene results in appearance of D peak due to the generation of sp^3-type defects in graphene, even in an absence of graphitic domains in the deposit itself [53,85]. On the contrary, in the case of physisorption, defect-free graphene does not have any contribution to the D peak, and as-deposited FEBID carbon with small content of graphitic domains will have no apparent D peak in the Raman spectrum [46,53]. Accordingly, the D peak in the Raman spectrum enables identification of the nature of adsorption states (*i.e.*, chemisorption vs. physisorption) of FEBID carbon on graphene.

4.5.1 FEBID carbon patterning on graphene

Using the optimized graphene transfer procedure developed in the previous session, a CVD monolayer graphene film was transferred to a 90 nm SiO_2/Si substrate. Six square-shaped carbon patterns were fabricated using FEBID on the graphene film using different primary electron doses with the electron beam energy of 25 keV and current ~30 pA, as shown in Figure 4.10(a) (FEI Quanta 200 ESEM at $P_{chamber}$~10^{-6} Torr). The low electron beam current was used to avoid electron beam-induced heating, which might graphitize the carbon deposits [86]. The electron dose was controlled by varying the electron beam dwelling time on a spot during FEBID patterning. We utilized an intrinsically present environmental hydrocarbon contamination adsorbed on graphene as a precursor source for FEBID process. In Figure 4.10, two distinct regions of carbon deposits can be identified after the electron beam exposure: (i) an intended FEBID carbon pattern of squares on graphene where the primary, high energy beam electrons (25 keV) impinged on the graphene surface, and (ii) unintentional parasitic "halo" carbon film around each square formed by low energy, secondary electrons (< 50 eV) [24,25]. It should be emphasized that the difference between these two types of carbon deposits is whether or not the high energy beam electrons were the first step in the deposition sequence, which as suggested by the DFT calculations generates defects on graphene and drives chemisorption of FEBID intermediate species.

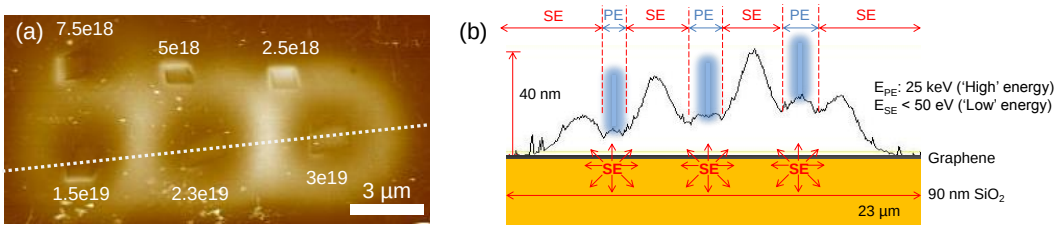

Figure 4.10. (a) AFM image of as-deposited FEBID carbon structures on CVD graphene, showing the patterned squares (with different electron beam dose in a unit of e^-/cm^2) and "halo" film around them, and (b) schematic illustration showing FEBID carbon deposition process with the AFM cross-sectional profile of the bottom row FEBID carbon structure along the dotted line in (a). (PE: primary electron, SE: secondary electron)

4.5.2 Raman laser-induced thermal ablation of parasitic carbon contaminations on graphene

Laser-induced thermal ablation is known to effectively remove FEBID carbon and thus improve deposited material purity and pattern resolution [87]. In particular, Raman laser was found to effectively and locally ablate FEBID carbon deposits on various substrates [70]. Exploiting this idea we utilized the Raman laser (514 nm Ar^+ ion laser with 5.5 mW power) to selectively get rid of the parasitic 'halo' carbon film. Figure 4.11(a) shows a sequence of optical images of as-deposited FEBID carbon on graphene and its removal *via* multiple laser exposures over the entire graphene area. Three consecutive laser thermal ablation experiments were performed, while collecting the Raman spectra at each step. Figure 4.11(b) shows the AFM topographic image of FEBID carbon on graphene after the 3rd laser exposure. After the 3rd laser exposure, most of the carbon "halo" film was removed with the reduction of the parasitic deposit thickness to vanishing levels. As shown in Figure 4.11(c), thickness of the primary beam irradiated square patterns also decreased by about 90% after the 2nd laser exposure, but the 3rd laser exposure did not lead to further noticeable changes in their thickness with an average height of residual pattern 0.8 ± 0.3 nm (RMS roughness: 0.29 ± 0.04 nm). It suggests that laser-induced thermal ablation can be an effective technique to remove the parasitic carbon deposits everywhere, and only a few atomic carbon layers of a desired pattern that has been exposed to high energy electron beam irradiation remain to be strongly bound to graphene.

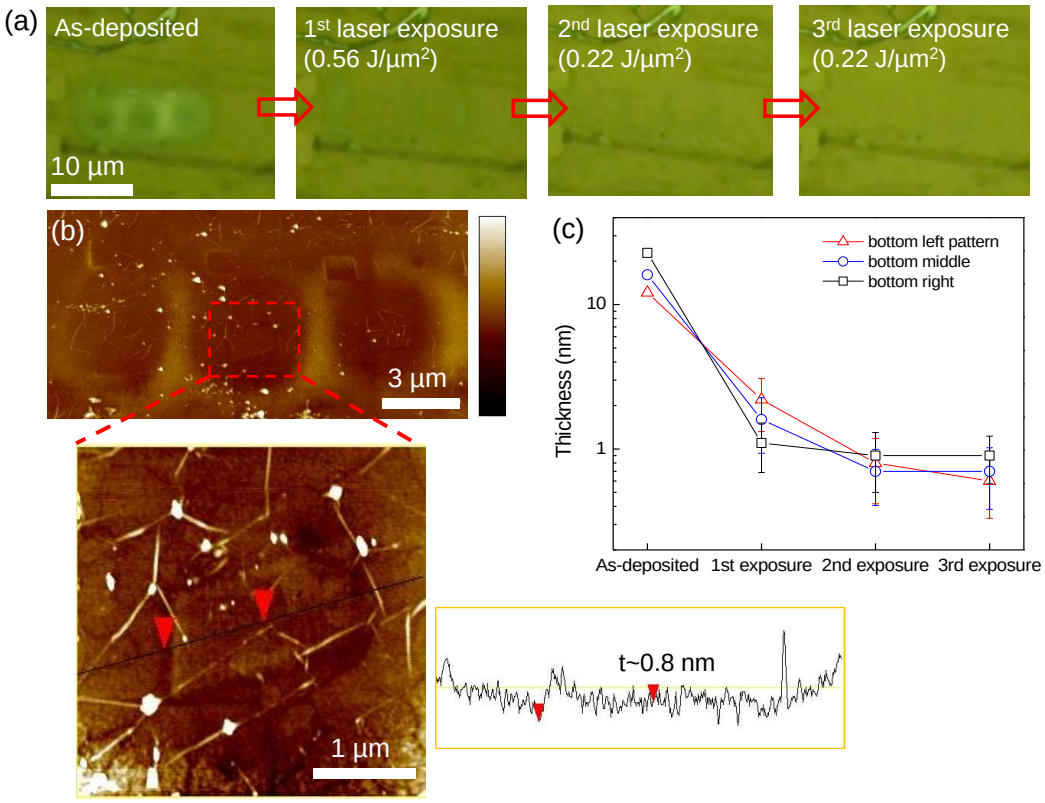

Figure 4.11. Visualization of FEBID-produced carbon deposits on CVD graphene: (a) Optical images qualitatively showing removal of the physisorbed carbon film by high power (5.5mW) laser ablation; (b) AFM image of the FEBID carbon structures after 3rd laser exposure (z-scale=50nm). The insets show the AFM image of the patterned carbon square (z-scale=8nm) and the cross sectional profile of the patterned carbon square thickness; (c) The change in the thickness of the bottom three patterned carbon squares upon the consecutive laser exposures.

4.5.3 Understanding of FEBID carbon adsorption states and deposit composition on graphene

Figures 4.12(a) and 4.12(b) are the Raman maps, showing the integrated intensity of the G peak over the spectral range from 1500 cm^{-1} to 1650 cm^{-1} and the D peak from 1350 cm^{-1} to 1450 cm^{-1}, respectively. The results indicate a much greater contrast between G and D peaks for the electron beam irradiated square patterns than for the unintentional film deposits. Composition of as-deposited FEBID carbon is generally similar regardless of electron beam conditions, such as beam current and energy [46], and even for different hydrocarbon precursors [88]. The number of

sp^2 bonds in the as-deposited FEBID carbon, which influence the G peak in the Raman spectrum, vary proportionally to the volume of deposits. Since the area of the laser spot is identical during all Raman measurements, the effect of the deposit volume on the Raman signal depends on the deposit thickness. As shown in Figures 4.10 and 4.11, the thickness of the square patterns is similar or smaller than the unintentional film deposits, and thus, the higher content of sp^2 sites (higher contrast of G peak map in Figure 4.12(a) in the patterned domains indicates the difference in FEBID carbon composition of the high energy beam irradiated areas, as compared to the "halo" film exposed to low energy electrons only. This suggests that carbon chemisorption occurs in the primary electron irradiated graphene sites vs. its physisorption in surrounding "halo" sites exposed only to the low energy secondary electrons. As revealed by the DFT calculations, this is an outcome of two distinctly different mechanisms of surface interactions between the FEBID intermediate radicals and graphene depending on whether it is pristine or has structural bond defects, induced by high energy electrons. In Figure 4.12(b), the higher contrast of the D peak is indicative of a more disordered carbon structure in the square pattern deposits. It can either result from generation of sp^3-type defects on graphene underneath of directly irradiated square deposits or may also appear due to the presence of graphitic domains in the deposited carbon [46,53,74].

Figures 4.12(c) and 4.12(d) represent the evolution of Raman spectra of graphene beneath the parasitic carbon "halo" film and patterned carbon areas, respectively, upon laser-induced thermal ablation. The Raman spectra for each patterned carbon areas are presented in the supporting information, providing the detailed analysis of the effect of electron beam dose on FEBID carbon formation on graphene. One can unambiguously identify the dissimilar adsorption states between the two regions. The spectrum of graphene covered by the "halo" carbon film in Figure 4.12(c) is similar to that of graphene itself with small D peak, and strong and narrow G and 2D peaks, which indicates the carbon film deposits have weak chemical coupling to graphene as expected for the physisorption state. In contrast, the spectrum of graphene areas covered with the high energy electron irradiated patterns, shown in Figure 4.12(d), features broad G and D peaks,

indicating that the FEBID carbon deposits strongly influence the spectrum even though the thickness of the square patterns (*i.e.*, the amount of deposited carbon) is less than that of the "halo" film. This supports the conclusion from DFT calculations that in the case of "halo" carbon film, which was deposited on electron-beam-unperturbed graphene and whose adsorption state is physisorption, the carbon deposit is weakly coupled to the substrate and does not induce any structural defects in graphene. Thus, no increase/activation of the D peak is expected in the carbon film-covered graphene Raman spectrum. Also, since graphene with sp^2 hexagonal lattice structure has higher Raman scattering cross section [53,89], the deposits with low content of sp^2 sites, due to the lack of graphitic domains [46,70], give small contributions to the G peak of the Raman spectrum even when a deposited carbon film is at least 50 times thicker than the graphene support itself.

In the case of the square carbon patterns whose adsorption state is chemisorption, the carbon deposits undergo local rehybridization of sp^2 to sp^3-like bonds of graphene upon exposure to high energy primary electrons, as shown by the DFT calculations. Accordingly, this increases the number of defects and, at the same time, also reduces the content of sp^2 hexagonal sites on graphene. Despite the reduction of intrinsic sp^2 hexagonal sites on graphene, the carbon deposition onto the defect sites contributes additional sp^2 carbon bonds in the form of chains or rings, which cumulatively increases the intensity and broadens the G peak. Additionally, a pronounced, broad D peak and appearance of D+D' peak (at ~2940 cm^{-1}) shown in the spectrum are the Raman signatures of amorphous carbon with imbedded nanocrystalline size of graphitic domains [46,74]. Therefore, we can conclude that chemisorption of intermediate hydrocarbon radicals and ultimately of the carbon deposit on high energy electron beam-impacted areas of graphene facilitates intimate coupling between the graphene substrate and FEBID carbon with an increased formation of sp^2 sites of graphitic domains.

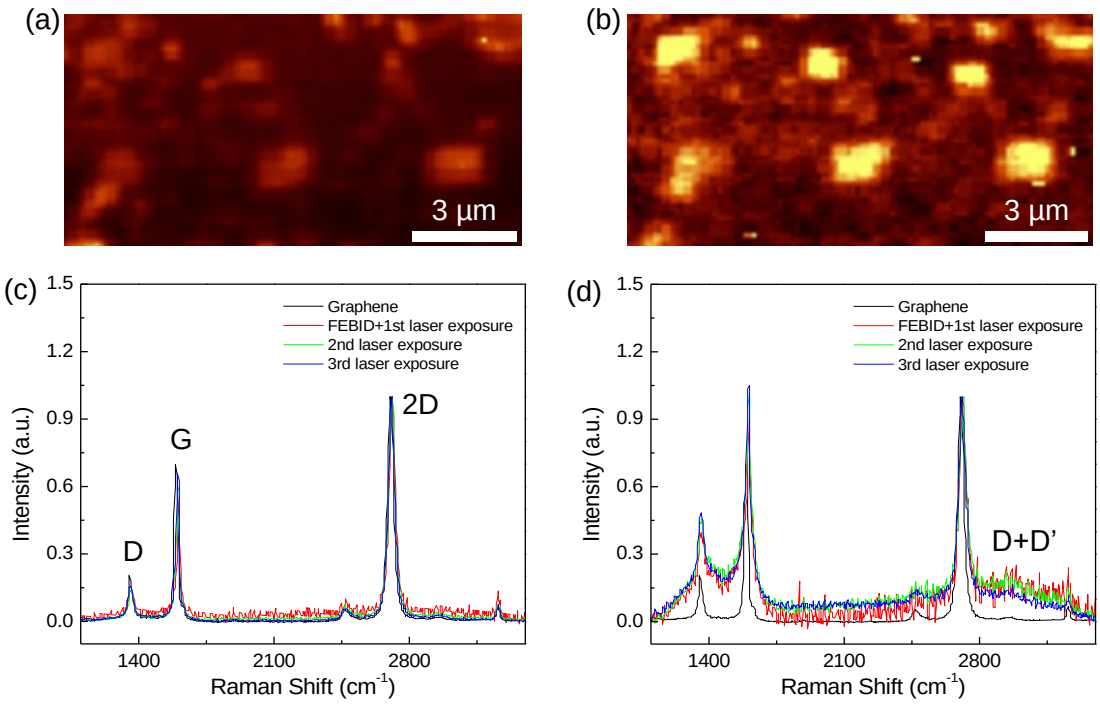

Figure 4.12. Raman maps showing the integrated intensity of (a) G peak and (b) D peak, and the Raman spectra for graphene areas covered with (c) physisorbed "parasitic" FEBID carbon and (d) chemisorbed FEBID patterned carbon squares, upon consecutive laser exposures.

To quantify the difference between the two types of carbon deposits onto graphene, the D to G peak intensity and area ratios, denoted as I(D)/I(G) and A(D)/A(G), are plotted in Figures 4.13(a) and 4.13(b), respectively. The intensity ratio is generally used as a measure of point-like defects on graphene,[37,38] while the area ratio can be used to determine the composition of amorphous carbon [46,53,70]. In Figure 4.13(a), the intensity ratio changes little in the graphene areas covered with the carbon "halo" film, but it profoundly increases in the graphene areas with the carbon square deposits which were irradiated by high energy primary electrons. This further supports the conclusion about differences in the adsorption state of carbon deposited onto graphene areas which have (*i.e.*, chemisorption sites with strong carbon-graphene interactions) and have not (*i.e.*, physisorption sites with weak carbon-graphene interactions) been exposed to

direct irradiation of high energy electron beam, owing to formation of structural defects in graphene substrate during the FEBID process. Interestingly, subsequent annealing *via* laser exposure essentially fully removes carbon from the physisorbed film areas, but does not make a significant change in the Raman peak intensity ratio for both physisorbed and chemisorbed carbon deposit states.

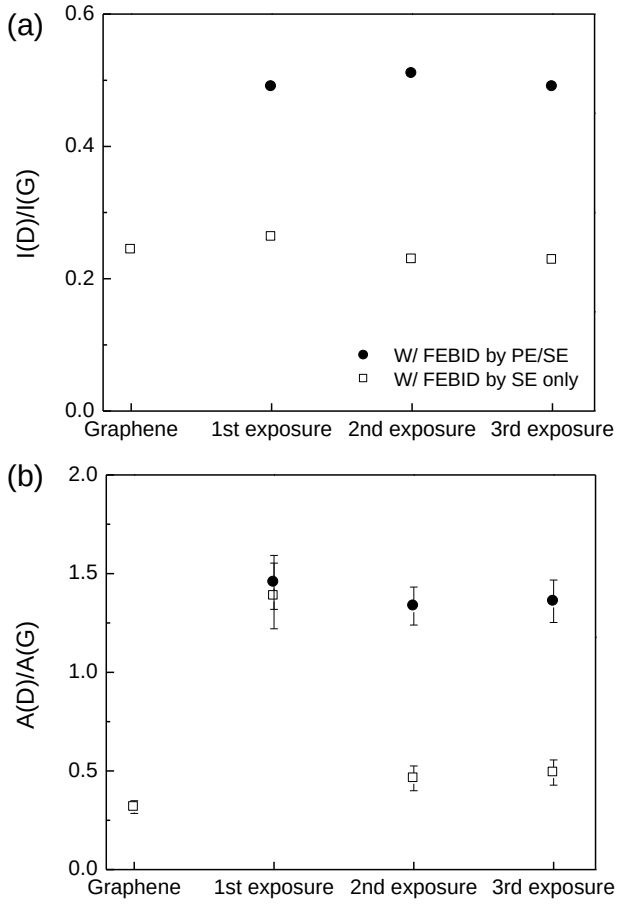

Figure 4.13. Change of (a) intensity and (b) area ratios of the D to the G peaks for graphene areas with FEBID carbon deposits exposed to both high energy primary electrons and low energy secondary electrons (FEBID by PE/SE, shown using filled symbols) and those exposed to secondary electrons only (FEBID by SE only), showing the progression through multiple laser exposures for thermal ablation.

In Figure 4.13(b), the D to G peak area ratio, A(D)/A(G), increases to ~ 1.4 after deposition and 1st annealing step *via* laser exposure for both the physisorbed carbon film and chemisorbed carbon squares. However, after additional laser exposures (2nd and 3rd), A(D)/A(G) for the physisorbed carbon film is noticeably decreased close to that of pristine graphene due to ablation of weakly bound carbon film, which is the source of perturbations for the graphene Raman spectrum. It indicates that laser-induced thermal ablation of physisorbed "halo" carbon deposits does not damage graphene and could be potentially used as a safe means for cleaning the graphene layer from carbon "contaminants" of the electron beam patterning process. In contrast, for the chemisorbed carbon, there is no significant change of the A(D)/A(G) ratio around 1.3~1.5 upon consecutive laser exposures, which indicates that the laser annealing do not alter the compositions of the chemisorbed carbon structure. It suggests that only a few layers of as-deposited carbon atoms remain on the surface covalently bound to graphene and contribute to the Raman spectrum. The area ratio indicates that the chemisorbed carbon is amorphous with graphitic cluster size of ~1.7 nm [53], confirming that chemisorption of electron-stimulated dissociation precursor radicals onto graphene leads to graphitization of FEBID carbon deposits.

4.5.4 Effect of primary electron beam dose on chemisorption of FEBID carbon on graphene

Figure 4.14(a) shows the change of the Raman spectrum by increasing the electron dose (on each pattern). In Figures 4.14(b) and 4.14(c), significant features of the Raman spectrum are plotted to investigate the evolution of carbon deposit composition upon increasing the electron dose. Initially, graphene has a small amount of defects with I(D)/I(G)~0.24 and A(D)/A(G)~0.32, indicating the distance (L_D) between two defects around 24 nm [74]. FEBID of carbon with electron dose up to 5e18 e^-/cm^2 increases the number of defects on graphene with I(D)/I(G)~0.8 representing L_D ~12.5 nm. Interestingly, I(D)/I(G) decreases to ~0.55 (L_D~15 nm) after further increase of the electron dose and converges to ~0.45 (L_D~16.7 nm) for the electron dose over 1.5e19 e^-/cm^2, while A(D)/A(G) continues to increase and reach ~1.5. In Figure 4.14(c), both

peaks are broadened by carbon deposition, which indicates the existence of carbon structure with sp^2 carbon bonds and graphitic domains [53]. Increasing the electron dose from 5e18 e^-/cm^2 to 7.5e18 e^-/cm^2, the FWHM of the D-band peak increases about 110%, whereas the FWHM of the G-band increases only slightly. However, the A(D)/A(G) in Figure 4.14(b) increases only 20%. It is due to an increase of the G-band peak height and a decrease of the D-band peak height, which is represented by the reduction of the I(D)/I(G) in Figure 4.14(b). The same trend can be found when the electron dose increases from 7.5e18 e^-/cm^2 to 1.5e19 e^-/cm^2. For the electron dose beyond 1.5e19 e^-/cm^2, the FWHM of the G and D-band peaks and the I(D)/I(G) do not change noticeably, resulting in the negligible change of the A(D)/A(G).

Based on the Raman analysis, we propose a mechanism about the formation of FEBID carbon nanostructure on graphene. At the early stage of deposition up to the electron dose of 5e18 e^-/cm^2, sp^3-type defects on graphene with chemisorption of carbon atoms are generated by energetic electron irradiations and dissociation of hydrocarbon precursor molecules, resulting in the increase of the I(D)/I(G) and the A(D)/A(G). At the intermediate stage of deposition with the electron dose between 5e18 e^-/cm^2 and 1.5e19 e^-/cm^2, a fraction of the chemisorbed carbon atoms are detached from the graphene surface by strong interactions with additionally deposited carbon atoms forming graphitic domains, which leads to the reduction of the I(D)/I(G) and a significant increase of the D-band peak width. At the final stage of deposition when the electron dose exceeds 1.5e19 e^-/cm^2, additional carbon deposition no longer influences composition of the deposited carbon structure as well as the defect density on graphene. The proposed deposition mechanism highlights the controllability of chemisorption of carbon atoms on graphene using FEBID, which is critical for direct-write nanopatterning applications.

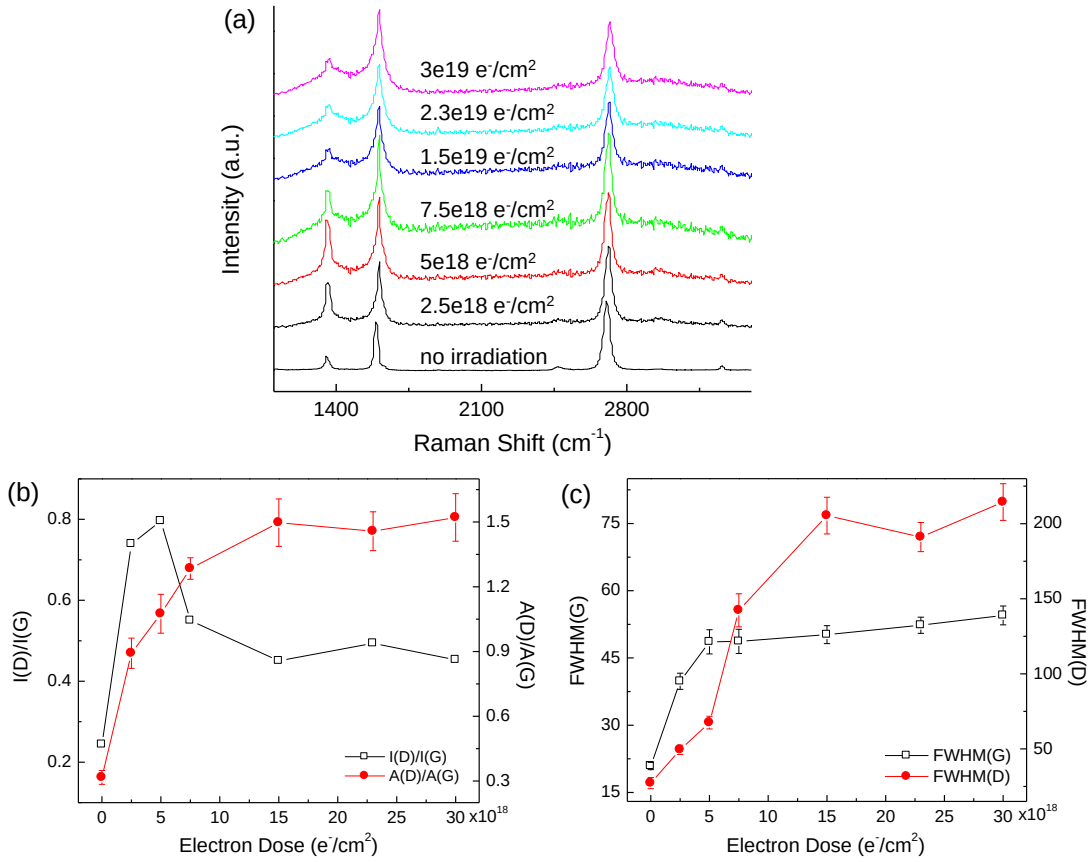

Figure 4.14. (a) Evolution of Raman spectra for the chemisorbed carbon structure on graphene supported by SiO_2/Si substrate upon an increase of the electron dose used for FEBID carbon square patterning, and quantification of spectral features with (a) the D to G intensity and area ratios, denoted as I(D)/I(G) and A(D)/A(G), respectively, and (b) the full width half maximum (FWHM) of the G and D-band peaks.

4.5.5 Control experiments: FEBID carbon deposition on bare SiO_2/Si

As a control experiment to demonstrate a role of graphene substrate on FEBID carbon deposition, we deposited FEBID carbon on a bare SiO_2/Si support with the same electron beam conditions used for the deposition on graphene, as shown in Figure 4.15(a). Figure 4.15(b) shows Raman spectra for each square pattern (different electron dose) along with average deposit thickness ($t_{FEBID\ carbon}$). No representative peaks, the G-band and D-band peaks, can be found for the deposits below the thickness of ~8 nm, meaning the absence or very little contents of sp^2

carbon bonds. The square patterns thicker than ~8 nm start to show the representative Raman peaks for amorphous carbon and all the Raman spectra have the same signature features of no apparent D-band peak and very broad G-band peak with the area ratio of the D to the G-band peaks close to unity, A(D)/A(G)~1, indicative of an amorphous carbon structure with no graphitic domains [46]. This stresses that the electron beam conditions used in this study do not induce any thermally-induced graphitization of FEBID carbon itself, but the defects on graphene generated by primary electron irradiation play a role of chemisorption sites for FEBID carbon resulting in graphitic domains inside the FEBID carbon square patterns.

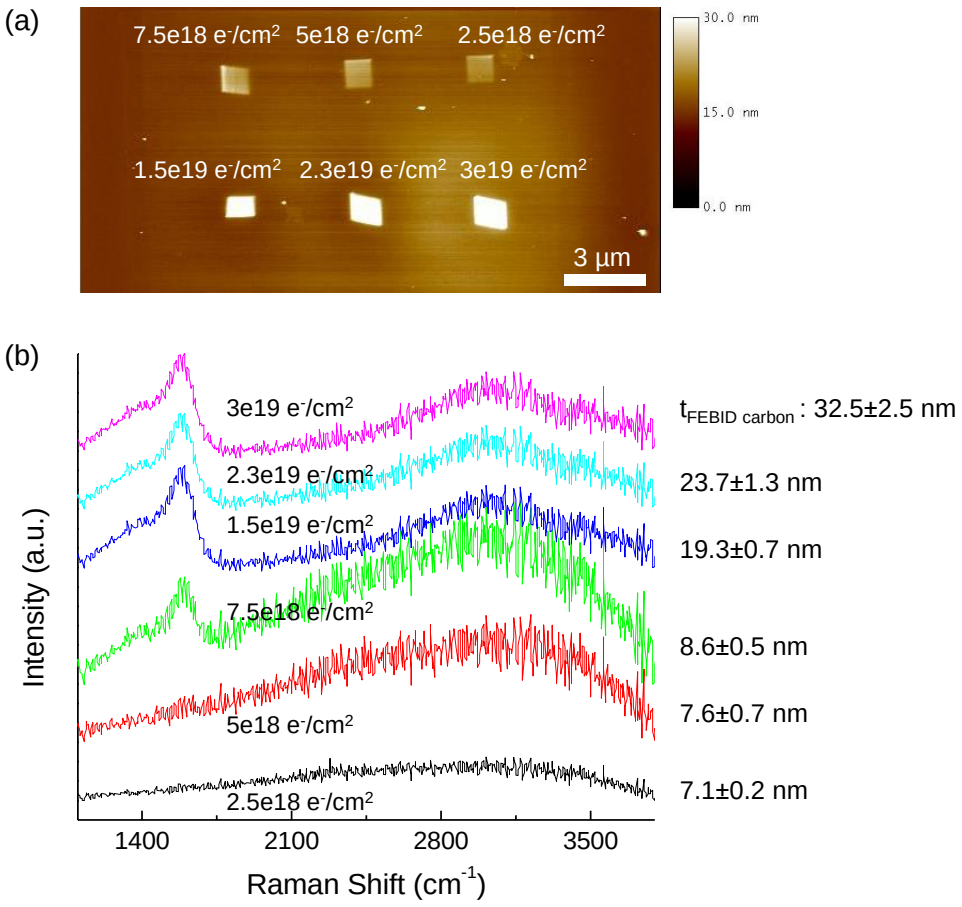

Figure 4.15. (a) Control experiments: AFM image of six FEBID carbon square patterns deposited on the SiO_2/Si substrate with various electron beam doses, and (b) the corresponding Raman spectra for each carbon square with an average thickness of the carbon depsoited ($t_{FEBID\ carbon}$) indicated in the legend.

In order to further confirm this, a rectangular shape of a FEBID carbon pattern (4 µm x 1 µm) was deposited across the transition zone going from the bare SiO_2 substrate to the graphene/SiO_2, as shown in Figure 4.16(a). Electron beam conditions were set to the beam energy of 25 keV and current ~30 pA for the beam dwelling time of 0.4 s on a spot, which correspond to the electron dose of 8.3e18 e^-/cm^2. Figures 4.16(b) and 4.16(c) are the Raman maps, showing the integrated intensity of G-band and D-band peaks over the spectral range from 1100 cm^{-1} to 1800 cm^{-1} and the 2D-band peak from 2600 cm^{-1} to 2800 cm^{-1} to identify the graphene region on the SiO_2 substrate, respectively. In Figure 4.16(b), the region 2 (FEBID carbon on graphene/SiO_2) shows a much higher Raman intensity than the region 1 (FEBID carbon on bare SiO_2) as well as pure graphene (no FEBID deposit) even though the thickness of the deposits is similar in two regions. This distinction in the Raman spectra of similar thickness deposits clearly supports the role of e-beam irradiated graphene as source of chemisorption sites for FEBID carbon *via* generation of defects upon exposure to the high energy primary electrons.

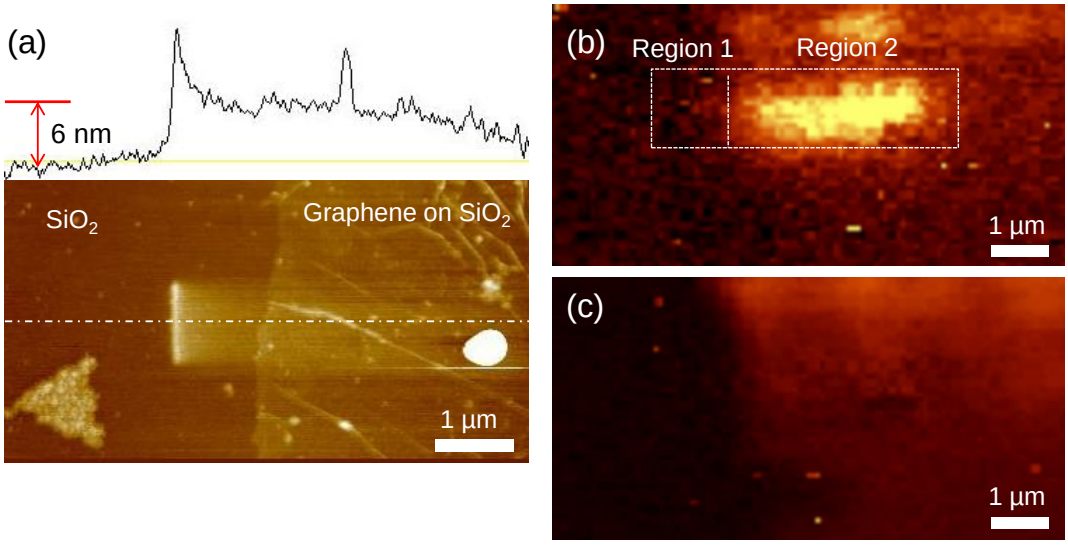

Figure 4.16. (a) AFM image of FEBID carbon deposited across the transition zone going from the base SiO_2 substrate (Region 1) to the graphene supported on the SiO_2 substrate (Region 2), and the Raman maps showing the integrated intensity of (b) G-band and D-band peaks and (c) 2D-band peak in all domains.

4.6 Concluding remarks

In summary, we developed the optimized graphene transfer procedure for minimizing defects, cracks and wrinkles of a CVD monolayer graphene film, and thus suitable for fabricating high performance graphene electronic devices. Using a high quality graphene films as test substrates, we discovered two possible adsorption states of carbon deposits on graphene, which are fabricated by FEBID. Using DFT calculations, it was shown that the sp^3-type defects in graphene produced by high energy beam electrons form energetically-favorable sites for chemisorption of FEBID-produced intermediate hydrocarbon species onto graphene. The different adsorption states during the FEBID process were confirmed using Raman spectroscopy of FEBID carbon deposits in combination with post-deposition multi-step laser annealing/ablation. It was shown that weakly-coupled physisorbed FEBID carbon formed in the surrounding areas of graphene substrate with no direct exposure to high energy electrons can be effectively eliminated by laser-induced thermal ablation with no damage to graphene. In contrast, the chemisorbed FEBID carbon on the areas with graphene structural defects induced by electron beam irradiation "survives" laser ablation treatment in the form of a few atomic layers of carbon atoms covalently bonded to graphene. This study provides a fundamental insight into the interactions between FEBID-produced carbon deposits and graphene, which is foundational for electron-beam-based direct-write graphene nano-patterning. In combination with demonstrated post-deposition "cleaning" process using laser ablation to remove detrimental "halo" carbon deposits with graphene remaining intact, it establishes the FEBID as a novel tool for controlled covalent functionalization of graphene with applications to electronic device fabrication. Especially, it provides a means to remove an unintentionally deposited parasitic carbon film on graphene channel maintaining mechanical/chemical coupling of an intentionally deposited FEBID carbon interlayer to graphene.

CHAPTER 5

FEBID CARBON 'INTERLAYER' FORMATION AT CVD MONOLAYER GRAPHENE-METAL INTERFACES

5.1 Introduction

In the previous chapter, we elaborated on the nature of the interaction of FEBID carbon deposits (chemisorption of intended carbon patterns vs. physisorption of parasitic carbon deposits) with graphene, which suggests a method of control of interfacial coupling between graphene and FEBID carbon deposits. It is important in that we can achieve strong coupling between graphene and FEBID carbon deposits, while parasitic carbon contamination is weakly interacting with graphene and thus can be easily removed using post-deposition processes, such as laser-induced thermal ablation or possibly thermal annealing in air. In application of the FEBID technique to modification of graphene-metal interfacial properties in graphene electronic devices, this finding suggests the possibility of enhancement of coupling between graphene and metal with post-deposition removal of any parasitic carbon contamination on graphene conduction channel, which is inevitably generated during FEBID carbon contact fabrication.

In this chapter, we apply FEBID carbon interlayer fabrication technique to graphene-metal contacts as shown in Figure 5.1. First, we focus on a fundamental investigation of FEBID carbon interlayer formation between CVD monolayer graphene and metal with an assist of topological and compositional characterization techniques using AFM and Raman spectroscopy. It provides a set of direct evidences of the FEBID graphitic interlayer formation at the graphene-metal interfaces. Next, the fabrication protocol of FEBID graphitic interlayer is applied to graphene electronic devices, and its effect on improving electrical/thermo-mechanical properties of the device is demonstrated. In order to evaluate the effect of FEBID graphitic interlayer formation on contact resistance, transmission line method (TLM) measurements are performed, and

improvements of the contact resistance with the FEBID graphitic ‘interlayer’ formation are demonstrated.

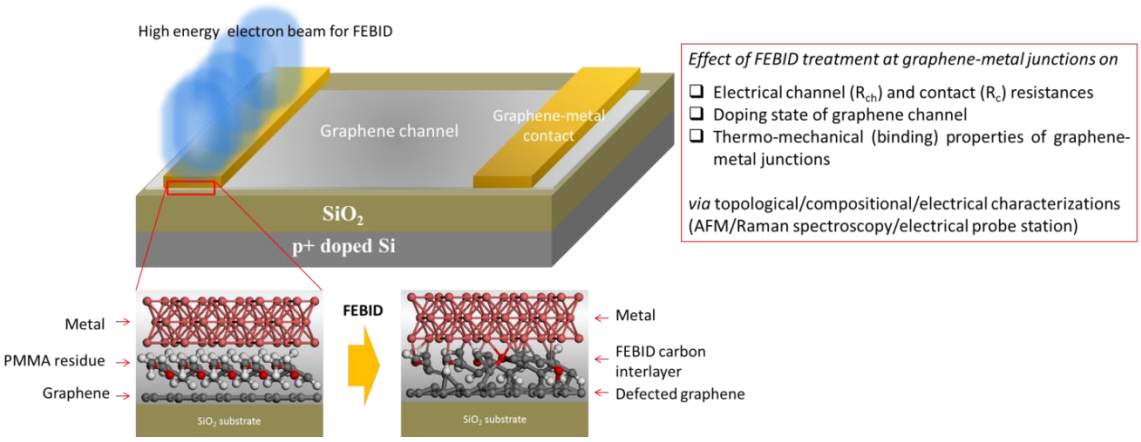

Figure 5.1. Schematic of graphene electronic device with FEBID contact modification, showing anticipated change of graphene-metal interface by FEBID, and summary of target outcomes of experiments demonstrated in this chapter.

5.2 FEBID graphitic interlayer formation between a CVD monolayer graphene and metal

In chapter 3, it was found that FEBID carbon ‘interlayer’ improves thermo-mechanical and electrical properties of mechanically exfoliated multilayer graphene and metal junctions. In this chapter, a comprehensive study is presented for in-situ observation and characterization of the FEBID graphitic interlayer formation between a CVD monolayer graphene and metal. AFM and a confocal Raman spectroscopy are used as primary tools for topological and compositional characterization of FEBID deposits.

5.2.1 Fabrication of metal contacts on a monolayer graphene

Using the optimized PMMA-mediated wet transfer method described in section 4.2, a monolayer graphene film was transferred onto a SiO_2/Si substrate. E-beam lithography was done

to make 10 µm by 10 µm square patterns for fabricating metal contacts on graphene. PMMA was used as a positive e-beam resist spin-coated on graphene supported by the SiO_2/Si substrate at 3000 rpm for 30 s, yielding a thickness of a PMMA layer ~ 300 nm. For e-beam lithography, Quanta 200 ESEM (FEI, Inc.) operated under ~ 10^{-6} Torr was employed with 'NPGS' (Nanometer Pattern Generation System) software. Electron beam conditions were set to spot size of 5 (~ 400 pA) and energy of 25 keV for a beam dwell time of 25 µs, corresponding to electron dose of ~400 µC/cm^2. After exposing PMMA layer according to the designed patterns, the PMMA layer was developed by soaking the substrate in methyl isobutyl ketone (MIBK) for 130 s as shown in Figure 5.2(a). Pattern development was terminated by soaking the substrate in isopropyl alcohol for 30 s and washing it in DI water for 30 s. Before depositing Cu, the surface morphology of the patterned area was measured using AFM, as shown in Figure 5.2. Very thin PMMA residues with 2~3 nm thickness generally remain after development of the patterns which degrades the quality of metal contacts on graphene. However, the residues are useful for modifying the interfacial property of graphene and metal interface, since they can be utilized as hydrocarbon precursors for FEBID carbon deposition resulting in graphitic interlayer formation. Figures 5.2(b) and (c) shows the AFM images of the surface morphologies for two representative developed patterns. They show the significant amounts of the PMMA residues remain after the development of the patterns, with ~2.2 nm root mean square (rms) roughness for both patterns. Finally, Cu was deposited on the substrate using e-beam evaporator, followed by the lift-off process to remove Cu everywhere except the pattern areas. Figure 5.2(d) shows the SEM image of a representative Cu pattern after completion of the lift-off process.

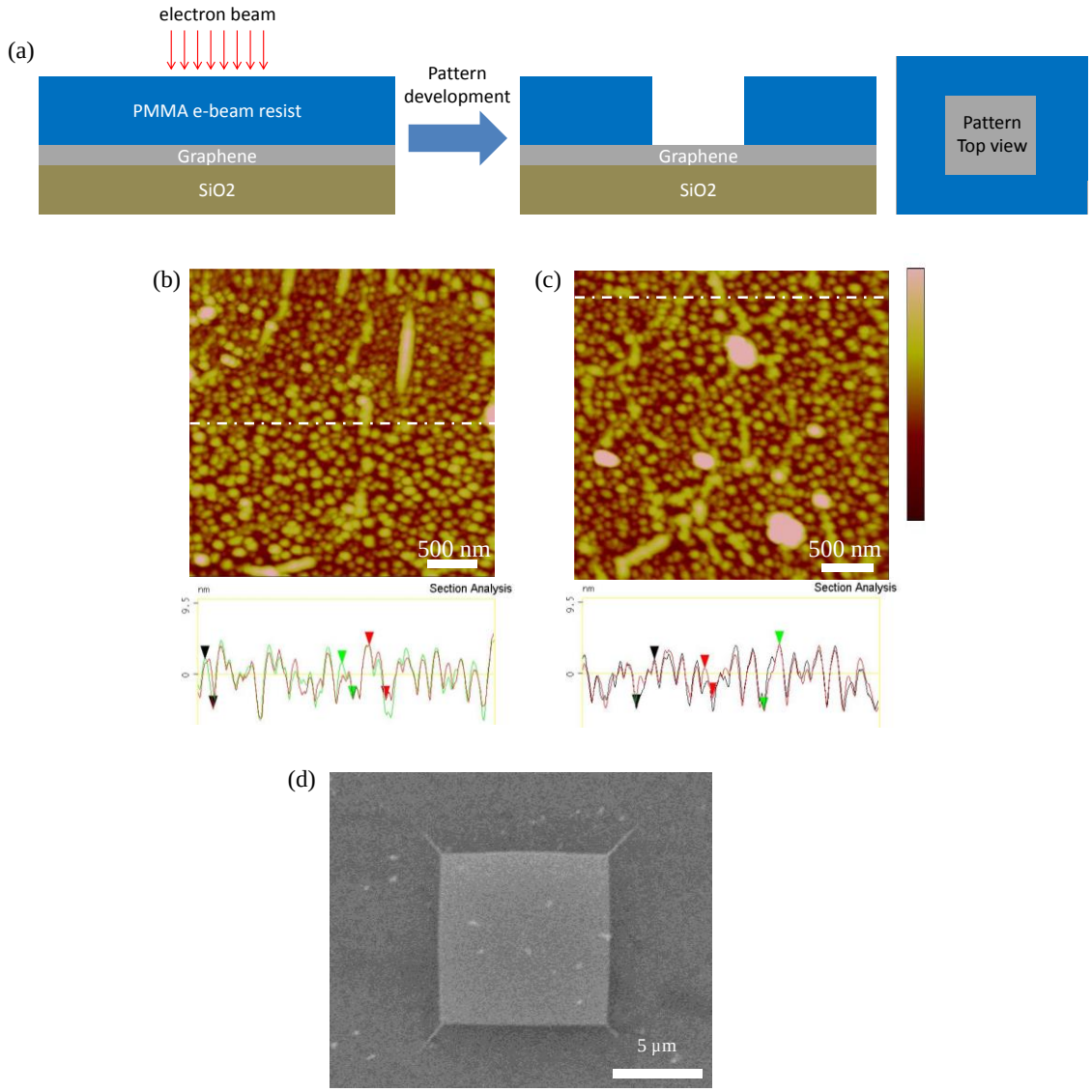

Figure 5.2. (a) Schematic of electron beam lithography for pattern generation before metal contact deposition. (b), (c) AFM images of surface morphology for two patterns on graphene after PMMA development and removal. Z-scale of the AFM images is 20 nm. (d) SEM image of a Cu pattern on graphene supported by the SiO_2/Si substrate.

5.2.2 Evidences for FEBID graphitic interlayer formation between graphene and metal

Figure 5.3 shows how FEBID treatment was conducted on the Cu pattern. Each row of three square patterns (1µm x 1 µm) was exposed to different electron beam dose with electron beam energy of 25 keV. The same process was applied to both the two Cu patterns. Figure 5.4 shows

the SEM images of the samples #1 and #2 treated with FEBID and a reference pattern without FEBID exposure. The sample #1 (Figure 5.4(a)) was exposed to the electron beam doses of 1.5 e18 e^-/cm^2 (e-beam dose 1), 1.5e19 e^-/cm^2 (e-beam dose 2), and 1.5e20 e^-/cm^2 (e-beam dose 3). The sample #2 (Figure 5.4(b)) was treated by electron beam with three consecutive doses: 7 e17 e^-/cm^2 (e-beam dose 1), 5e18 e^-/cm^2 (e-beam dose 2), and 5e19 e^-/cm^2 (e-beam dose 3). The Pt/C nanopillars were deposited at the two corners of the Cu patterns to identify the location of the patterns after etching Cu.

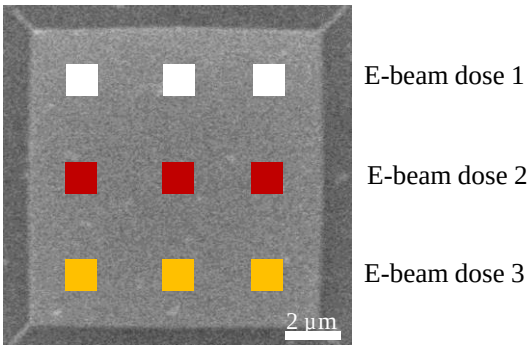

Figure 5.3. Schematic of FEBID treatment on the Cu pattern with three different electron beam doses.

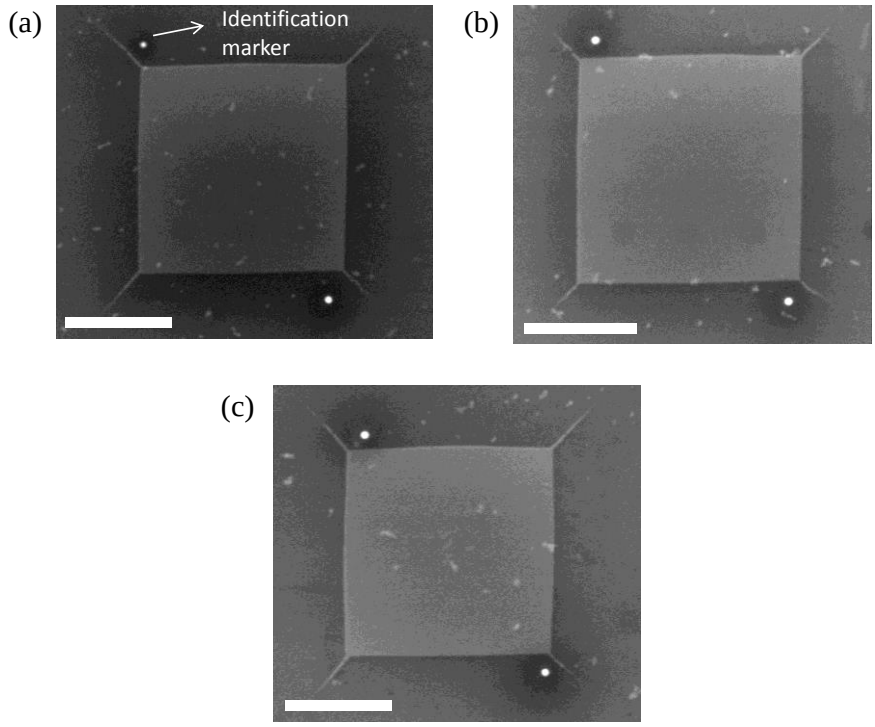

Figure 5.4. SEM images of the Cu patterns with Pt/C identification markers with FEBID ((a) sample #1 and (b) sample #2) and (c) without FEBID as a reference for comparison. Scale bar: 5 µm.

In order to investigate the change of interfacial properties by FEBID interlayer formation, the Cu patterns were selectively etched by 0.05 g/mL of ammonium persulfate in DI water. The sample substrate was placed in the etching solution heated on a hot plate at 40 ˚C and taken out from the solution after a variable etching time, followed by dry air blow. The thickness of the Cu patterns was measured using AFM. Figure 5.5 shows the change of thickness upon etching of Cu with an increase in the etching time. Results clearly show that a significant amount of the Cu patterns remain adhered to graphene after FEBID treatment, while the Cu pattern (as a control) was totally dissolved without FEBID exposure. The presence of Cu was confirmed by the EDX (energy-dispersive X-ray spectroscopy) measurements in Figure 5.6. It implies that Cu strongly adheres to graphene *via* formation of the FEBID carbon interlayer, thus enhancing mechanical and chemical binding between Cu and graphene, while Cu as-deposited on graphene without FEBID has a weak physical (*i.e*. *via* van der Waals forces) binding to graphene. The difference of

thickness of the Cu patterns observed between the two samples is due to the different total electron beam irradiations for FEBID treatment. The average electron dose on the entire Cu pattern is defined as total number of delivered primary electrons divided by a total area of the Cu pattern (10 μm × 10 μm), and it is 5e18 e^-/cm^2 and 1.7e18 e^-/cm^2 for the samples #1 and #2, respectively.

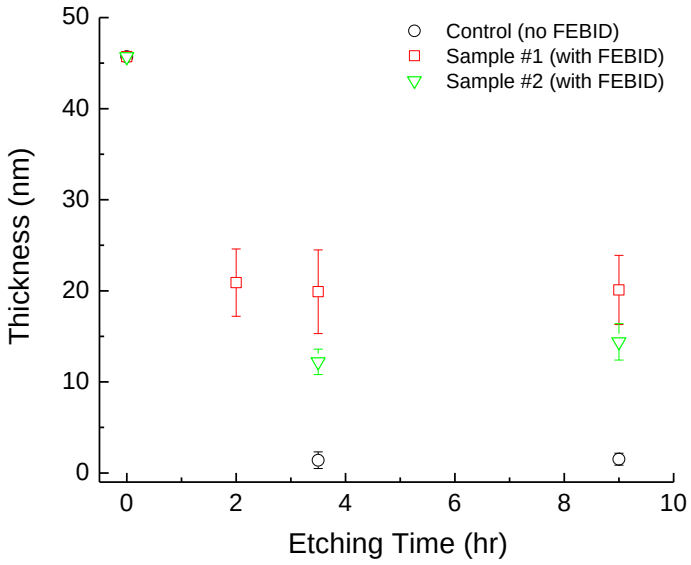

Figure 5.5. Change of the Cu thickness on increasing time of the selective Cu etching, indicating formation of the FEBID carbon interlayer between metal and graphene with enhanced interfacial chemical binding.

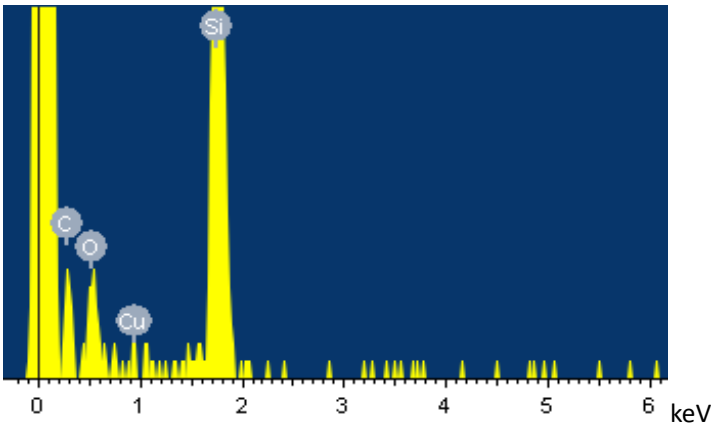

Figure 5.6. EDX compositional analysis of the sample #1 after 9 hrs of Cu etching, showing the presence of Cu in FEBID treated samples.

Figure 5.7 shows the corresponding AFM images of the Cu patterns after 3.5 hrs etching. Figures 5.7(a) and (b) show the Cu patterns remained with FEBID treatment, and Figure 5.7(c) results are for without FEBID treatment. The insets of Figure 5.7(c) are the zoomed-in AFM image of graphene surface and the corresponding cross-sectional profile with the rms (root mean square) surface roughness of 2.1±0.2 nm. Highly rough surface is due to the PMMA residue resulted from the e-beam lithography of the patterns for Cu deposition. Interestingly, the surface morphology and the rms roughness are similar to those before Cu metallization in Figure 5.1. It confirms complete etching of the Cu pattern without FEBID treatment, which implies that a conventional metallization method (in this case, e-beam evaporator) can have only a weak binding to the PMMA residues and graphene.

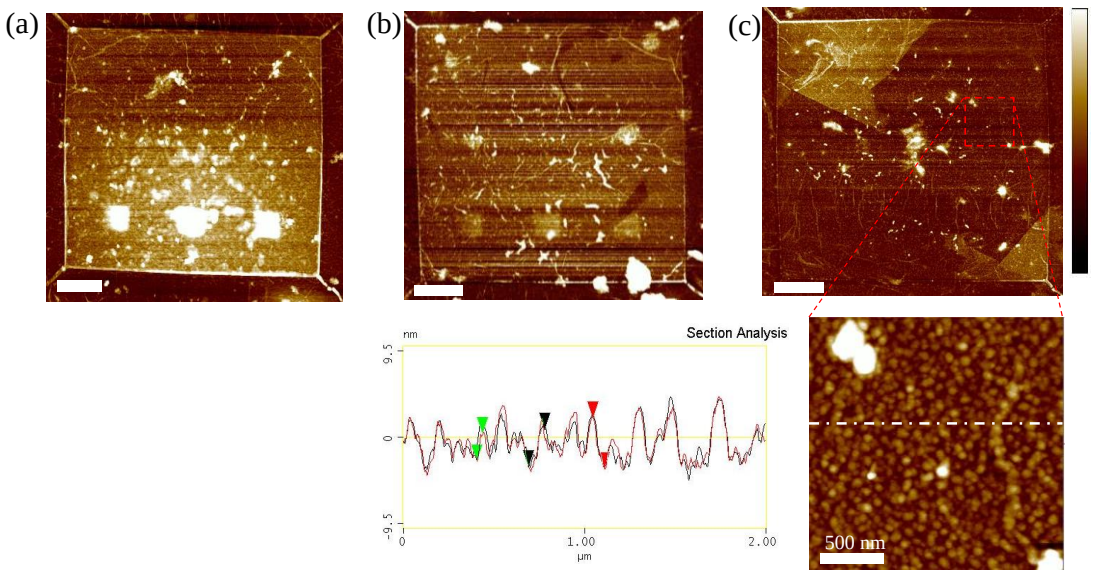

Figure 5.7. AFM images of the samples with FEBID treatments ((a) sample #1 and (b) sample #2) and (c) without FEBID treatment, after 3.5 hrs Cu etching. Scale bar and z-scale of the images are 2 µm and 50 nm, respectively. The insets are the zoomed-in image of Figure 5.7(c) and the cross-sectional profile of the surface morphology, showing the PMMA residues generated during e-beam lithography for Cu deposition. Z-scale of the inset image in Figure 5.7(c) is 20 nm.

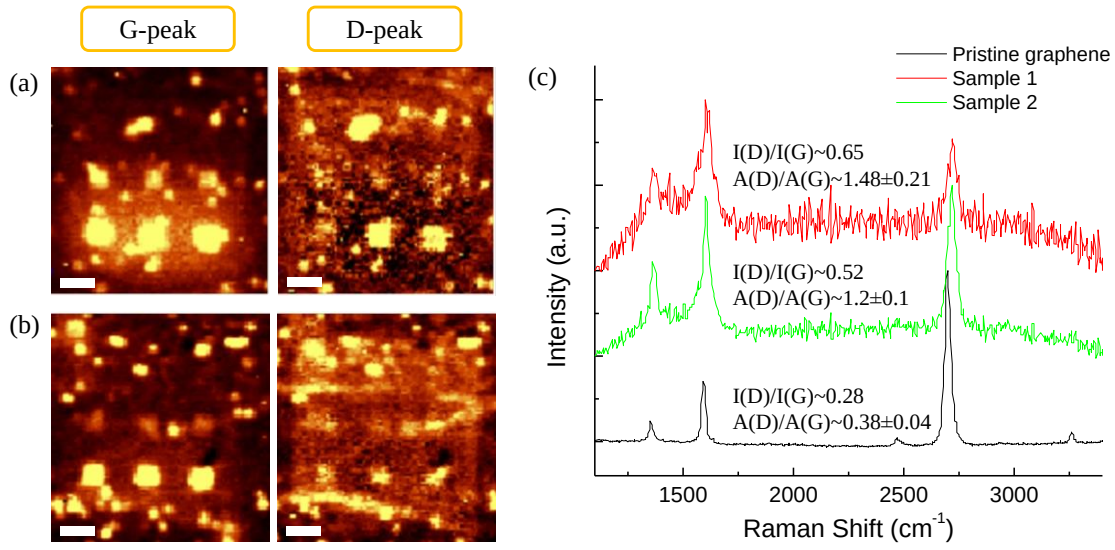

Figure 5.8. Raman maps of G and D peaks for (a) sample #1 and (b) sample #2, distinctly showing FEBID treated square patterns as graphitic interlayer between graphene and Cu, and (c) the corresponding Raman spectrum for samples #1 and #2 with FEBID and the pristine graphene without FEBID, showing the change of the spectrum through FEBID graphitic interlayer formation.

In order to confirm the presence of FEBID carbon interlayer and investigate its interaction with graphene, Raman analysis was performed for samples #1 and #2, using a confocal Raman spectroscopy with a 514 nm Ar^+ ion laser. Figures 5.8(a) and (b) show Raman maps for G and D peaks integrated over the spectral ranges of 1520 cm^{-1}-1680 cm^{-1} and 1300 cm^{-1}-1420 cm^{-1}, respectively. Higher contrasts (higher Raman intensity) in G and D peaks represent the presence of additional sp^2-bonded carbon and the generation of disorder by interaction between FEBID carbon and graphene [90]. The square patterns irradiated by high energy primary electrons are clearly seen in both of the Raman maps, indicating the formation of the FEBID carbon interlayers underneath the Cu squares. Figure 5.8(c) shows the change of the Raman spectrum with FEBID interlayer formation at the interface of graphene and Cu. Pristine graphene without FEBID shows high quality structure with a small peak intensity ratio for D and G peaks, I(D)/I(G)~0.28. After FEBID, the Raman spectrum significantly changed with the increased I(D)/I(G) and a peak area ratio, A(D)/A(G), for both samples #1 and #2. The higher I(D)/I(G) and A(D)/A(G) indicate an

increase of defects in graphene and presence of graphitic domains in FEBID carbon structure, respectively [46,53,85,90] Interestingly, FEBID interlayer between graphene and Cu has graphitic domains as-deposited (*i.e.* with no post-deposition treatment such as annealing), while FEBID carbon deposited on other materials, such as SiO_2 or Si, has highly amorphous structure [26,70,90].

5.2.3 Effect of primary electron beam dose on FEBID carbon interlayer formation

In order to substantiate the effect of electron beam dose on FEBID carbon interlayer formation between graphene and metal, supplementary experiments were performed following the same experimental procedure as previously described, including the following main steps: graphene transfer, graphene-metal contact preparation *via* e-beam lithography and metal evaporation, FEBID treatment and subsequent etch out of metal contacts. Figure 5.9 shows the optical images before/after Cu removal by etching for 60 min. The entire area of the left four square Cu patterns in Figure 5.9(a) were uniformly exposed to electrons with the energy of 25 keV and electron dose ranging from 2e17 to 1e19 e^-/cm^2. The right four Cu patterns were not exposed to electrons and used as a reference. As shown in Figure 5.9(b), the Cu patterns with FEBID still remained regardless of electron dose while the Cu patterns without FEBID were totally etched away. It implies that even small dose of electrons with high energy can enhance interfacial binding between graphene and metal.

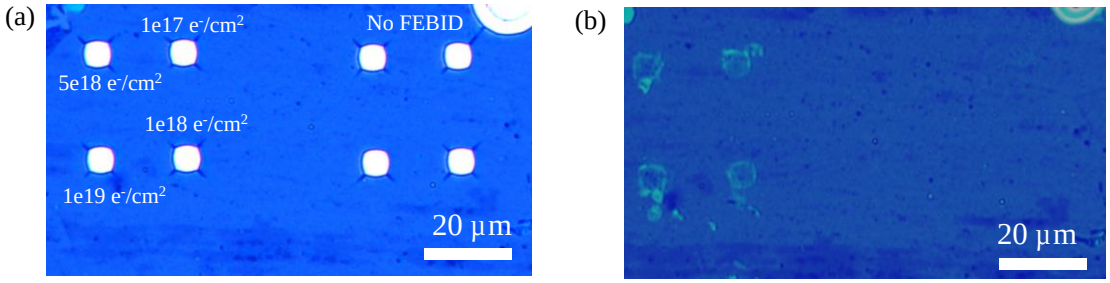

Figure 5.9. Optical microscopy images of Cu square patterns on graphene (a) before and (b) after Cu etching for 60 min. The left four Cu patterns were exposed to high energy (25 keV) electrons with varying doses, ranging from 2e17 to 1e19 e^-/cm^2.

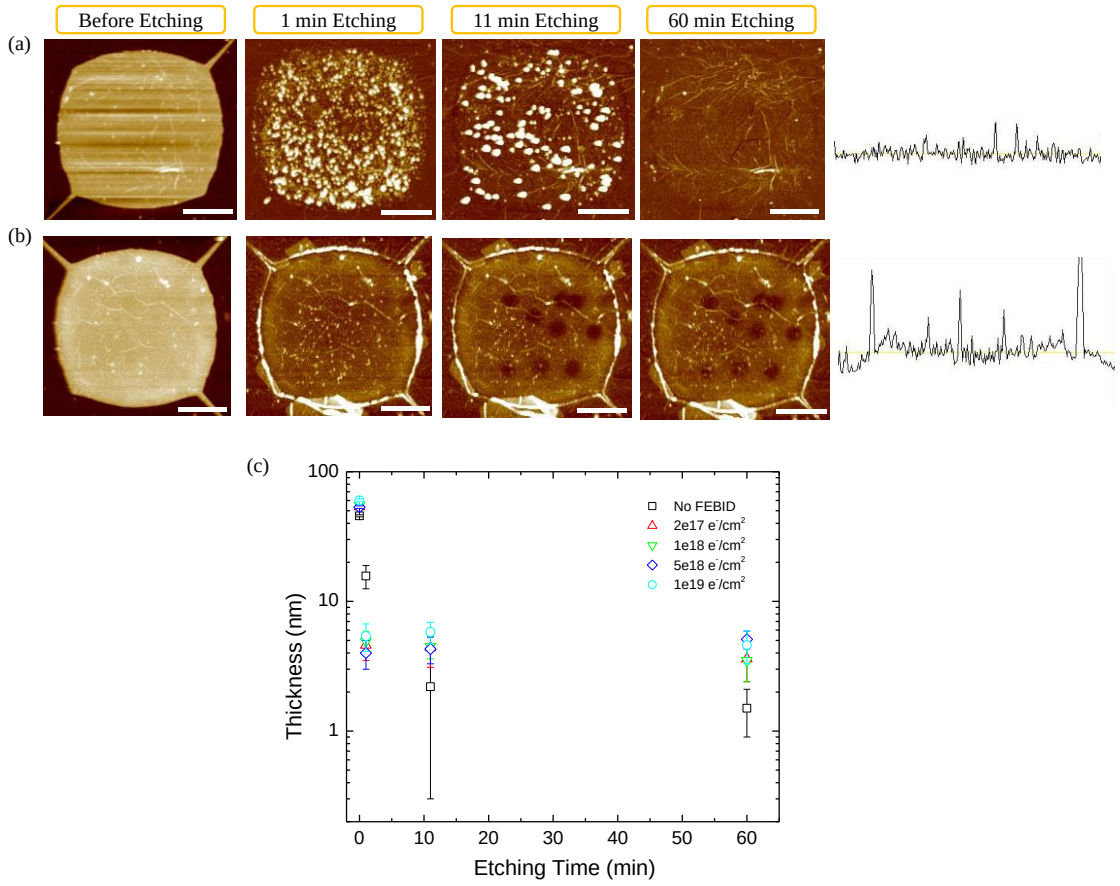

Figure 5.10. AFM images of Cu patterns on graphene (a) without FEBID and (b) with FEBID of electron dose~5e18 e^-/cm^2, showing the change of morphology of the patterns upon Cu etch time. The cross-sectional profiles after 60 min etch clearly indicate the presence of residual Cu tightly bound to graphene due to FEBID treatment. (c) Change of the thickness of the Cu patterns upon etching time as function of different FEBID electron doses. Scale bar is 2 µm.

Figures 5.10(a) and (b) show the AFM images of the Cu patterns without FEBID and with FEBID of electron dose~5e18 e^-/cm^2, respectively, upon increasing the Cu etching time. Interestingly, most (but not completely) of the Cu pattern with FEBID was uniformly removed away in a very short etching time of just 1 min and no evidence of further Cu removal was found even after 60 min at additional etching. On the other hand, the Cu pattern without FEBID treatment was anisotropically etched away with large local variation of an etching rate with complete Cu removal after 60 min of etching time. The pits shown on the Cu pattern after 11 min etching time in Figure 5.10(b) resulted from Raman measurements of the Cu pattern using a spot mode, which led to the laser-induced thermal ablation of the Cu pattern. Figure 5.10(c) shows the thickness change of the Cu patterns as function of the etch time for samples with and without FEBID treatment. The thickness of the Cu patterns with FEBID treatment reduced from initial 55.3±3.2 nm (~45 nm Cu and ~10 nm FEBID carbon on the Cu) to 4.2±0.8 nm on average for entire range of electron beam doses after 60 min etching, which indicates that a very thin Cu layer is strongly adhered to graphene *via* FEBID carbon interlayer. In contrast, the thickness of the Cu pattern without FEBID treatment reduced from initial 45.7±0.8 nm to 1.5±0.6 nm, which is the average thickness of PMMA residues remained after the e-beam lithography process prior to Cu evaporation.

Figure 5.11 shows Raman spectra indicating the impact of the electron beam dose on graphene composition with FEBID carbon interlayer formation. The Raman spectra were obtained after 11 min Cu etching to remove interfering bulk copper and expose graphene surface, using a confocal Raman spectroscopy with a 514 nm Ar^+ ion laser. Pristine graphene as transferred to the substrate shows the Raman characteristics of high quality, monolayer sp^2 carbon bonded sheet with I(D)/I(G)~0.25 and I(2D)/I(G)~2.0. After Cu deposition, the D peak intensity slightly increases, which resulted from either an exposure to a small dose of electrons during e-beam lithography or generation of atomic-scale strain on graphene lattice structure by interaction with Cu on top of graphene [91]. The Raman spectra of graphene are more significantly

influenced by exposure to high energy electrons in the course of FEBID carbon interlayer formation. A relative intensity of D peak to G peak strongly increased with electron dose of 2e17 e^-/cm^2 with appearance of D+D' peak at ~2964 cm^{-1}, which indicates generation of defects in graphene. Increasing electron dose broadened both the D and G peaks but decreased the 2D peak, which is a clear evidence of formation of FEBID carbon interlayer between graphene and Cu [46,70,90]. Decrease of the relative intensity of 2D peak to G peak occurs with defect generation and also with FEBID carbon interlayer formation [74,85,90]. 2D peak represents graphene's sp^2 hexagonal sites while G peak indicates any sp^2 sites including chains and rings [7,74,85,90]. Thus, the decrease of the relative intensity of 2D peak to G peak indicates the decrease of sp^2 hexagonal sites on graphene by the defect generation. In addition, any doping of graphene can influence the relative intensity of 2D peak to G peak *via* generation of mechanical strain in graphene's lattice structure induced by charge transfer between graphene and dopants [92-94]. Formation of FEBID carbon interlayer on graphene resulted in both the defect generation with an increase of sp^2 carbon sites from additional FEBID carbon structures (increase of G peak intensity) and doping of graphene with some amorphous carbon nanostructures weakly bound to graphene surface. Therefore, removing amorphous carbon weakly adsorbed on graphene should lead to increase of the relative intensity of 2D peak to G peak by eliminating dopants from the graphene surface. This will be shown in the next section, when explaining the effect of thermal annealing in air on removing unconstrained FEBID amorphous carbon deposit film weakly interacting with graphene.

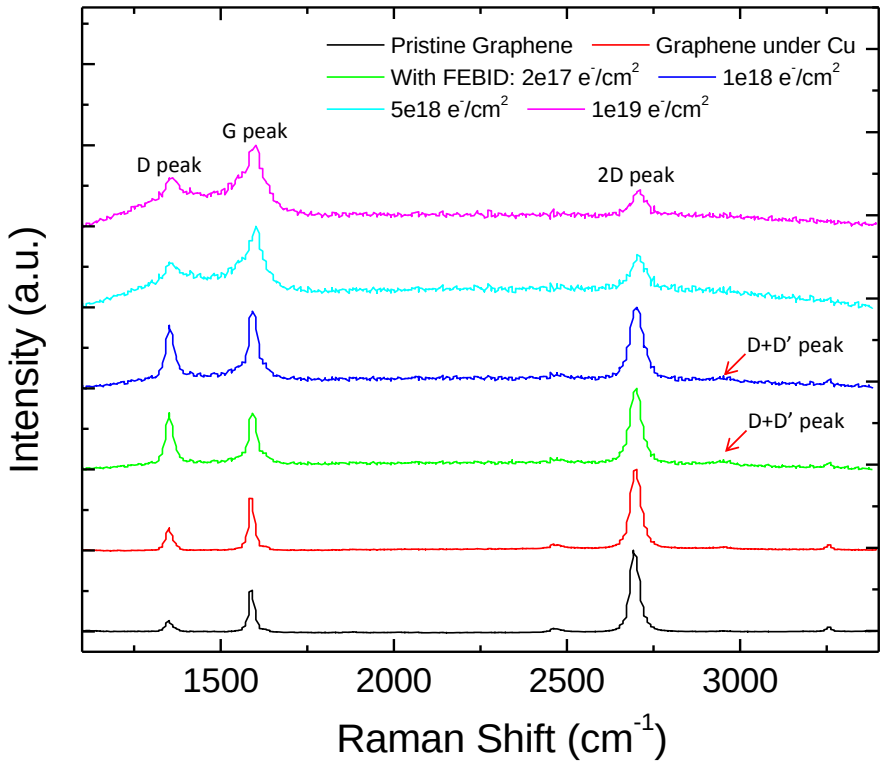

Figure 5.11. Change of the Raman spectra of graphene upon making a Cu contact and FEBID carbon interlayer formation using various electron doses from 2e17 to 1e19 e^-/cm^2.

To quantitatively demonstrate the effect of electron beam dose on the FEBID carbon interlayer formation on graphene, evolution of signature characteristics of the Raman spectra are plotted in Figure 5.12. The intensity and area ratios of D peak to G peak, denoted as I(D)/I(G) and A(D)/A(G), are shown in Figure 5.12(a). With an electron dose of 2e17 e^-/cm^2, I(D)/I(G) increased from ~0.25 to ~1.0, which represents four times higher density of defects on graphene generated by exposure to high energy electrons. The energy used for FEBID is 25 keV, which is sufficient for generation of sp^3-type defects, but less than the energy required for any other kinds of defects, such as SW defects or carbon vacancies [79-81,90]. The sp^3-type defect sites are energetically unstable, thus FEBID carbon atoms can strongly bind to these defect sites [79-81,90]. Formation of FEBID carbon atoms can be confirmed with broadening of the G peak, as shown in Figure 5.12(b). Figure 5.12(b) shows evolution of a full width half maximum (FWHM)

of G and D peaks as function of electron beam dose. Interestingly, the broadening of G peak is much more significant than that of D peak. The broadening of D peak is indicative of formation of graphitic domains (sp^2 carbon bonds in nano-sized hexagonal rings) within FEBID carbon deposits [46,53,70,90]. Thus, an increase of A(D)/A(G) is mainly due to an increase of the D peak intensity, and it can be concluded that the defect formation on graphene is more dominant than formation of graphitic domains. Increasing the electron dose to 1e18 e^-/cm^2 resulted in a decrease of I(D)/I(G) and A(D)/A(G) with the broadening of both of the G and D peaks. For treatment with this electron dose, no or negligible additional defect generation occurs on graphene with FEBID carbon deposition, which only increases and broadens the G peak, and still no significant amount of graphitic domains is formed within the FEBID carbon deposits. Above the electron dose of 5e18 e^-/cm^2, a significant increase of A(D)/A(G) is observed, while I(D)/I(G) decreases. An increase of A(D)/A(G) is due to significant broadening of the D peak, and it indicates formation of graphitic domains within the FEBID carbon deposit, featuring the amorphous structure containing the sp^2 carbon bonds in the form of rings and chains [46,53,70,90]. Further increase of the electron dose to 5e18 e^-/cm^2 does not lead to any changes in either ratio. It implies that the electron dose of 5e18 e^-/cm^2 is sufficient for FEBID graphitic interlayer formation. Figure 5.13(c) shows the G and 2D peak positions, which are indicative of doping state of graphene. Both peaks are blue-shifted with FEBID carbon interlayer formation. For defected graphene, electron doping induces a blue shift of the peak positions for G and 2D peaks from those of undoped graphene [92-94]. Thus, it can be concluded that the FEBID carbon interlayer formation leads to an n-type (electron) doping of graphene.

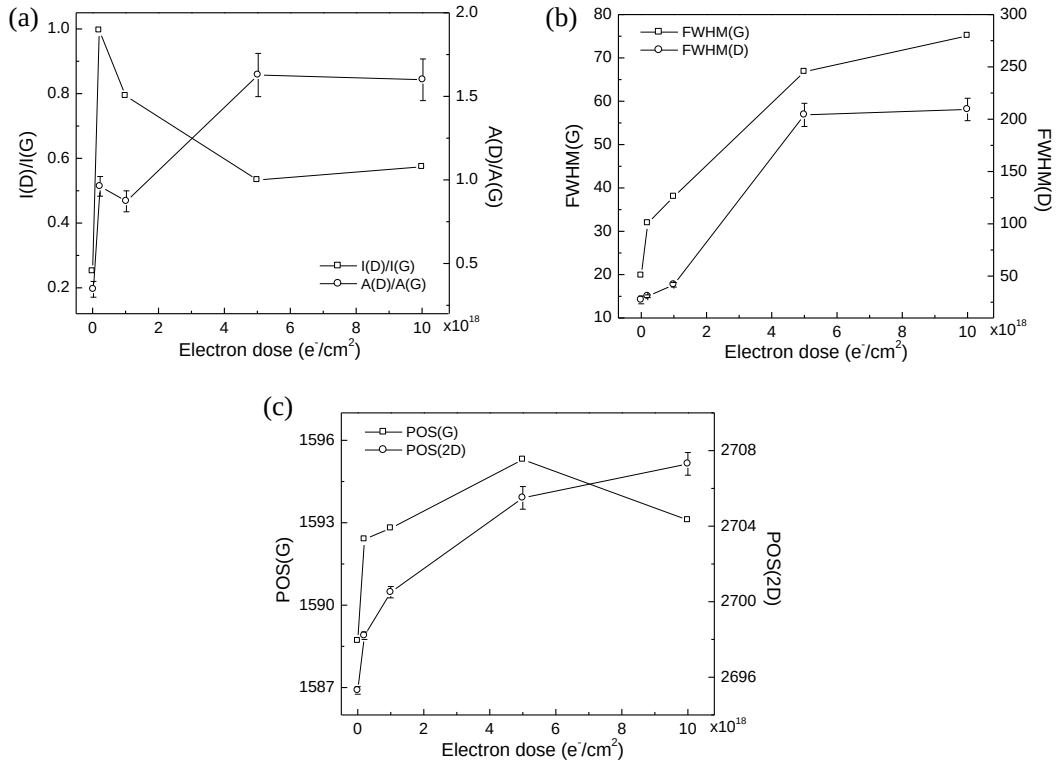

Figure 5.12. Electron dose induced evolution of signature characteristics of the Raman spectra as function of FEBID electron dose: (a) peak intensity and area ratios, I(D)/I(G) and A(D)/A(G), (b) the full width at half maximum (FWHM) of D and G peaks and (c) G and 2D peak position.

5.3 Post-deposition graphene regeneration by removing FEBID amorphous carbon structures weakly interacting with graphene

Post-deposition treatment of FEBID carbon structures, such as thermal annealing or laser-induced annealing, is critical for FEBID utility to improve interfacial properties at the graphene-metal junctions. It can accomplish complete graphitization of FEBID carbon interlayers at the graphene-metal junctions as well as remove parasitically deposited FEBID carbon contaminations on graphene exposed surface, which are weakly interacting with the base substrate of graphene. In Chapter 4, we have developed the Raman laser-induced thermal ablation technique for selective, localized cleaning of the FEBID carbon contaminants physisorbed on graphene surface without damaging graphene. Even though this technique is very efficient in removing carbon

contaminations, it is limited to a very small area, and thus troublesome in respect to cost and processing time. In contrast, thermal annealing in an environmental furnace can be more efficient for large areas and also for annealing a large number of samples at the same time, which reduces cost and processing time.

Three FEBID carbon squares were deposited on a CVD monolayer graphene supported by a SiO_2/Si substrate, using electron beam energy of 25 keV and dose of 1e19 e^-/cm^2, as shown in Figure 5.13. The carbon squares were thermally annealed in air at 250 $^\circ$C (1st annealing) and 350 $^\circ$C (2nd annealing) for 15 min each, consecutively. Figure 5.13 shows the change of morphology of the carbon squares upon thermal annealing. Thermal annealing removed parasitically deposited carbon around the squares sharpening the edges and thus, improving the patterning resolution. The changes of the average deposit volume and thickness are plotted in Figure 5.13(d) for different annealing steps. Upon thermal annealing, the volume of the deposits was reduced by ~82% after 2nd annealing. The reduction of the deposit volume is mainly due to the change of the deposit thickness which was decreased by ~72 %. It is known that dehydration and dehydrogenation of FEBID carbon deposits occur at low annealing temperatures of 100-250 $^\circ$C [46], and their graphitization can be achieved above 350 $^\circ$C with some thermal oxidation and volatilization of amorphous carbon structures [46,95]. Thus, it can be concluded that a significant reduction of the deposit volume resulted from both the thermal decomposition of hydrogen and thermal oxidation of amorphous carbon, accompanying graphitization of a carbon film strongly adhered to the graphene surface.

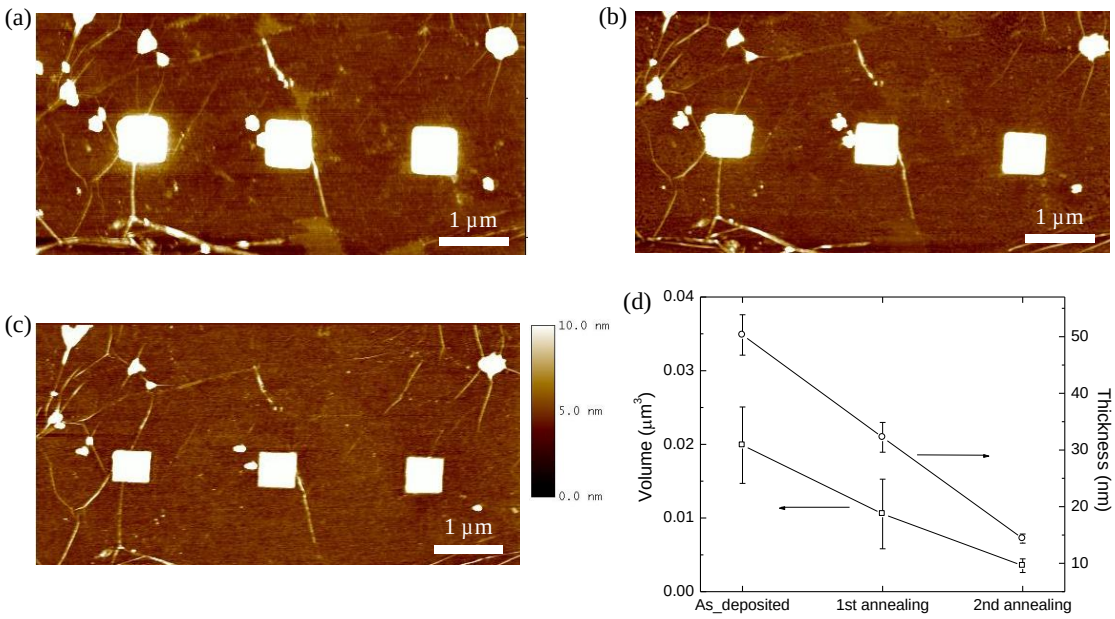

Figure 5.13. FEBID carbon squares deposited on graphene supported by a SiO_2/Si substrate: (a) as-deposited, and after thermal annealing in air at (b) 250 ˚C and (c) 350 ˚C for 15 min. (d) Change of the deposit volume and thickness upon thermal annealing.

Figure 5.14(a) shows the change of Raman spectra of FEBID carbon squares during annealing. The Raman spectrum with as-deposited FEBID carbon squares is dominated by the features of amorphous carbon with buried Raman peaks of graphene (one can hardly find a 2D peak of graphene). Thermal annealing removed unstable, thick amorphous carbon deposits by thermal oxidation and volatilization, which perturb the Raman signals from graphene. It resulted in an appearance of the 2D peak which is a Raman feature of graphene. Change of the full width at half maximum (FWHM) of the G and D peaks is shown in Figure 5.14(b). The FWHM became narrower upon thermal annealing, which indicates graphitization of FEBID carbon squares. These observations, in combination with AFM imaging of deposits, suggest that thermal annealing in air can induce graphitization of FEBID carbon deposits and also remove parasitically deposited carbon contaminants on graphene by thermal oxidation. Moreover, a relatively low annealing

temperature (350 ˚C) for graphitization of FEBID carbon interlayer is attractive in regards to its utility for processing real electronic devices.

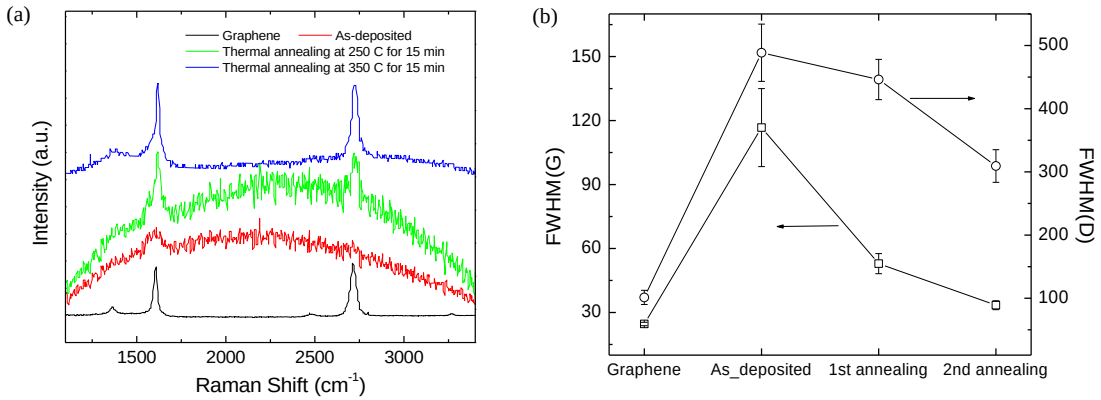

Figure 5.14. Change of (a) the Raman spectra of graphene with FEBID carbon squares and (b) the full width at half maximum (FWHM) of G and D peaks, upon thermal annealing.

5.4 Improvement of contact resistance of graphene-metal junctions using FEBID graphitic interlayer formation

In the previous sections, we demonstrated the formation of FEBID graphitic 'interlayer' between graphene and metal and modification of its interfacial properties, characterized using AFM and Raman spectroscopy. In this section, the effect of FEBID graphitic interlayer formation was investigated in application to graphene electronic devices, in order to evaluate the effect of FEBID interface modification on transport properties of graphene devices. Three-terminal (d: drain, s: source, bg: back-gate) electrical measurements (I_{ds}-V_{ds} & I_{ds}-V_{bg}) shown in Figure 5.15 were performed for all the device structures, resulting in quantitative assessment of the impact of FEBID modification of graphene-metal interface on the contact and channel resistances of graphene electronic devices.

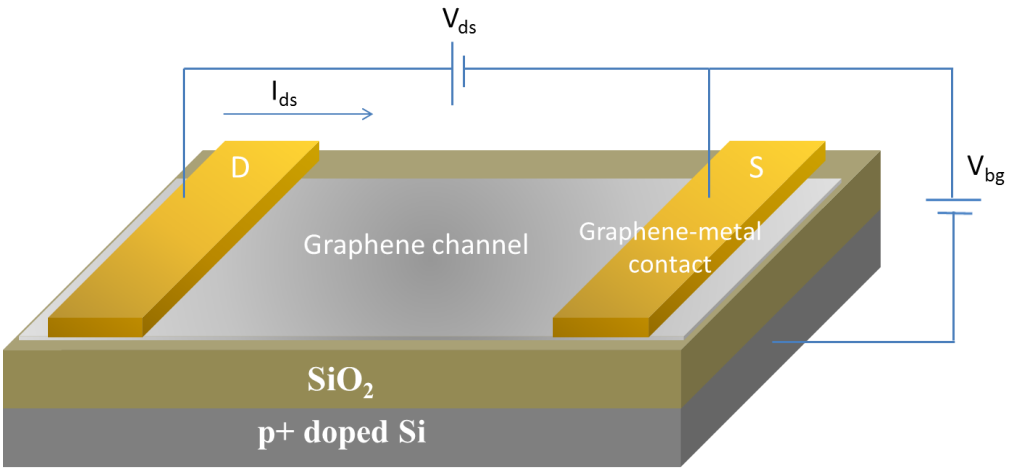

Figure 5.15. Schematic of three-terminal electrical measurements of a graphene electronic device. (V_{ds}: drain-source voltage, I_{ds}: drain-source current and V_{bg}: back-gate voltage)

5.4.1 Fabrication of graphene electronic devices for TLM measurements

CVD monolayer graphene film was transferred from the Cu foil to the 90 nm SiO_2/p-doped Si substrate, using an optimized wet transfer method described in Chapter 4.2. E-beam lithography using PMMA resist was employed to pattern the graphene film defining a 1.3 µm (width) x 70 µm (length) graphene strip, followed by oxygen plasma reactive ion etching (RIE) of graphene external to the strip. Then, the source/drain metal contacts with a contact length of ~2.6 µm were lithographically defined atop of the graphene strip, followed by deposition of 10 nm Cr/30 nm Au (metal pads) and subsequent lift-off of PMMA in a heated acetone bath at 80 ◦C. The final structure of graphene device test structure is shown in Figure 5.16. A series of the graphene interconnects with different channel lengths was developed for transmission line method (TLM) measurements to separately evaluate electrical contact and channel resistances. Each channel is defined as shown in the zoomed-in SEM image of Figure 5.16. Here, we assumed that the effect of metal contacts on transport properties in the graphene channels (marked as 'CH') for CH4~6 is negligible since the graphene channel length is much longer than the metal contact length.

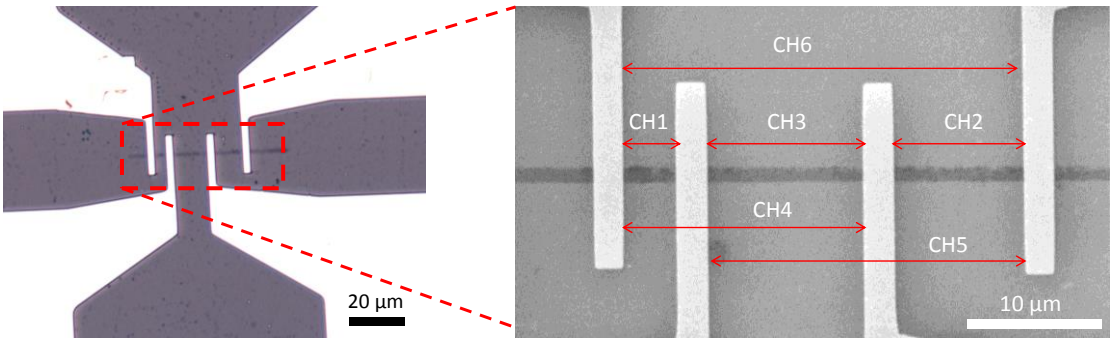

Figure 5.16. Optical microscope image of the TLM device structure with the zoomed-in SEM image describing 6 graphene channels, used for channel/contact resistance measurements.

5.4.2 Effect of FEBID carbon on transfer characteristics (R_{tot} vs. V_{bg}) and total resistance of graphene electronic devices

Monolayer graphene is a semi-metal or zero-bandgap semiconductor with conical valence and conduction bands, which thus result in the resistance change upon gate potential modulation [7,18,22]. Therefore, two-terminal electrical currents were measured by varying a back-gate voltage through a 90 nm SiO_2 dielectric layer on a p-doped Si substrate and total resistance at each gate voltage was calculated based on Ohm's law. The highest resistance (minimum conductance) occurs at the Dirac point (minimum carrier density), where the conduction and valence bands of graphene's electronic structure converge to an apex point [7,18,22,96-98]. Electron transport occurs at V_{bg}-V_{Dirac}>0 and hole transport occurs at V_{bg}-V_{Dirac}<0, where V_{Dirac} is a gate voltage with the highest device resistance (defined as 'Dirac' voltage). Physically, V_{Dirac} represents the doping state of graphene. Positive V_{Dirac} indicates that graphene is p-doped, which generally occurs when residual PMMA is adsorbed on graphene surface or when graphene strongly interacts with the SiO_2 substrate induced by thermal treatment in the course of removing PMMA residues [96]. Negative V_{Dirac} represents an n-doped graphene and can result, for example, from being exposed to focused electron beam [99].

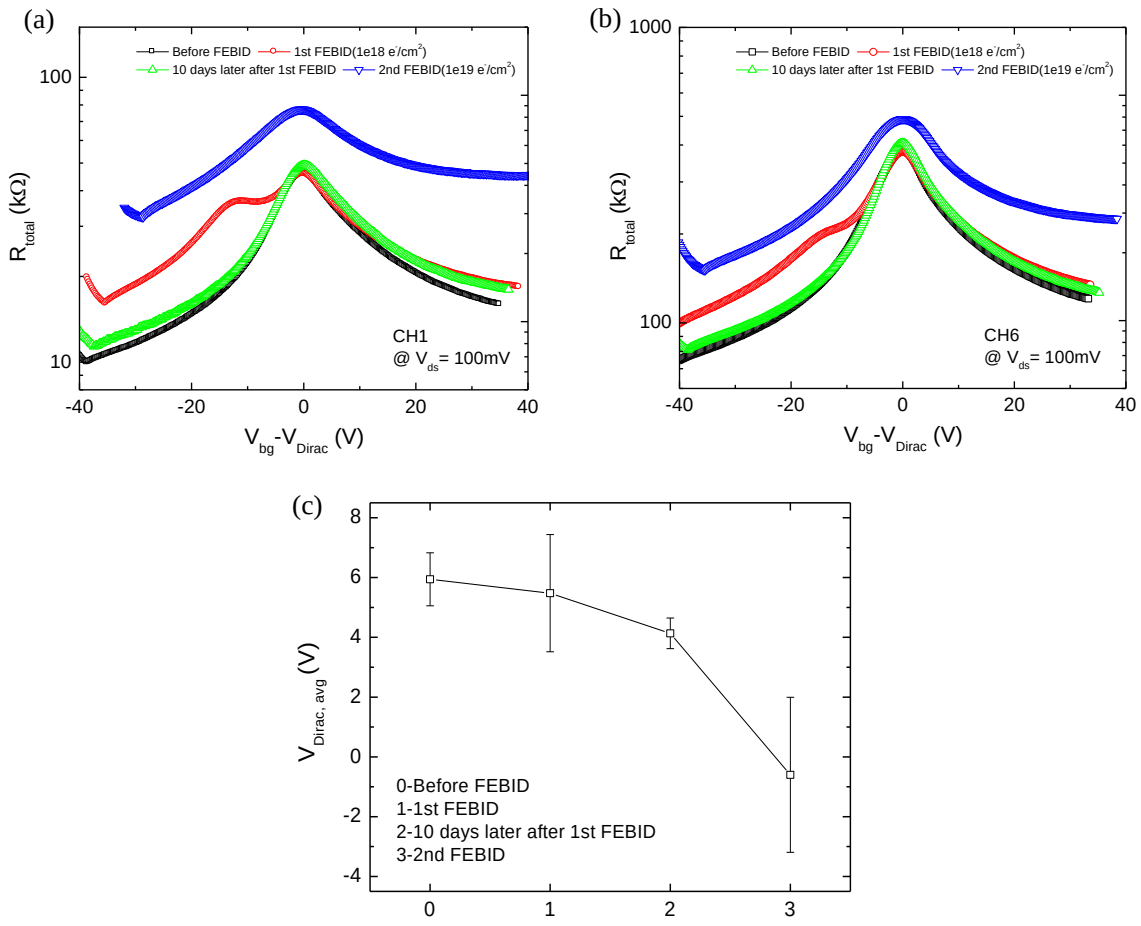

Figure 5.17. Change of the transfer characteristic (R_{tot} vs. V_{bg}-V_{Dirac}) of (a) channel #1 (CH1) and (b) #6 (CH6) with FEBID process, and (c) the averaged Dirac voltage change after FEBID process indicating n-type doping of graphene with FEBID carbon contamination on the channel.

FEBID carbon interlayer formation at graphene-metal junctions results in unintentional parasitic carbon contamination on the graphene conduction channel, which increases the device resistance. Thus, the understanding the effect of FEBID carbon contamination on the transport properties of the graphene channel is critical for FEBID utility to improve interfacial properties of the graphene-metal junctions. To this end, here, we first investigate how the carbon contamination affects the transport properties of the graphene channel. Figures 5.17(a) and (b) show the transfer characteristics of channel #1 (CH1, shortest channel length) and channel #6 (CH6, longest channel length), respectively. For FEBID carbon interlayer formation at the

graphene-metal contacts, high energy electrons (25 keV) were irradiated right on top of metal contacts, first, with electron dose of 1e18 e^-/cm^2 and, second, with the dose of 1e19 e^-/cm^2. Between 1st and 2nd FEBID steps, the test device was stored in air at a room temperature. At each stage, we performed electrical measurements and investigated the effect of FEBID conditions and carbon interlayer formation on transfer characteristics (R_{tot} vs. V_{bg}-V_{Dirac}) of the graphene device.

After 1st FEBID (low electron dose, 1e18 e^-/cm^2), a significant increase of electrical resistance can be found in the hole transport region with an additional peak at V_{bg}-V_{Dirac} ~ -13.5±0.4 V for the channel #1 (CH1) and ~ -16.3±0.5 V for the channel #6 (CH6). Two peaks in the transfer characteristics indicate the presence of two Fermi levels relative to the Dirac point energy [97]. It can occur with the p-n junction formation in the graphene channel [100,101]. As mentioned earlier, the FEBID process resulting in carbon interlayer formation at the graphene-metal contact region inevitably leads to carbon contamination on the graphene channel. It increases the device resistance due to an increase of carrier scattering sites by forming charged impurities or introducing structural defects on graphene channel. Since FEBID process focuses at the contact region, FEBID parasitic carbon contamination on the graphene channel is spatially distributed with higher density near the contact region and being decreased to the middle of the channel away from the contacts. As shown in Figure 5.17(c), graphene before FEBID is p-doped with V_{Dirac}~5.9±0.9 V due to interactions with adsorbed PMMA residues. V_{Dirac} in Figure 5.17(c) was averaged over measurements for all channels, representing the effect of each processing step on the Dirac point shift. Also, it is known that FEBID treatment can result in n-type doping of graphene [99]. Therefore, it can be expected that the graphene has n-type doping near the contact region where carbon deposition is prevalent, but p-type doping in the middle of conduction channel with minimal carbon deposition. Figure 5.18(a) shows the schematic of the device structure and its electronic band diagram, which we suggest to become established immediately after FEBID processing of graphene-metal contacts. Depending on the ratio of two length scales, $L_{n\text{-}doped}$ vs. $L_{p\text{-}doped}$ ($=L_{ch}- 2L_{n\text{-}doped}$), the electronic properties of the channel can vary. Since the

electron dose for the 1st FEBID is identical for all the channels, $L_{n\text{-}doped}$ should be the same and thus the ratio, $L_{n\text{-}doped}/L_{p\text{-}doped}$, becomes higher for the shorter channel length, which implies that the graphene channel characteristics are more strongly influenced by the n-type doped graphene region resulting from FEBID of carbon. Figure 5.18(b) shows the transfer characteristics of each channel (shown in Figure 5.16). Two peaks in Figure 5.18(b) can be found for all the channels, which represent two Fermi levels relative to the Dirac point energy. The highest peak, defined as 1st peak, is from p-type doping region, and an additional peak, defined as 2nd peak, results from n-type doping region. In order to see the effect of the channel length, the ratio of the total resistance of the 2nd peak to that of the 1st peak is plotted depending on the channel length, as shown in Figure 5.18(c). The ratio is much higher for the shortest channel length ~ 5 μm (CH1) than for any other channels, and no significant change can be found for the channel length longer than ~12 μm (CH3). It clearly demonstrates the n-p-n junction formation on the graphene channel *via* FEBID carbon contamination.

Ten days following the initial (1st) FEBID treatment, the transfer characteristics of the graphene device recovered to the state before FEBID, but the Dirac voltage, V_{Dirac}, shifted from 5.9±0.9 V to 4.1±0.5 V, as shown in Figure 5.17(c), indicative of lesser p-doping. FEBID carbon contamination on the graphene channel is deposited by low energy secondary electrons (< 50 eV), and thus carbon as-deposited has weak interaction with graphene as explained in Chapter 4. This implies that FEBID carbon atoms can migrate on the surface of graphene driven by a gradient of its chemical potential [90,102,103]. That is, due to the surface concentration of FEBID carbon varying from high near the metal contact to low at the middle of graphene channel, FEBID carbon has a driving force to diffuse towards the center of the channel and rearrange its structure. As a result, FEBID carbon is driven to become uniformly distributed on the graphene channel, forming a single-type doping state with a decrease of the effect of the PMMA-induced p-type doping on the graphene channel property. Interestingly, after 2nd FEBID (high electron dose, 1e19 e^-/cm^2), resistance for both the hole and electron transport regions increased with a significant

change of the doping state of graphene from p-type to n-type, as shown in Figure 5.17. It supports a conjecture that n-doping inducing FEBID carbon contamination becomes uniformly distributed over the graphene channel.

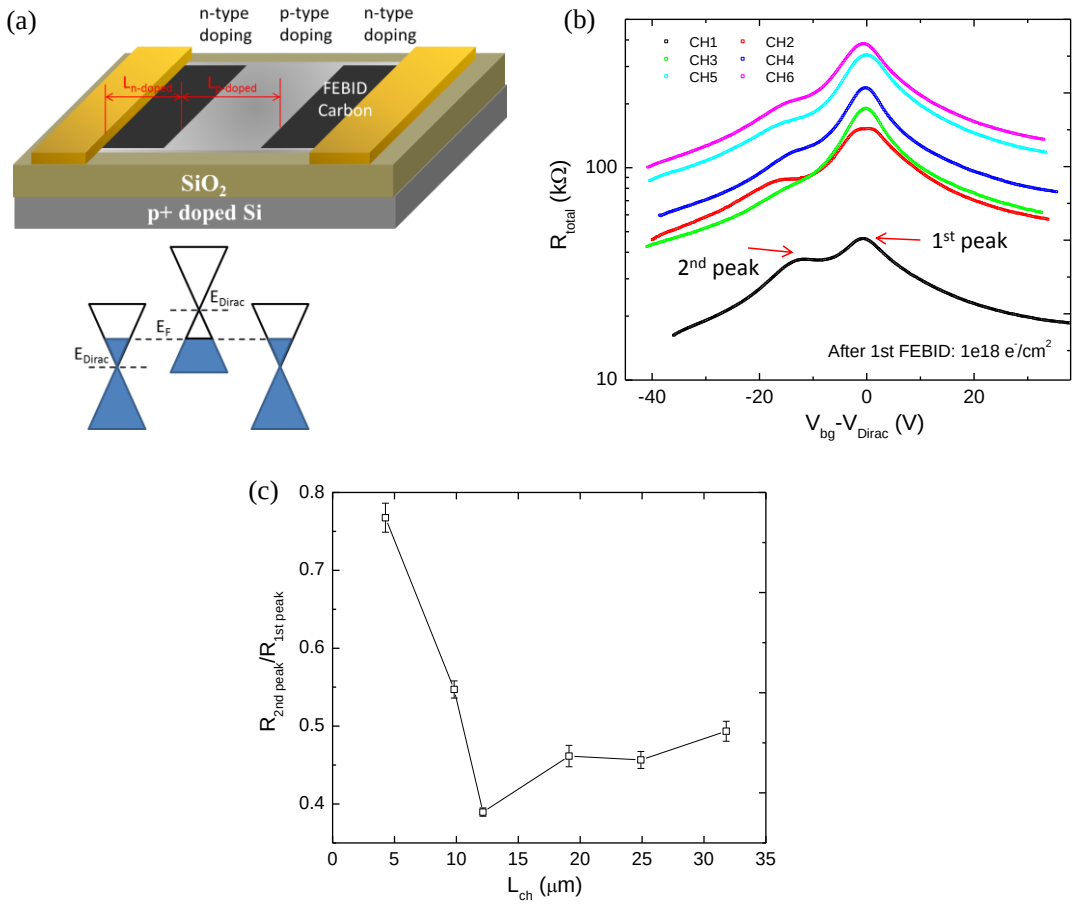

Figure 5.18. (a) Schematic of the graphene device structure and the suggested electronic band diagram immediately after FEBID process with low electron dose ~ 1e18 e^-/cm^2, showing the formation of n-p-n junction on the graphene channel. $L_{n\text{-}doped}$ is the length of the graphene channel doped by FEBID carbon (n-type doping) and $L_{p\text{-}doped}$ is the length of the graphene channel without FEBID carbon (p-type doping due to residual PMMA). (b) The change of the transfer characteristic of the graphene devices depending on the channel length showing the two peaks (1st and 2nd peaks) which is an evidence of the n-p-n junction formation. (c) The change of the ratio of the total resistance of the 2nd peak to that of the 1st peak, demonstrating the effect of the channel length on the doping state of the graphene channel and thus, confirming the formation of the n-p-n junction with FEBID carbon.

Figure 5.19 schematically summarizes the mechanism underlying an effect of FEBID carbon contamination on the graphene channel property. Initially, graphene is p-doped by PMMA residues generated from graphene transfer process or lithography steps for metal electrode fabrication. With a low electron dose~1e18 e^-/cm^2 for FEBID carbon interlayer formation, locally concentrated FEBID carbon contamination near the graphene-metal junction establishes an n-p-n junction on the graphene channel. At a room temperature, the weakly interacting (with graphene) FEBID carbon atoms diffuse towards the middle of the graphene channel due to their surface concentration gradient of carbon atoms and rearrange their structure reducing the level of graphene p-type doping. With a high electron dose~1e19 e^-/cm^2 used for FEBID carbon interlayer formation, FEBID carbon contaminates the graphene channel uniformly throughout with high surface density, and thus, resultantly, the graphene channel becomes n-type doped by substantial FEBID carbon contamination. It is worth to note that FEBID carbon contamination generated even with high electron dose is still weakly interacting with graphene, and it can be easily removed by post-deposition treatment, such as thermal annealing in air.

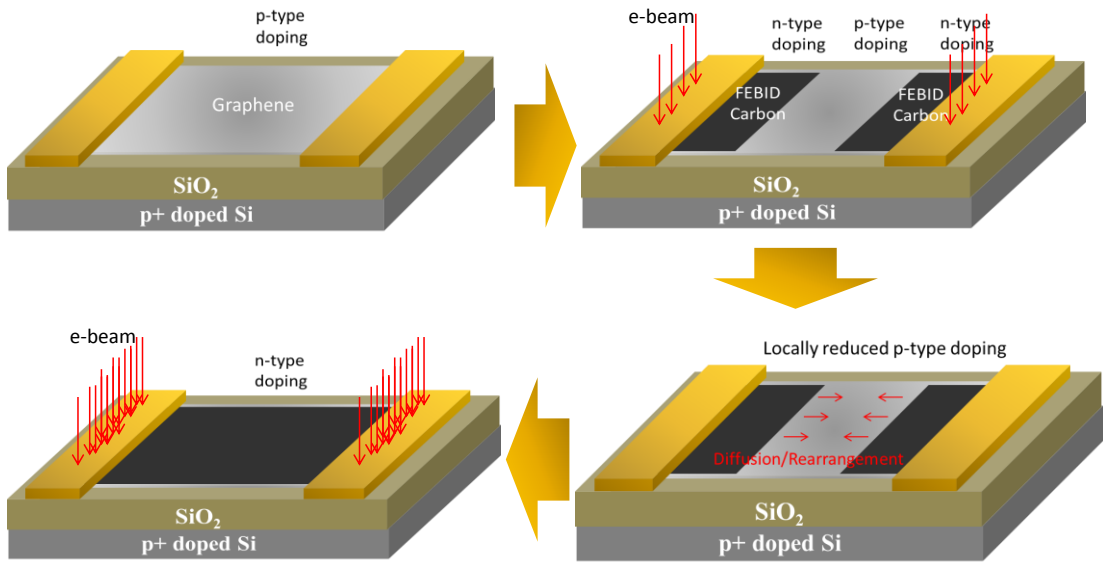

Figure 5.19. Schematics of the graphene devices, describing the change of the doping state on the graphene channel with FEBID carbon contamination in the course of carbon interlayer formation at the graphene-metal junction due to direct high energy electron beam irradiation.

5.4.3 Effect of thermal annealing on transfer characteristics and total resistance of graphene electronic devices

In order to graphitize the FEBID carbon interlayer for increasing conductivity of the interlayer and to remove the FEBID carbon contamination from the graphene channel, post-deposition thermal annealing was performed in air at 350 ˚C which is a threshold temperature for complete transformtion of FEBID amorphous carbon to nanocrystalline graphite [30,46]. Figure 5.20(a) shows the change of the transfer characteristics upon FEBID carbon interlayer formation and thermal annealing. FEBID carbon interlayer was formed at two graphene-metal junctions with the electron dose of 5e18 e^-/cm^2. As demonstrated in the previous section, FEBID carbon interlayer formation entails the carbon contamination on the channel, increasing the total device resistance, but after 13 days of device storage in unprotected (air) environment at room temperature, the transfer characteristics of the device return to the state close to that of an as-fabricated device without FEBID. After thermal annealing for 35 min, the total resistance decreases by ~47 % at V_{bg}-V_{Dirac}= 0V and by ~27% at V_{bg}-V_{Dirac}= -35V, respectively, as compared to the respective resistance of the as-fabricated device before FEBID. Thermal annealing induced a heavy p-doping of graphene due to either oxygen doping from air after annealing or interaction with the dielectric substrate, as shown in the inset of Figure 5.20. After the prolonged annealing in air at 350 ˚C up to 85 min, only a slight change in the resistance was found with the final reduction of total resistance by ~ 50% at V_{bg}-V_{Dirac}= 0V and ~31% at V_{bg}-V_{Dirac}= -35V. This indicates that the annealing time of 35 min is sufficient for complete graphitization of FEBID carbon interlayer.

For comparison, as-fabricated devices with no FEBID treatment were tested upon the same thermal annealing process, with results shown in Figures 5.21(a), (b) and (c). Figures 5.21(a) and (b) show the change of transfer characteristics (I_{ds} vs. V_{bg}-V_{Dirac}) of two different graphene devices upon thermal annealing. After thermal annealing for 35 min, the resistance in Figure 5.21(a) slightly decreased by ~29% at V_{bg}-V_{Dirac}= 0V, which might be due to the removal of

contamination on the graphene channel by thermal oxidation. However, the device resistance increased upon longer exposure to annealing conditions, which might be due to breakage of the graphene-metal junctions. The damage of the device by thermal annealing was also found in the other device as shown Figure 5.21(b). After the 1st stage of thermal annealing for 35 min, it lost graphene's intrinsic electrical characteristic (ambipolar behavior). Figure 5.21(c) shows the change of I_{ds}-V_{ds} curve at V_{bg}= -20 V. The device clearly shows an Ohmic contact behavior before annealing, but it changed to rectifying contact behavior after thermal annealing and the prolonged annealing continued to significantly increase the device resistance. It implies that the thermal annealing breaks down the interface between graphene and metal. Collectively, these observations highlight that the FEBID graphitic interlayer not only reduces the electrical contact resistance, but also improves the interfacial thermo-mechanical properties of graphene-metal contacts.

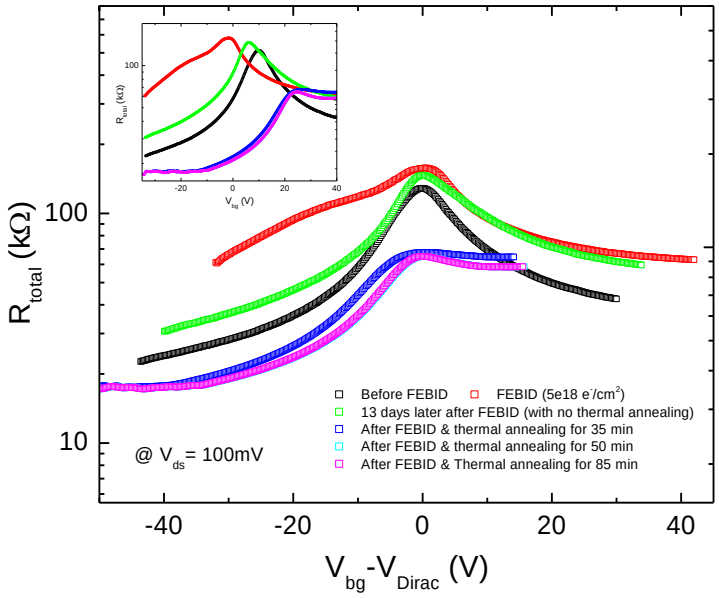

Figure. 5.20. Change of the transfer characteristics of the graphene device with FEBID treatment of contact (graphitic interlayer). The inset shows the change of the Dirac voltage, indicating that FEBID treatment induces n-type doping of graphene and thermal annealing results in heavy p-doping of graphene.

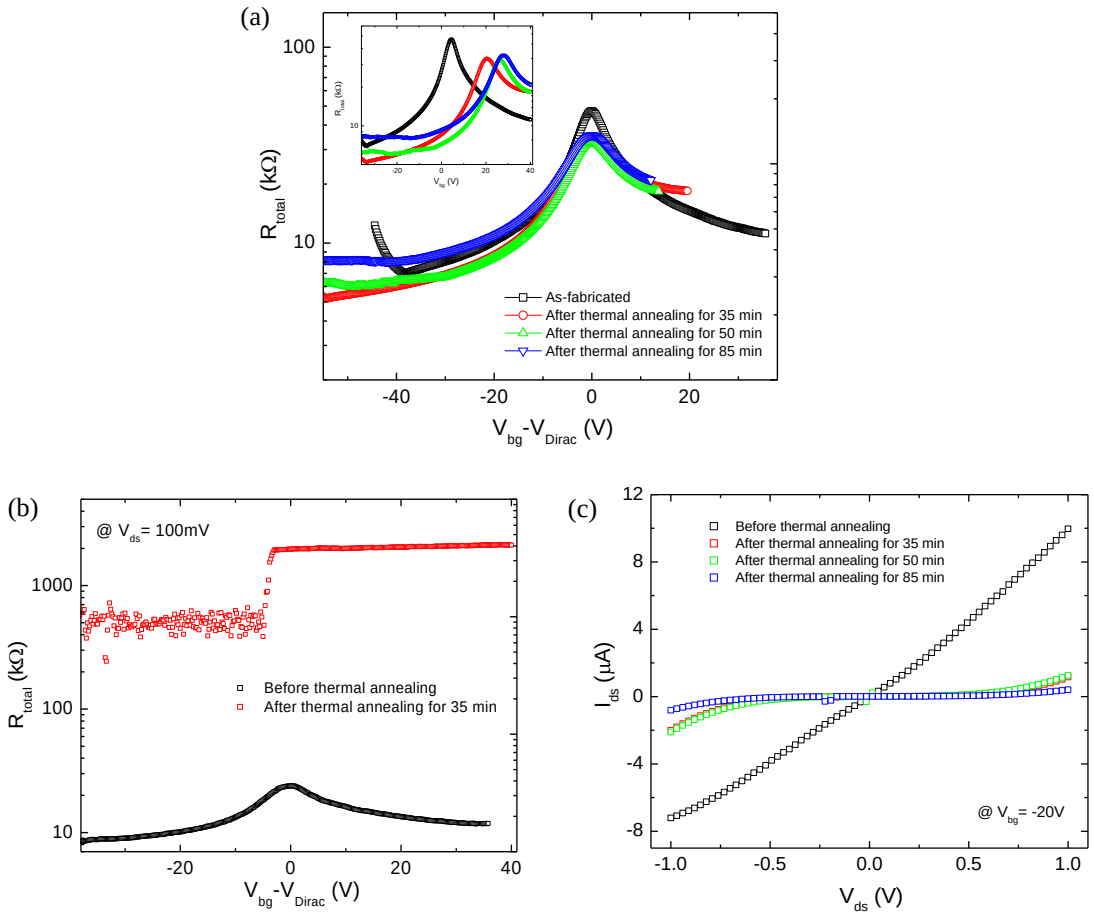

Figure. 5.21. (a)&(b) Change of the transfer characteristics of the graphene device without FEBID treatment (no graphitic interlayer). The inset of Figure 5.21(a) shows the change of the Dirac voltage, indicating thermal annealing induces heavy p-doping of graphene. (c) The change of I_{ds}-V_{ds} curve for the graphene device in Figure 5.21(b), showing degradation of the graphene-metal interface in the course of thermal annealing.

5.4.4 Effect of FEBID graphitic interlayer formation on contact and channel resistances of graphene electronic devices

In this section, we evaluate the effect of FEBID graphitic interlayer formation on contact and channel (sheet) resistances, separately, using the transmission line method (TLM) measurements. Figure 5.22 shows the results of TLM measurements for two different TLM test sets, plotted as total device resistance (R_{tot}) normalized by the contact width (W) vs. graphene channel lengths. In the TLM measurements, it is assumed that the total resistance is only affected by the channel

length and the contact resistance is identical for all channels shown in Figure 5.16, following the relation, $R_{tot}W=R_{sheet}L_{ch}+2\rho_c$, where $R_{sheet}=R_{tot}W/L_{ch}$ and $\rho_c=R_CW$ [22,55,97,104]. Thus, in the plots of $R_{tot}W$ vs. L_{ch}, the slope and the y-intercept obtained from a linear fitting indicate a channel (sheet) resistance (R_{sheet}) and twice the contact resistivity ($2\rho_c$), respectively. A goodness of the linear fitting is a measure for how reliable the TLM measurement results are, which indirectly indicates a uniformity of both the channel and contact properties over the entire set of devices involved in the TLM measurements. The TLM measurement results shown in Figure 5.22 have a goodness of linear fitting (R^2) between 0.92 and 0.99 over each process step, 'before FEBID', 'after FEBID', and 'after thermal annealing'. A strong linear relation of $R_{tot}W$ vs. L_{ch} implies that both the channel and contact electrical properties are uniform and stable upon each process step, which is essential for high quality quantitative measurements.

Figures 5.23(a) and 5.23(b) show the change of sheet and contact resistances for the TLM test sets #1 and #2, respectively. The contacts of the TLM test sets #1 and #2 were irradiated by the electron beam with the electron dose of 1e19 e^-/cm^2 and 2e19 e^-/cm^2 (total count), respectively, for FEBID carbon interlayer formation. After FEBID carbon interlayer formation, both the sheet and contact resistances increased. The contact resistance is influenced by the interfacial coupling between graphene and metal and charge carrier transmission from graphene under the metal contacts to the free-standing graphene channel [97]. The transmission efficiency is determined by the interfacial potential barrier and the minimum carrier density of states between graphene under the metal contacts and in the channel, which implies that the channel properties can also affect the contact resistance [97]. Therefore, an increase of the channel resistance due to the parasitic FEBID carbon contamination led to an increase of the contact resistance. It highlights that it is critical to remove channel contamination for reducing both channel and contact resistances. After 5 days of device storage in unprotected (air) environment at room temperature, the resistances of both the devices dropped close to those before FEBID

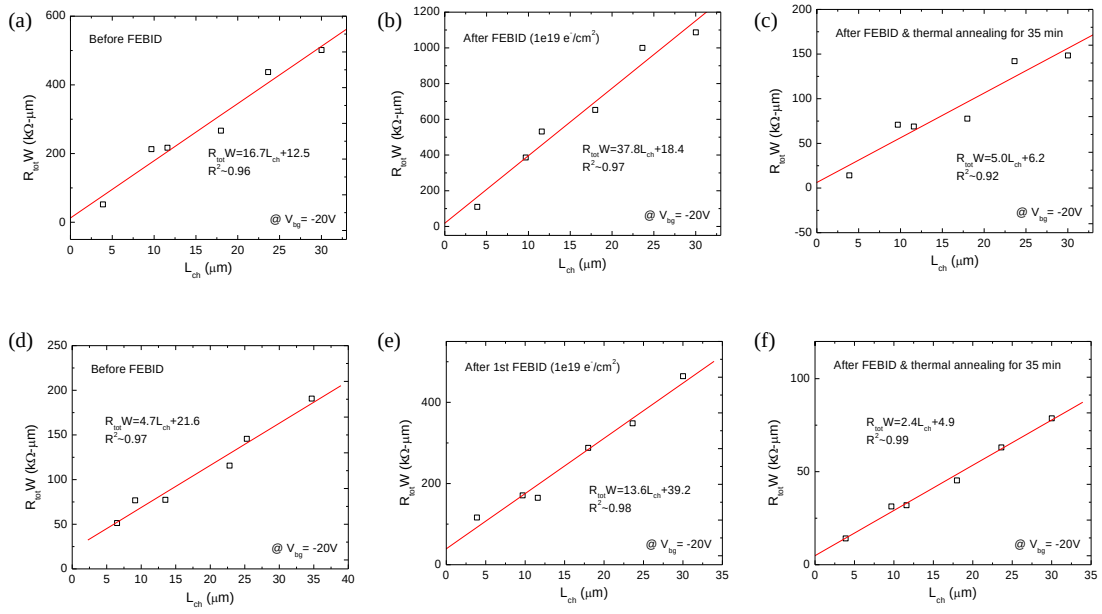

Figure 5.22. Transmission line method (TLM) measurement results for (a),(b),(c) TLM test set #1 and (d),(e),(f) TLM test set #2, before and after FEBID and after thermal annealing, respectively, showing a good linear relation between the total resistance normalized with the contact width and the channel lengths.

treatment. As demonstrated in the previous section, it occurred due to rearrangement of the parasitic FEBID carbon deposits on the graphene channel, recovering the channel and contact electrical resistances. For the TLM device #2, an additional FEBID with the electron dose of 1e19 e^-/cm^2 was performed to study the effect of the electron dose on the contact resistance.

Interestingly, after thermal annealing in air at 350 ˚C firstly for 35 min and up to 85 min, both the channel (sheet) and contact resistances become significantly reduced. It is due to removals of parasitic FEBID carbon contamination from the graphene channel and an enhanced graphene-metal electronic/mechanical coupling at the contacts *via* graphitization of the FEBID carbon interlayer. Specifically, the FEBID graphitic interlayer formation resulted in the reduction of contact resistance by ~60% from that of the as-fabricated graphene-metal contact without FEBID treatment in Figure 5.22(a), and at a higher (doubled) electron beam dose (Figure 5.22(b)), the reduction of the contact resistance was even greater, as much as ~ 80% as compared to that for the standard metal contacts before FEBID treatment.

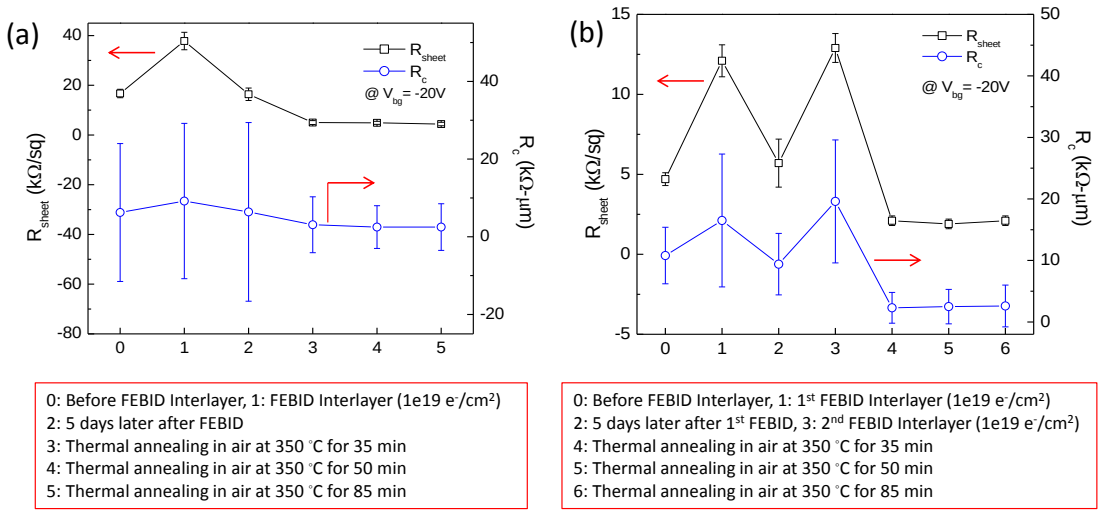

Figure 5.23. Changes in the sheet and contact resistances extracted by TLM measurements for (a) TLM test set #1 and (b) TLM test set #2, showing a significant reduction of sheet and contact resistance with formation of FEBID graphitic "interlayer" after short duration thermal annealing at 350 °C in air. No significant changes in both the sheet and contact resistances were observed after the prolonged annealing, indicating that the short time annealing ~35 min is sufficient for complete graphitization of the FEBID carbon interlayer.

5.5. Concluding remarks

In summary, we have performed a comprehensive investigation on the formation of FEBID graphitic interlayer at the interface between graphene and metal, aiming to improve the contact resistance and thermo-mechanical properties of the graphene-metal junction. Firstly, the effect of FEBID carbon interlayer formation on the binding property between graphene and Cu contacts was carefully studied using AFM and Raman spectroscopy. Measuring the change of the Cu thickness upon its removal by wet etching in ammonium persulfate/DI water solution, it was found that a very thin Cu film remained bound to graphene *via* the FEBID graphitic interlayer, while entire Cu films were completely etched away in the absence of the interlayer when no FEBID treatment was performed. The presence of the residual Cu film was confirmed by compositional analysis using EDX measurements, and the interfacial modification of the graphene-Cu contacts *via* FEBID interlayer was studied using Raman spectroscopy. Both the high

energy primary electrons and the low energy secondary electrons were found to contribute to the interlayer formation with generation of structural defects on graphene, which is indicative of strong chemical coupling between graphene and FEBID carbon interlayer. The evolution of FEBID carbon interlayer composition and chemical interactions between graphene and the graphitic carbon interlayer were assessed by Raman analysis of graphene under the Cu contacts upon exposure to various electron doses, ranging from 2e17 to 1e19 e^-/cm^2. At an initial stage of high energy electron exposure, the sp^3-type defect formation on graphene induced by chemisorption of FEBID carbon atoms is more dominant than the formation of complete FEBID carbon interlayer structures. Increasing the electron dose (thus, increasing the electron beam exposure time) results in additional FEBID carbon formation, rather than further sp^3 defect generation on graphene; and beyond the electron dose ~ 5e18 e^-/cm^2, a complete FEBID carbon interlayer was formed with apparent graphitic domains within an amorphous carbon structure.

The fabrication protocol of FEBID graphitic carbon interlayer was applied to graphene-metal junctions in order to evaluate the effect of interlayer formation on electrical transport properties of graphene devices. The FEBID process not only results in modification of the graphene-metal interface, but also impacts the electronic properties of the graphene channel by parasitic FEBID carbon. Low electron dose (1e18 e^-/cm^2) deposition leads to the non-uniform surface concentration of FEBID carbon, higher near the graphene-metal junction where the primary electron beam stroke and lower in the middle of the graphene conducting channel, forming the n-p-n junction. The weakly-coupled FEBID carbon atoms physisorbed on the graphene diffuse towards the center of the channel due to surface concentration gradient, and eventually become uniformly distributed on the channel, resulting in vanishing of a distinct n-p-n junction signature in the device transfer characteristics but producing the red shift of the Dirac voltage. Electron beam irradiation of high electron dose (1e19 e^-/cm^2) results in uniform, high density FEBID contamination over the entire graphene channel, which completely switches the doping state of the graphene channel from p-type to n-type.

Post-deposition thermal annealing of the graphene devices was conducted to graphitize the FEBID carbon interlayer at the graphene-metal contacts and remove the carbon contamination from the graphene conducting channel. The outcome was characterized by AFM and Raman spectroscopy. Thermal annealing in air at 350 $^{\circ}$C led to improvements of electrical and thermo-mechanical properties of the FEBID treated graphene-metal interface through the graphitization of the FEBID carbon interlayer, while it severely degraded the interfacial properties of as-fabricated graphene-metal contacts without the FEBID graphitic interlayer, resulting in transformation of relatively low-resistance Ohmic contacts to high-resistance rectifying junctions. Sheet and contact resistances were separately evaluated using transmission line method (TLM) measurements. Both the sheet and contact resistances were significantly reduced with FEBID graphitic interlayer after thermal annealing for 35 min, which clearly establishes the unique capability of this new interface engineering technique to improve the performance of graphene electronic devices.

CHAPTER 6

CONCLUSIONS AND RECOMMENDATIONS FOR FUTURE WORK

6.1 Summary

While carbon-based materials (CNTs and graphene) show potential as promising alternatives to conventional semiconductor materials, large contact resistance between CNTs/graphene and metal interconnects has been preventing application of these materials to functional electronic devices. Focused Electron Beam Induced Deposition (FEBID), enabling a resist-free "direct-write" additive nanomanufacturing using a variety of materials with a high degree of spatial and time-domain control, offers a unique capability to engineer MWCNT/graphene-metal interfaces with nanoscale resolution. In this Ph.D thesis, the FEBID technique is utilized to improve interfacial properties at MWCNT/graphene-metal junctions by forming graphitic nanojoints using hydrocarbon precursors. In Chapter 2, a capability of graphitized FEBID carbon to produce a low-resistance Ohmic contact connecting multiple shells of MWCNT to metal electrodes is demonstrated in the context of making high-performance electrical interconnect structure for the next generation electronic circuits. The FEBID carbon contact shape and size effects on the MWCNT-metal interconnect performance were evaluated along with the development of the low temperature (350 ℃) annealing technique for transforming initially hydrogenated amorphous FEBID carbon contacts into nanocrystalline graphite. In Chapter 3, three fabrication protocols for FEBID graphitic nanojoints, (i) 'overlayer', (ii) pre-deposited and (iii) post-deposited 'interlayers', were developed for modifying contact properties of the mechanically exfoliated multilayer graphene-metal junctions. Systematic evaluation of each fabrication protocol was performed with in-depth characterization of the resulting deposits' topological/compositional properties and device performance tests. It was demonstrated that post-metal-deposition FEBID of graphitic interlayer is the most promising approach to forming high performance graphene-

metal junctions, in combination with low temperature thermal annealing for graphitization of the carbon interlayer. In Chapter 4, an optimized transfer procedure of CVD grown monolayer graphene from a growth substrate (Cu foil) to a dielectric (device) substrate was developed in order to obtain a high quality graphene film for fabrication of high-performance graphene electronic devices. Using high quality graphene films on a dielectric support, two possible adsorption states of FEBID carbon deposits on graphene (strong chemical coupling vs. weak physical coupling) were identified theoretically and experimentally, providing insightful understanding about interactions of FEBID carbon deposits with graphene. This enabled the development of Raman laser induced thermal ablation technique to remove parasitically deposited FEBID carbon contamination from a graphene surface, which is a negative 'side-effect' of FEBID when used for processing the graphene electronic devices or FEBID patterning resolution. Lastly, in Chapter 5, formation of the FEBID graphitic interlayer at the interface of graphene and metal contacts has been investigated *via* systematic FEBID deposition experiments and complementary characterization of topological, compositional and electrical properties of the resulting interface. Notable enhancement of chemical, thermo-mechanical, and electrical interfacial properties at the graphene-metal junctions were demonstrated with use of FEBID graphitic interlayer formation. This signature result highlights a unique promise of FEBID technique as a graphene-metal contact modification tool for enhancing interfacial properties and ultimately, improving the performance of graphene electronic devices.

6.2 Major original contributions and publications

The following results are key original contributions of this work:

- Development of a novel nanomanufacturing process and quantitative operating guidelines for the FEBID-based technique to reduce contact resistance at MWCNT/graphene-metal interfaces, including multi-shell/multi-layer device structures.

- Development of fabrication protocols for low-resistance, Ohmic contact of MWCNT/graphene-metal electronic devices using FEBID-enabled interface engineering.
- Fundamental understanding of the interaction state of FEBID carbon nanostructures and the graphene's basal plane using DFT calculations and experimental validation of the theoretically predicted physical mechanism.
- Systematic assessment of topological and compositional properties of the MWCNT/ graphene-metal interface with FEBID graphitic nanojoints and their effects on the electrical properties of the interface.
- Discovery of the controls of graphene's doping states *via* FEBID carbon deposited by low energy secondary electrons, such as n-p-n junction or n-type doping formation on the graphene channel.
- First demonstration of a significant improvement of contact resistivity at the monolayer graphene-metal interface *via* formation of electron-beam-deposited graphitic interlayer.

The following publications and presentations resulted from this thesis research:

Refereed Journal Publications

- **Songkil Kim**, Michael Russell, Dhaval D. Kulkarni, Mathias Henry, Marius Chyasnavichyus, Steve S. Kim, Rajesh R. Naik, Andrey A. Voevodin, Seung Soon Jang, Vladimir V. Tsukruk, and Andrei G. Fedorov, "Controlling doping state of graphene using Focused Electron Beam Induced Deposition (FEBID)", in preparation.
- **Songkil Kim,** Dhaval D. Kulkarni, Mathias Henry**,** Seung Soon Jang, Vladimir V. Tsukruk, and Andrei G. Fedorov, "New route to reduction of graphene oxide using Focused Electron Beam Induced Deposition (FEBID)", in preparation.
- **Songkil Kim,** Michael Russell, Dhaval D. Kulkarni, Marius Chyasnavichyus, Mathias Henry, Steve S. Kim, Rajesh R. Naik, Andrey A. Voevodin, Seung Soon Jang, Vladimir V. Tsukruk,

and Andrei G. Fedorov, "Welding of graphene-metal junction *via* graphitic interlayer using Focused Electron Beam Induced Deposition (FEBID)", in preparation.

- **Songkil Kim**, Dhaval D. Kulkarni, Richard Davis, Steve S. Kim, Rajesh R. Naik, Andrey A. Voevodin, Michael Russell, Seung Soon Jang, Vladimir V. Tsukruk, and Andrei G. Fedorov, "Controlling Physicochemical State of Carbon on Graphene Using Focused Electron Beam Induced Deposition (FEBID)", *ACS Nano*, 8(7), pp. 6805-6813 (2014)
- Andrei G. Fedorov, **Songkil Kim**, Mathias Henry, Dhaval Kulkarni, and Vladimir V. Tsukruk, "Focused electron beam induced processing (FEBIP) for emerging applications in carbon nanoelectronics", *Appl. Phys. A – Mat. Sci. & Proc.*, invited, pp. 1-16 (2014)
- Dhaval D. Kulkarni, **Songkil Kim,** Marius Chyasnavichyus, Kesung Hu, Andrei G. Fedorov, and Vladimir V. Tsukruk, "Chemical reduction of individual graphene oxide sheets as revealed by electrostatic force microscopy", *J. Am. Chem. Soc.*, 136(18), pp. 6546-6549 (2014)
- **Songkil Kim**, Dhaval Kulkarni, Mathias Henry, Vladimir V. Tsukruk, and Andrei G. Fedorov, "Fabrication of an Ultra Low-Resistance Ohmic Contact to MWCNT-Metal Interconnect using Graphitic Carbon by Electron Beam Induced Deposition (EBID)", *IEEE Trans. Nanotechnol.*, 11(6), pp. 1223-1230 (2012)

  News Coverage (http://www.electroiq.com/articles/sst/2012/11/advancing-cnts-for-next-gen-chips.html)
- Dhaval Kulkarni, **Songkil Kim**, Andrei G. Fedorov, and Vladimir V. Tsukruk, "Fast light-induced phase transformations of carbon on metal nanoparticles", *Adv. Funct. Mater.*, 22, pp. 2129-2139 (2012)
- Mathias R. Henry, **Songkil Kim**, Konrad Rykaczewski, and Andrei G. Fedorov, "Inert gas jet for growth control in Electron Beam Induced Deposition", *Appl. Phys. Lett.* 98, 263109 (2011)

- Dhaval Kulkarni, Konrad Rykaczewski, Srikanth Singamaneni, **Songkil Kim**, Andrei G. Fedorov, and Vladimir V. Tsukruk, "Thermally induced transformation of amorphous carbon nanostructures fabricated by electron beam induced deposition", *ACS Appl. Mat. Interfaces*. 3, pp. 710-720 (2011)

Conference presentations

- **S.K. Kim**, D. D. Kulkarni, M. Henry, S. S. Jang, V. V. Tsukruk, and A. G. Fedorov, "Engineering of graphene-based electronic devices using FEBID", Poster presentation, *Materials Research Society Spring 2014 meeting*, San Francisco, CA, April 21-25, 2014.
- **S. K. Kim**, D. D. Kulkarni, S. Jang, M. Henry, V. V. Tsukruk, and A. G. Fedorov, "Graphitic FEBID carbon interfaces between MWCNT/graphene and metal electrodes", Poster presentation, *Materials Research Society Spring 2013 meeting*, San Francisco, CA, April 1-5, 2013.
- **S. K. Kim**, D. D. Kulkarni, K. Rykaczewski, M. R. Henry; V. V. Tsukruk, A. G. Fedorov, "Application of FEBID to Carbon Nanotube-based interconnect fabrication", Poster presentation, *4th FEBIP Workshop*, Zaragoza, Spain, Jun 20-21, 2012.

6.3 Recommendations for future work

6.3.1 Direct measurement of tunneling resistance between graphene and metal coupled *via* the FEBID graphitic interlayer

The contact resistance in graphene electronic devices includes two factors, (i) the tunneling resistance between graphene and metal contacts and (ii) the transmission resistance from the graphene under metal contacts to the graphene channel [97]. The TLM measurement results performed in this research can only give a total value of the contact resistance, which combines

contributions from both factors. Separate evaluation of the tunneling and transmission resistances would be very useful for deeper understanding of the effect of the FEBID graphitic interlayer formation on the contact resistance.

In order to make it possible, we suggest a new concept of a test structure as shown in Figure 6.1(a). Figure 6.1(b) shows the SEM image of the test structure under development with fabricated metal-graphene-metal contact for direct measurements of graphene-metal tunneling resistance. The total resistance between two (external) metal terminals can be expressed as $R_{tot}=2R_c+R_{others}$. R_{others} includes the resistances of metal electrodes and of the contact between an electrical probe tip and a metal pad. R_c should be more dominant than R_{other} for performing accurate contact (tunneling) resistance measurements. Hence, it is advisable to make a contact area as small as possible to achieve $R_{tot}\sim 2R_c$. Ultimately, such measurements can give us much better understanding for FEBID utility as a contact fabrication tool and thus, provide more control of using this technique.

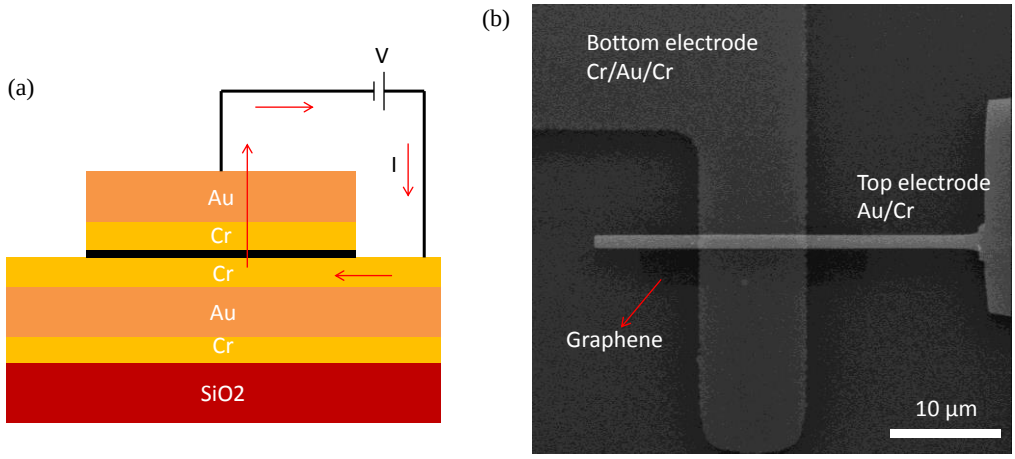

Figure 6.1. (a) Schematic of a cross section of a new test device concept, showing the electrical circuit for direct measurement of a tunneling resistance at the metal (Cr)-graphene-metal (Cr) contact and (b) SEM image of the fabricated prototype device.

6.3.2 Establishment of electrical connection to multilayers of graphene using FEBID composite Pt/C contact fabrication

Similar to connections of the multiple shells of MWCNTs to the metal electrodes, multilayers of graphene can be connected to the metal electrodes *via* FEBID composite (metal/carbon) nanojoints so that overall conductivity of graphene interconnects can increase with an increase in the number of graphene layers. FEBID composite naonjoints can be deposited introducing various precursor gases into the deposition chamber through a gas injection system integrated into the SEM machine or a custom-built injection nozzle system [105]. Figures 6.2(a) and (b) show the preliminary experiments making Pt/C 'end' contacts to monolayer graphene, deposited by injecting Pt precursor gas (Trimethyl(methylcyclopentadienyl)platinum, $C_5H_4CH_3Pt(CH_3)_3$) to the deposition substrate using a gas injection system. The EDX results shown in Figure 6.2(c) clearly demonstrate the presence of Pt in the carbon matrix with an atomic % ratio of Pt to C ~ 30%.

In order to understand the effect of the Pt/C deposition process on graphene's structure, Raman analysis was performed. Figure 6.2(d) shows the change of the intensity ratio of D to G peaks, I(D)/I(G), for the graphene channel (between two electrodes in Figure 6.2(a)) as-transferred (a large graphene film), after reactive ion etching (RIE) using oxygen to pattern the film to the strip (a region protected by the PMMA e-beam resist during RIE) and after the Pt/C deposition at the ends of the graphene strip. Interestingly, a slight decrease of I(D)/I(G) can be found after RIE, but after the Pt/C deposition, I(D)/I(G) significantly increased from ~0.2 to ~1.1, which indicates about five times higher density of defects generated after FEBID of the Pt/C deposits. The graphene channel is only exposed to low energy (< 50 eV) secondary electrons, which cannot generate structural defects [90]. Therefore, it is possible that graphene is damaged by being exposed to a high energy Pt precursor gas jet during FEBID treatment for 'end' contact fabrication.

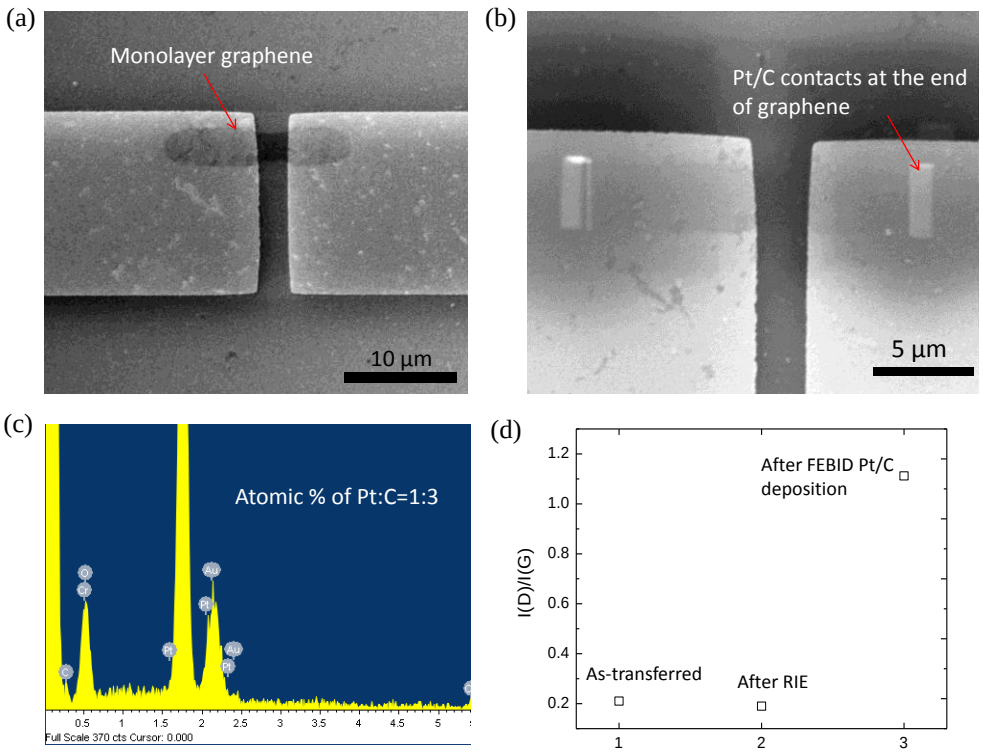

Figure 6.2. SEM images of the graphene device (a) before and (b) after FEBID Pt/C contact fabrication, connecting the ends of monolayer graphene to the metal electrodes. (c) The EDX result of the Pt/C contact showing the presence of Pt~30% and C~70% in atomic weight.

To avoid any damage of graphene, a shielding layer is required to protect graphene from a high energy precursor gas. A hexagonal boron nitride (h-BN) sheet, a two-dimensional dielectric material, can be utilized as such a shielding layer. It is expected to not only protect graphene from a precursor gas, but also separate each graphene layer when developing a multi-layer graphene channel, which is critical to maintain superior conductivity of a single layer graphene. Figure 6.3 shows a schematic of a multi-layer graphene electronic device (cross-sectional view) with FEBID composite Pt/C 'end' contacts, whose conducting channels are separated by h-BN sheets. Each layer of graphene and h-BN can be easily stacked layer by layer, using a graphene transfer procedure shown in Chapter 4. This technical advance, controllably connecting the ends of multi-layer graphene *via* the FEBID Pt/C nanojoints, should make it possible reduce the overall electrical resistance of the graphene interconnect by reducing both the contact and channel resistances. It would enable fabrication of high performance graphene-based interconnects.

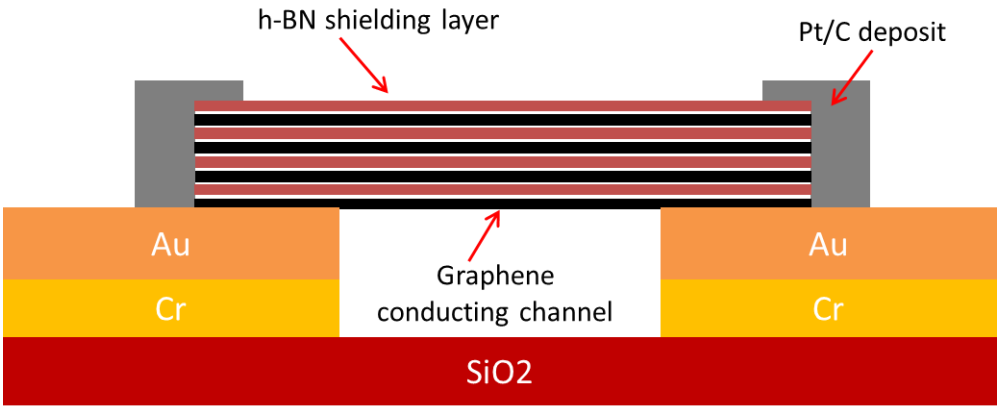

Figure 6.3. Schematic of a promising structure of a multi-layer graphene electronic device with FEBID composite Pt/C 'end' contacts, enabling reduction of the overall device resistance by decreasing both the contact and channel resistances.

APPENDIX A. Controlled assembly of MWCNT within a trench fabricated by electron beam lithography

Controlled assembly of MWCNTs into device architectures is a ground challenge for application of MWCNTs to nanoelectronics. Many studies have been performed to resolve this issue [106-111], and direct assembly of carbon nanotubes using dielectrophoresis (DEP) was found to be one of the most promising techniques due to its high controllability, low cost and suitability for large scale assembly [112]. However, there are many parameters determining an achievable yield of an individual nanotube assembly, such as MWCNT chirality, electrode geometry, AC/DC voltage levels, AC voltage frequency, dispersion solvent, and geometry of carbon nanotubes [112-115]. The diversity of control parameters resulted in a lack of consistency of an individual MWCNT assembly.

To lessen the effect of various control parameters, additional improvements were introduced by controlling the electric field generated between two metal electrodes [116,117]. For example, the use of a large (limiting) resistor placed in series allows for an automatic shut-off of the electric field across the metal electrodes once a carbon nanotube interconnect alignment is achieved [116]. Another technique is to use microwells fabricated by conventional photolithography, thereby creating concentrated electric fields to attract nanowires to the patterns bridging two metal electrodes [117]. Additional challenges include a highly flexible nature of carbon nanotubes with large variation in their length distribution in dispersion solution (thus, a variability of the required electric field that supports the tube alignment) and difficulty of creating metal electrodes/terminals with very sharp ends that produce better focusing of an electric field. For example, as shown in Figure A1, we successfully aligned a single MWCNT between two electrodes with a limiting resistor of 25 GΩ, which is much larger than resistance of a MWCNT bridging the gap between the metal electrodes (~1 GΩ). However, it was found that several

shorter MWCNTs were also attracted to the electrode side. This situation is quite typical and indicates that shorter MWCNTs can readily contaminate a designated area of assembly prior to the successful bridging of an inter-electrode space by a single long tube.

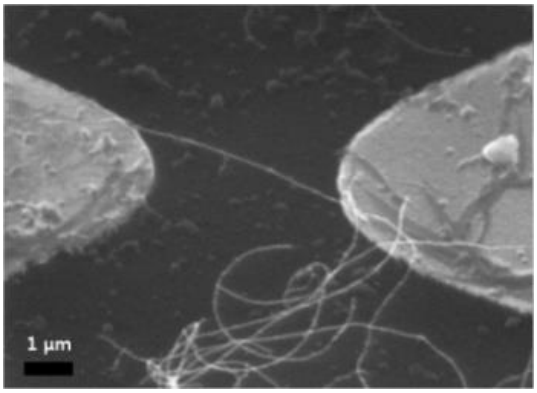

Figure A1. The SEM image of an individual MWCNT aligned using AC dielectrophoresis (DEP) with a 25 GΩ limiting resistor.

To circumvent these challenges, we developed a concept of the limiting resistor AC dielectrophoresis in combination with the electron beam lithography to align MWCNTs over multiple interconnects in an array. The test structure with 15 interconnects, as shown in Figure A2(a), was fabricated by a conventional photo- lithography with Cr/SiO_2 electrodes. The positive photoresist (PMMA) was spin-coated with 4000 rpm for 30 s on top of the prefabricated Cr electrode. Prebake at 180℃ for 90 s was used to harden the photoresist and to evaporate the solvent. The FEI Quanta 200 SEM and 'NPGS' software were used to generate the MWCNT alignment pattern. Electron beam with the spot size 3 (~30 pA and area dose of 150 $\mu C/cm^2$) and an accelerating voltage of 25 keV was used for electron beam lithography. After developing the resist with isopropanol (IPA)/ methyl-iso-butyl-ketone (MIBK) solution, 500 nm by 7 um trenches with 120 nm depth were obtained (Figure A2(b)). MWCNTs were aligned between two electrodes using the dielectrophoresis with the frequency of 5 MHz and peak-to- peak voltage of

0.5 V for 1 min. After dissolving the photoresist in acetone for 30s, the substrate was washed with DI water and dried with N_2 gas. The inset of Figure A2(b) shows MWCNT assembly before removing the photoresist. A single MWCNT is positioned within the trench connecting two electrodes and several small CNTs are on top of the photoresist. After removing the photoresist, only the MWCNTs in the trench remained, bridging the electrodes with about 50% yield of MWCNT alignment as shown in Figure A2(c).

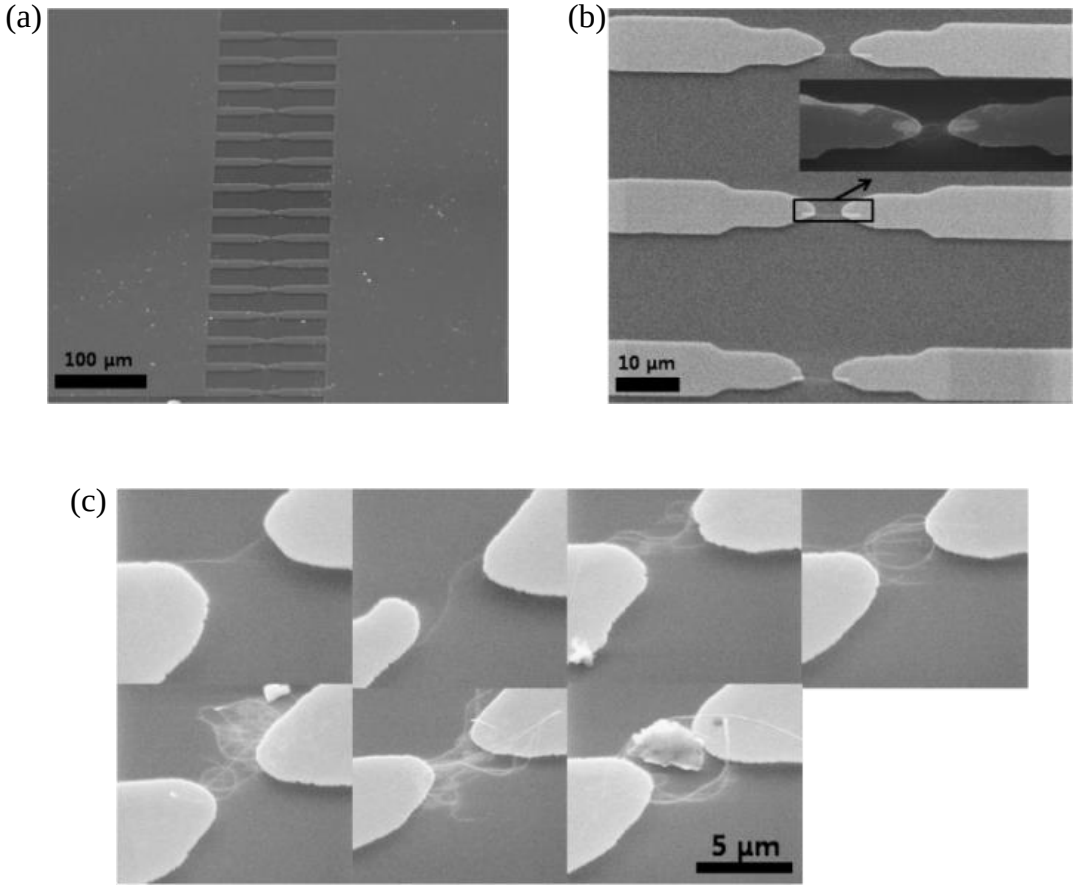

Figure A2. (a) SEM image of 15 parallel metal pads for CNT interconnect assembly. SEM images show the MWCNT assembly using a limiting resistor in combination with the electron beam lithography patterning of a trench for CNT confinement. (b) 500 nm by 7 µm trenches with 120 nm depth and the inset shows MWCNTs driven to the trenches using DEP, (c) and 50% yield of MWCNT assembly after removing the photoresist.

APPENDIX B. Exploratory work: Application of FEBID to chemical reduction of graphene oxide (GO) sheets

Graphene oxide (GO) is one of popular precursors for graphene-based devices. It features the 2D graphitic structure with surface functionalities, such as epoxide and hydroxyl species [118,119]. It is a promising material, which can be utilized for various applications owing to its unique electronic/mechanical/chemical properties [119,120]. Of specific interest to this thesis work, it can be used as a primary precursor source for high-yield, low cost production of large area graphene *via* its thermal or chemical reduction [118-121], resulting in partial removal of functional groups from its surface and a dramatic increase of conductivity. Thus, reduced graphene oxide can be applied to fabrication of large area graphene-based conductive and flexible displays or batteries [119].

There is an intriguing opportunity to modify the electronic properties of graphene oxide with application of FEBID technique, which enables the localized, high-resolution, controllable patterning of various materials. To this end, we have implemented FEBID of carbon using a hydrocarbon precursor source on graphene oxide and explored the effect of FEBID on the electronic properties of graphene oxide.

Graphene oxide was synthesized from natural graphite flakes (325 mesh, 99.8% metal basis) purchased from Alfa Aesar using the modified Hummer's method [121]. Stable dispersion of graphene oxide in a solution mixture of methanol: water (5:1) was subjected to ultrasonication for 15 mins followed by centrifugation at 3000 rpm. Then, the sheets were deposited on a 300 nm SiO_2/p-doped Si substrate using Langmuir-Blodgett (LB) method at a room temperature, using a KSV 2000 LB minitrough [121]. Figure B1(a) shows the schematic of the experimental steps used for this study. Lithographically defined source-drain contacts were established on the deposited graphene oxide sheet supported by a SiO_2/p-doped Si substrate. Focused electron beam with energy of 25 keV irradiated the center of the graphene oxide sheet. Figure B1(b) shows

graphene oxide device before and after FEBID carbon deposition on the center of the GO channel.

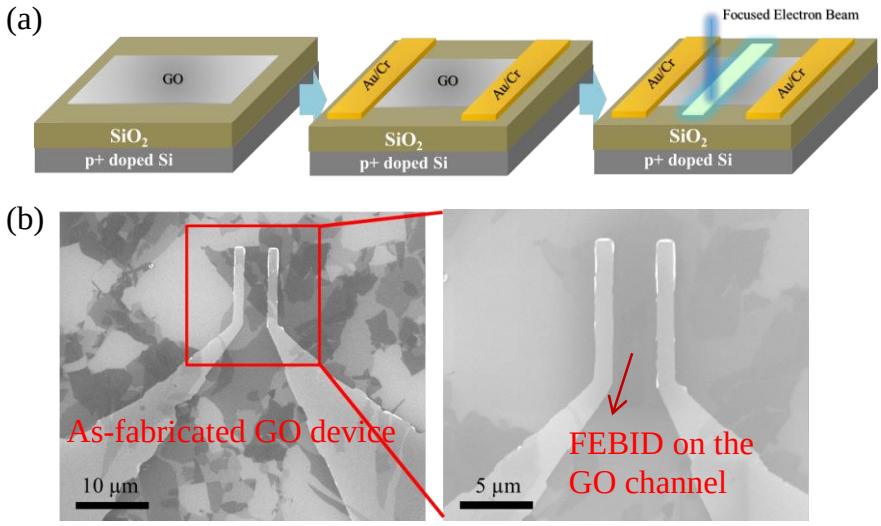

Figure B1. (a) Schematic showing the experimental steps used for studying the effect of FEBID carbon patterning on modification of the electronic properties of the graphene oxide sheet. (b) The SEM image of the as-fabricated GO device and a zoomed-in image of the device after FEBID carbon patterning at the center of the channel region.

Figure B2 shows the I_{ds}-V_{ds} characterization of the GO device, depending on electron dose in FEBID carbon deposition. The as-fabricated GO device without FEBID shows perfectly insulating behavior with no current flow at applied voltages up to ±4 V DC. After FEBID carbon patterning with a low electron dose ~ 3.4e17 e^-/cm^2, the conduction channel opened up and current started to flow through the modified GO device. Increasing the electron dose to ~4.2e18 e^-/cm^2 resulted in both the improved linearity of the I_{ds}-V_{ds} curve and a dramatic increase of current, by at least one order of magnitude. Since by itself amorphous FEBID carbon is an insulator, this implies that FEBID carbon deposition must partially reduce the graphene oxide, increasing the channel conductivity. For better understanding of this effect, density functional theory (DFT) calculations were performed for FEBID process on the surface of graphene oxide. In DFT calculations, geometry optimization of 'graphene oxide structure' and 'graphene oxide+FEBID carbon species' were implemented, using Generalized Gradient Approximation

(GGA) Perdew-Burke-Ernzerhof (PBE) functional, [64,65,76] for the exchange correlation potential of interaction electrons with double numerical basis set in the DMol3 [77]. Self-consistent field (SCF) convergence, 10^{-5} Ha, was obtained at 9x9x1 Monkhorst-Pack (MP) k-point grid [78].

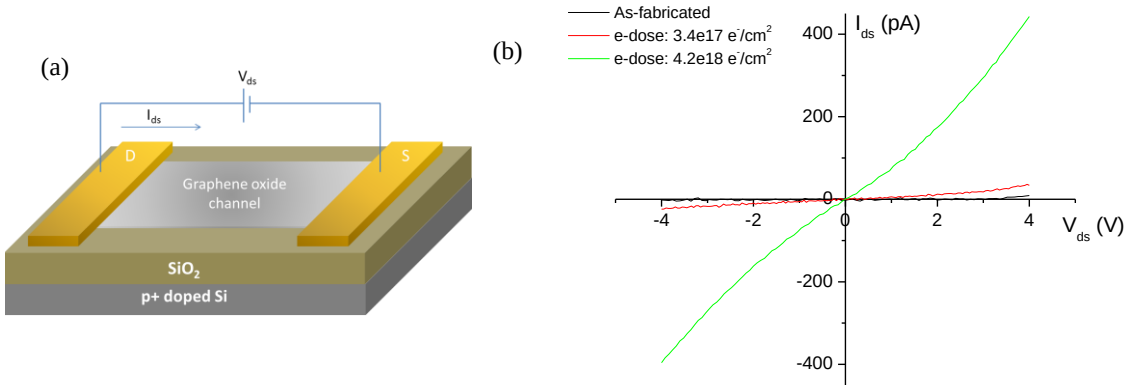

Figure B2. (a) Schematic of a device used for electrical characterization and (b) I_{ds}-V_{ds} measurements of the GO device depending on the electron dose for FEBID carbon deposition, as compared to the as-fabricated device without FEBID, indicating an increase of the channel conductivity with FEBID treatment.

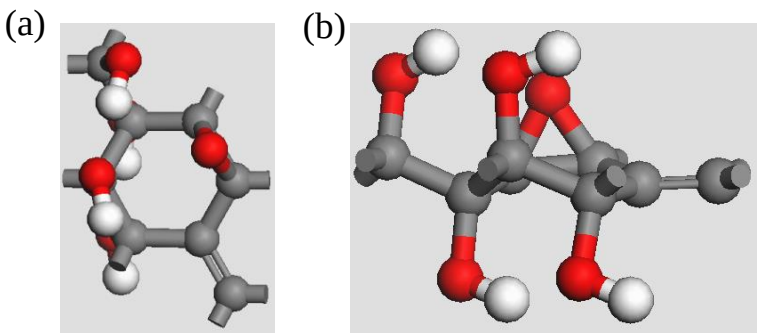

Figure B3. Graphene oxide model structure obtained by DFT calculations.

In modeling graphene oxide, only epoxide and hydroxyl species were considered as surface functionalities of graphene oxide. In this case, chemical composition of the most stable graphene oxide structure is known as $C_8(OH)_4O$ [122], whose 75% carbon atoms are oxidized, as shown in

Figure B3, and the model predictions are in a good agreement with the XPS results of graphene oxide [121]. The graphene oxide structure in Figure B3 is in the most stable state obtained by the DFT calculations starting from the random positioning of four hydroxyl groups and one epoxide group on a 2x2 supercell of graphene (eight carbon atoms). The electronic band gap of the modeled graphene oxide was calculated to be ~3.2 eV, which is in a good agreement with literature [122,123]. The electronic bandgap of materials represents their electrical characteristics, such as conductor, semiconductor or insulator. The calculated large value of the bandgap indicates that the graphene oxide is an insulator [118-123].

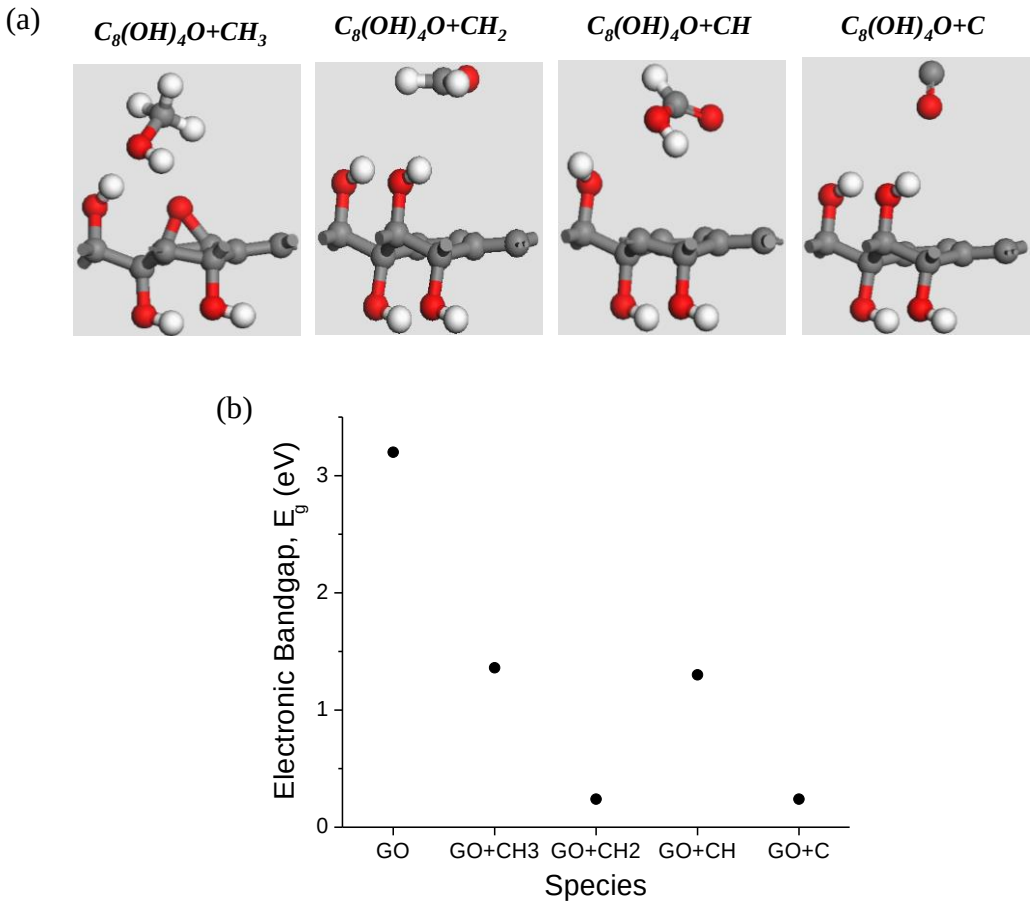

Figure B4. (a) The optimized graphene oxide structures reacting with four possible CH_4-derived intermediate species dissociated by electron beam during FEBID and (b) the corresponding electronic bandgap for each structure.

In order to describe the effect of FEBID process on the graphene oxide, we modeled four possible reactions of CH_4–derived intermediate species (possible outcomes of electron beam induced dissociation of a CH_4 precursor molecule) with the graphene oxide surface, as shown in Figure B4. Each species was randomly positioned on the surface of the graphene oxide, and the geometry optimization was implemented for each case to obtain the energetically most stable structures. Based on the calculations, all the cases have the most stable structure by removing a surface functional group from the graphene oxide and forming CH_3OH, CH_2O, CHOOH, and CO, which are weakly bound or volatile to/from the graphene oxide surface. The reduction of the electronic bandgap in Figure B4(b) indicates the change of the electrical characteristic of the graphene oxide from an insulator to a semiconductor as function of increased precursor dissociation and carbon deposition by FEBID on top of GO channel. The theoretical results supports the experimental observations of an increase of the channel conductivity by FEBID treatment with an increased irradiation dose (Figure B2) and suggests a new possible physico-chemical route for the reduction of graphene oxide by FEBID process with direct-write patterning capability on nanoscale.

REFERENCES

[1] A. Naeemi, R. Sarvari and J. D. Meindl, "Performance comparison between carbon nanotube and copper interconnects for gigascale integration (GSI)*", IEEE Electron Dev. Lett.*, vol. 26 (2), pp. 84-86, 2005.

[2] Gutmann et al., *10th Usenix Security Symposium*. Washington, D.C, 2001.

[3] Steinhogel et al., "Size-dependent resistivity of metallic wires in the mesoscopic range**",** *Physical Rev. B*, vol. 66, pp. 075414, 2002.

[4] International Technology Roadmap for Semiconductors (2011 ed. Interconnect). Available: http://www.itrs.net.

[5] R. S. Ruoff and D. C. Lorents, "Mechanical and thermal properties of carbon nanotubes", *Carbon*, vol. 33, 925-930, 1995.

[6] C. Lee, X. Wei, J. Kysar and J. Hone, "Measurement of elastic properties and intrinsic strength of monolayer graphene", *Science*, vol. 321, pp. 385-388, 2008.

[7] A. K. Geim and K. S. Novoselov, "The rise of graphene", *Nature Mater.*, vol. 6, pp. 183-191, 2007.

[8] M. S. Dresselhaus, G. Dresselhaus and P. Avouris, "Carbon nanotubes: synthesis, structure, properties, and applications", Berlin; New York, Springer, 2001.

[9] A. Naeemi and J. D. Meindl, "Compact physical models for multiwall carbon nanotube interconnects", IEEE *Electron Dev. Lett.*, vol. 27, pp. 338-340, 2006.

[10] A. D. Franklin and Z. Chen, "Length scaling of carbon nanotube transistors", *Nature Nanotechnol.* vol. 5, pp. 858-862, 2010.

[11] R. V. Seidel, A. P. Graha, J. Kretz, B. Rajasekharan, G. S. Duesberg, M. Liebau, E. Unger, F. Kreupl and W. Hoenlein, "Sub-20 nm short channel carbon nanotube transistors", *Nano Lett.*, vol. 5 (1), pp. 147-150, 2005.

[12] S. Frank, P. Poncharal, Z. L. Wang and W. A. de Herr, "Carbon nanotube quantum resistors", *Science*, vol. 280 (5370), pp. 1744-1746, 1998.

[13] H. J. Li, W. G. Lu, J. J. Li, X. D. Bai, and C. Z. Gu, "Multichannel ballistic transport in multiwall carbon nanotubes", *Phys. Rev. Lett.*, vol. 95 (8), pp. 086601, 2005.

[14] S. C. Lim, J. H. Jang, D. J. Bae, G. H. Han, S. Lee, I. S. Yeo and Y. H. Lee, "Contact resistance between metal and carbon nanotube interconnects: Effect of work function and wettability ", *Appl. Phys. Lett.*, vol. 95 (26), pp. 264103, 2009.

[15] J. Tersoff, "Contact resistance of carbon nanotubes", *Appl. Phys. Lett.*, vol. 74 (15), pp. 2122-2124, 1999.

[16] R. Pati, Y. Zhang, S. K. Nayak and P. M. Ajayan, "Effect of H_2O adsorption on electron transport in carbon nanotube", *Appl. Phys. Lett.* vol. 81 (14), pp. 2683-2640, 2002.

[17] M. S. Wang, D. Golberg and Y. Bando, "Superstrong low-resistant carbon nanotube-carbide-metal nanocontacts", *Adv. Mater.*, vol. 22 (47), pp. 5350-5355, 2010.

[18] A. D. Franklin, S.-J. Han, A. A. Bol and W. Haensch, "Effects of nanoscale contacts to graphene," *IEEE Electron. Dev. Lett.*, vol. 32 (8), pp. 1035–1037, 2011.

[19] A. D. Franklin, S.-J. Han, A. A. Bol and V. Pereveinos, "Double contacts for improved performance of graphene transistors", *IEEE Electron Dev. Lett.*, vol. 33 (1), pp. 17–19, 2012.

[20] Y. Matsuda, W. Q. Deng and W. A. Goddard, "Contact resistance properties between nanotubes and various metals from quantum mechanics", *J. Phys. Chem. C*, vol. 111, pp. 11113-11116, 2007.

[21] Y. Matsuda, W. Q. Deng and W. A. Goddard, "Contact resistance for "End-Contacted" metal-graphene and metal-nanotube interfaces from quantum mechanics", *J. Phys. Chem. C*, vol. 114, pp. 17845-17850, 2010.

[22] J. Smith, A. D. Franklin, D. B. Farmer and C. D. Dimitrakopoulos, "Reducing contact resistance in graphene devices through contact area patterning", *ACS Nano*, vol. 7 (4), pp. 3661-3667, 2013.

[23] J. Robinson, M. LaBella, M. Zhu, M. Hollander, R. Kasarda, Z. Hughes, K. Trumbull, R. Cavalero and D. Snyder, "Contacting graphene", *Appl. Phys. Lett.*, vol. 98, pp. 053103, 2011.

[24] S. J. Randolph, J. D. Fowlkes and P. D. Rack, "Focused, nanoscale electron-beam-induced deposition and etching", *Crit. Rev. Solid State Mater. Sci.*, vol. 31, pp. 55-89, 2006.

[25] W. F. van Dorp and C. W. Hagen, "A critical literature review of focused electron beam induced deposition", *J. Appl. Phys.*, vol. 104, pp. 081301, 2008.

[26] K. Rykaczewski, W. B. White and A. G. Fedorov, "Analysis of Electron Beam Induced Deposition (EBID) of residual hydrocarbons in electron microscopy", *J. Appl. Phys.*, vol. 101, pp. 054307, 2007.

[27] W. F. van Dorp, B. Someren, C. W. Hagen and P. Kruit, "Approaching the resolution limit of nanometer-scale Electron Beam-Induced Deposition", *Nano Lett.*, vol. 5, pp. 1303-1307, 2005.

[28] F. Banhart, "The formation of a connection between carbon nanotubes in an electron beam", *Nano Lett.*, vol. 1, pp. 329-332, 2001.

[29] K. Rykaczewski, M. R. Henry, S. K. Kim, D. Kulkarni, S. Singamaneni, V. V. Tsukruk and A. G. Fedorov, "Effect of Electron Beam Induced Deposited (EBID) carbon joint geometry

and material properties on electrical resistance of multiwalled carbon nanotubes (MWNT)-to-metal contact interface", *Nanotechnology*, vol. 21, pp. 0352021, 2010.

[30] S. Kim, D. D. Kulkarni, K. Rykaczewski, M. Henry, V. V. Tsukruk and A. G. Fedorov, "Fabrication of an ultralow-resistance Ohmic contact to MWCNT-metal interconnect using graphitic carbon by Electron Beam Induced Deposition (EBID)", *IEEE Trans. Nano.*, vol. 11, pp. 1223-1230, 2012.

[31] K. Hoeflich, R. B. Yang, A. Berger, G. Leuchs and S. Christiansen, "The direct writing of plasmonic gold nanostructures by Electron-Beam-Induced Deposition", *Adv. Mater.,* vol. 23, pp. 2657-2661, 2011.

[32] N. Kurra, V. S. Bhadram, C. Narayana and G. U. Kulkarni, "Field-effect transistors based on thermally treated Electron Beam-Induced carbonaceous patterns", *ACS Appl. Mater. Interfaces,* vol. 4, pp. 1030-1036, 2012.

[33] G. Boero, I. Utke, T. Bret, N. Quack, M. Todorova, S. Mouaziz, P. Kejik, J. Brugger, R. S. Popovic and P. Hoffmann, "Submicrometer hall devices fabricated by Focused Electron-Beam-Induced Deposition", *Appl. Phys. Lett.*, vol. 86, pp. 042503, 2005.

[34] L. Bernau, M. Gabureac, R. Erni and I. Utke, "Tunable nanosynthesis of composite materials by electron-impact reaction", *Angew. Chem. Int. Ed.*, vol. 49, pp. 8880-8884, 2010.

[35] I. Utke, P. Hoffmann and J. Melngailis, "Gas-assisted focused electron beam and ion beam processing and fabrication", *J. Vac. Sci. Technol. B,* vol. 26 (4), pp. 1197-1276, 2008.

[36] Y. Chai, A. Hazeghi, K. Takei, H. Y. Chen, P. C. H. Chan, A. Javey and H. S. P. Wong, "Low-resistance electrical contact to carbon nanotubes with graphitic interfacial layer", *IEEE Trans. Electron Dev.*, vol. 59(1), pp. 12-19, 2012.

[37] M. Shiraishi and M. Ata, "Work function of carbon nanotubes", *Carbon,* vol. 39 (12), pp. 1913-1917, 2001.

[38] K. Rykaczewski, A. Marshall, W. B. White and A. G. Fedorov, "Dynamic growth of carbon nanopillars and microrings in electron beam induced dissociation of residual hydrocarbons", *Ultramicroscopy,* vol. 108 (9), pp. 989-992, 2008.

[39] J. J. Palacios, A. J. Perez-Jimenez, E. SanFabian and J. A. Verges, "First-principles phase-coherent transport in metallic nanotubes with realistic contacts", *Phys. Rev. Lett.*, vol. 90(10), pp. 106801, 2002.

[40] A. G. Fedorov and K. Rykaczewski, "Electron Beam Induced Deposition of interface to carbon nanotube", U.S. Patent No. 8,207,058, 2012.

[41] T. H. P. Chang, M. Mankos, K. Y. Lee and L. P. Muray, "Multiple electron-beam lithography", *Microelectron. Eng.*, vol. 57-58, pp. 117- 135, 2001.

[42] A. Naeemi and J. D. Meindl, "Carbon nanotube interconnects", *Annu. Rev. Mater. Res.,* vol. 39, pp. 255-275, 2009.

[43] H. Li, W. Y. Yin, K. Banerjee and J. F. Mao, "Circuit modeling and performance analysis of multi-walled carbon nanotube interconnects", *IEEE Trans. Electron Dev.,* vol. 55 (6), pp. 1328-1337, 2008.

[44] T. D. Yuzvinsky, W. Mickelson, S. Aloni, G. E. Begtrup, A. Kis and A. Zettl, "Shrinking a carbon nanotube", *Nano Lett.,* vol. 6 (12), pp. 2718-2722, 2006.

[45] C. A. Santini, P. M. Vereecken, A. Volodin, G. Groeseneken, S. D. Gendt and C. V. Haesendonck, "A study of joule heating-induced breakdown of carbon nanotube interconnects", *Nanotechnology,* vol. 22 (39), pp. 395202, 2011.

[46] D. D. Kulkarni, K. Rykaczewski, S. Singamaneni, S. Kim, A. G. Fedorov and V. V. Tsukruk, "Thermally induced transformation of amorphous carbon nanostructures fabricated by Electron Beam Induced Deposition", *ACS Appl. Mater. Interfaces,* vol. 3 (3), pp. 710-720, 2011.

[47] D. Bom, R. Andrews, D. Jacques, J. Anthony, B. Chen, M. S. Meier and J. P. Selegue, "Thermogravimetric analysis of the oxidation of the multiwalled carbon nanotubes: Evidence for the role of defect sites in carbon nanotube chemistry", *NanoLett.,* vol. 2 (6), pp. 615-619, 2002.

[48] Helix materials solutions, Inc., available: www.helixmaterial.com

[49] S. Paulson, M. R. Falvo, N. Snider, A. Helser, T. Hudson, A. Seeger, R. M. Taylor, R. Superfine and S. Washburn, "In situ resistance measurements of strained carbon nanotubes", *Appl. Phys. Lett.,* vol. 75 (19), pp. 2936-2938, 1999.

[50] J. F. AuBuchon, L. H. Chen, A. I. Gapin and S. Jin, "Opening of aligned carbon nanotube ends *via* room-temperature sputter etching process", *J. Appl. Phys.,* vol. 97 (12), pp. 124310, 2005.

[51] C. H. Jin, J. Y. Wang, Q. Chen and L. M. Peng, "In situ fabrication and graphitization of amorphous carbon nanowires and their electrical properties", *J. Phys. Chem. B,* vol. 110, pp. 5423-5428, 2006.

[52] A. Callegari, D. A. Buchanan, H. Hovel, E. Simonyi and A. Marwick, "Thermal stability and electrical properties of hydrogenated amorphous carbon film", *Appl. Phys. Lett.,* vol. 65 (25), pp. 3200-3202, 1994.

[53] A. C. Ferrari and J. Robertson, "Interpretation of Raman spectra of disordered and amorphous carbon", *Phys. Rev. B,* vol. 61, pp. 14095-14107, 2000.

[54] Y. Sui and J. Appenzeller, "Screening and interlayer coupling in multilayer graphene field-effect transistors", *Nano Lett*., vol. 9 (8), pp. 2973-2977, 2009.

[55] S. M. Song, J. K. Park, O. J. Sul and B. J. Cho, "Determination of work function of graphene under a metal electrode and its role in contact resistance", *Nano Lett*., vol. 12, pp. 3887-3892, 2012.

[56] P. Avouris and C. Dimitrakopoulos, "Graphene: synthesis and applications", *Mater. Today*., vol. 15 (3), pp. 86-97, 2012.

[57] X. Liang, B. A. Sperling, I. Calizo, G. Cheng, C. Hacker, Q. Zhang, Y. Obeng, K. Yan, H. Peng, Q. Li, X. Zhu, H. Yuan, A. Walker, Z. Liu, L. Peng and C. Richter, "Toward clean and crackless transfer of graphene", *ACS Nano*, vol. 5 (11), pp. 9144-9153, 2011.

[58] X. Li, Y. Zhu, W. Cai, M. Borysiak, B. Han, D. Chen, R. Piner, L. Colombo and R. S. Ruoff, "Transfer of large-area graphene films for high-performance transparent conductive electrodes", *Nano Lett*., vol. 9 (12), pp. 4359-4363, 2009.

[59] J. C. Meyer, F. Eder, S. Kurasch, V. Skakalova, J. Kotakoski, H. J. Park, S. Roth, A. Chuvilin, S. Eyhusen, G. Benner, *et al.*, "Accurate measurements of electron beam induced displacement cross sections for single-layer graphene", *Phys. Rev. Lett.*, vol. 108, pp. 196102, 2012.

[60] J. D. Jones, K. K. Mahajan, W. H. Williams, P. A. Ecton, Y. Mo and J. M. Perez, "Formation of graphene and partially hydrogenated graphene by electron irradiation of adsorbates on graphene", *Carbon*, vol. 48, pp. 2335-2340, 2010.

[61] S. Ryu, M. Y. Han, J. Maultzsch, T. F. Heinz, P. Kim, M. L. Steigerwald and L. E. Brus, "Reversible basal plane hydrogenation of graphene", *Nano Lett.*, vol. 8, pp. 4597-4602, 2008.

[62] J. Balakrishnan, G. K. Koon, M. Jaiswal, A. H. Neto and B. Oezyilmaz, "Colossal enhancement of spin-orbit coupling in weakly hydrogenated graphene", *Nature Phys. Lett.*, vol. 9, pp. 284-287, 2013.

[63] D. C. Elias, R. R. Nair, T. M. G. Mohiuddin, S. V. Morozov, P. Blake, M. P. Halsall, A. C. Ferrari, D. W. Boukhvalov, M. I. Katsnelson, A. K. Geim, *et al.*, "Control of graphene's properties by reversible hydrogenation: Evidence for graphane", *Science*, vol. 323, pp. 610-613, 2009.

[64] E. J. G. Santos, A. Ayuela and D. Sanchez-Portal, "Universal magnetic properties of sp^3-type defects in covalently functionalized graphene", *New J. Phys.*,vol. 14, pp. 043022, 2012.

[65] D. W. Boukhvalov and M. I. Katsnelson, "A new route towards uniformly functionalized single-layer graphene", *J. Phys. D: Appl. Phys.*, vol. 43, pp. 175302, 2010.

[66] Y. G. Zhou, Z. G. Wang, P. Yang, X. T. Zu, H. Y. Xiao, X. Sun, M. A. Khaleel and F. Gao, "Electronic and magnetic properties of C-adsorbed graphene: a first-principles study", *Phys. Chem. Chem. Phys.*, vol. 13, pp. 16574-16578, 2011.

[67] C. Ataca, E. Aktürk, H. Sahin and S. Ciraci, "Adsorption of carbon adatoms to graphene and its nanoribbons", *J. Appl. Phys.*, vol. 109, pp. 013704, 2011.

[68] I. C. Gerber, A. V. Krasheninnikov, A. S. Foster and R. M. Nieminen, "A first-principles study on magnetic coupling between carbon adatoms on graphene", *New J. Phys.*, vol. 12, pp. 113021, 2010.

[69] C. H. Jin, J. Y. Wang, Q. Chen and L. M. Peng, "*In situ* fabrication and graphitization of amorphous carbon nanowires and their electrical properties. *J. Phys. Chem. B.*, vol. 110, pp. 5423-5428, 2006.

[70] D. D. Kulkarni, S. Kim, A. G. Fedorov and V. V. Tsukruk, "Light-induced plasmon-assisted phase transformation of carbon on metal nanoparticles", *Adv. Funct. Mater.*, vol. 22, pp. 2129-2139, 2012.

[71] W. F. van Dorp, X. Zhang, B. L. Feringa, T. W. Hansen, J. B. Wagner and J. Th. M. De Hosson, "Molecule-by-molecule writing using a focused electron beam", *ACS Nano*, vol. 6, pp. 10076-10081, 2012.

[72] J. C. Meyer, C. O. Girit, M. F. Crommie and A. Zettl, "Hydrocarbon lithography on graphene membranes", *Appl. Phys. Lett.*, vol. 92, pp. 123110, 2008.

[73] N. Liu, Z. Pan, L. Fu, C. Zhang, B. Dai and Z. Liu, "The origin of wrinkles on transferred graphene", *Nano Res.*, vol. 4 (10), pp.996-1004, 2011.

[74] L. G. Cancado, A. Jorio, E. H. Martins Ferreira, F. Stavale, C. A. Achete, R. B. Capaz, M. V. O. Moutinho, A. Lombardo, T. S. Kulmala and A. C. Ferrari, "Quantifying defects in graphene *via* Raman spectroscopy at different excitation energies", *Nano Lett.*, vol. 11, pp. 3190-3196, 2011.

[75] E. H. Martins Ferreira, M. V. O. Moutinho, F. Stavale, M. M. Lucchese, R. B. Capaz, C. A. Achete and A. Jorio, "Evolution of the Raman spectra from single-, few-, and many-layer graphene with increasing disorder", *Phys. Rev. B*, vol. 82, pp. 125429, 2010.

[76] J.P. Perdew, K. Burke and M. Ernzerhof, "Generalized gradient approximation made simple", *Phys. Rev. Lett.*, vol. 77, pp. 3865-3868, 1996.

[77] B. Delley, "From molecules to solids with the DMol3 approach", *J. Chem. Phys.*, vol. 113, pp. 7756-7764, 2000.

[78] W. Koh, J. I. Choi, S. G. Lee, W. R. Lee and S. S. Jang, "First-principles study of Li adsorption in a carbon nanotube-fullerene hybrid system", *Carbon*, vol. 49, pp. 286-293, 2011.

[79] F. Banhart, J. Kotakoski and A. V. Krasheninnikov, "Structural defects in graphene", *ACS Nano*, vol. 5, pp. 26-41, 2010.

[80] F. Banhart, "Irradiation effects in carbon nanostructures", *Rep. Prog. Phys.*, vol. 62, pp. 1181-1221, 1999.

[81] L. Li, S. Reich and J. Robertson, "Defect energies of graphite: Density-functional calculations", *Phys. Rev. B.*, vol. 72, pp. 184109, 2005.

[82] C. Thierfelder, M. Witte, S. Blankenburg, E. Rauls and W. G. Schmidt, "Methane adsorption on graphene from first principles including dispersion interaction", *Surf. Sci.*, vol. 605, pp. 746-749, 2011.

[83] L. Mandeltort, P. Choudhury, J. K. Johnson and J. T. Yates, "Reaction of the basal plane of graphite with the methyl radical", *J. Phys. Chem. Lett.*, vol. 3, pp. 1680-1683, 2012.

[84] M. S. Dresselhaus, A. Jorio, M. Hofmann, G. Dresselhaus and R. Saito, "Perspectives on carbon nanotubes and graphene Raman spectroscopy", *Nano Lett.*, vol. 10, pp. 751-758, 2010.

[85] A. Eckmann, A. Felten, A. Mishchenko, L. Britnell, R. Krupke, K. S. Novoselov and C. Casiraghi, "Probing the nature of defects in graphene by Raman spectroscopy", *Nano Lett.*, vol. 12, pp. 3925-3930, 2012.

[86] A. G. Fedorov, K. Rykaczewski and W. B. White, "Transport issues in focused electron beam chemical vapor deposition", *Surf. Coat. Tech.*, vol. 201, pp. 8808-8812, 2007.

[87] N. A. Roberts, J. D. Fowlkes, G. A. Magel and P. D. Rack, "Enhanced material purity and resolution *via* synchronized laser assisted electron beam induced deposition of platinum", *Nanoscale,*, vol. 5, pp. 408-415, 2013.

[88] T. Bret, S. Mauron, I. Utke and P. Hoffmann, "Characterization of focused electron beam induced carbon deposits from organic precursors", *Microelectron. Eng.*, vol. 78-79, pp. 300-306, 2005.

[89] K. N. Kudin, B. Ozbas, H. C. Schniepp, R. K. Prud'homme, I. A. Aksay and R. Car, "Raman spectra of graphite oxide and functionalized graphene sheets", *Nano Lett.*, vol. 8, pp. 36-41, 2008.

[90] S. Kim, D. D. Kulkarni, R. Davis, S. S. Kim, R. R. Naik, A. A. Voevodin, S. S. Jang, V. V. Tsukruk and A. G. Fedorov, "Controlling physicochemical state of carbon on graphene using Focused Electron Beam Induced Deposition (FEBID)", *ACS Nano*, 8(7), pp. 6805-6813, 2014.

[91] X. Shen, H. Wang and T. Yu, "How do the electron beam writing and metal deposition affect the properties of graphene during device fabrication", *Nanoscale*, vol. 5, pp. 3352-3358, 2013.

[92] C. Casiraghi, S. Pisana, K. S. Novoselov, A. K. Geim and A. C. Ferrari, "Raman fingerprint of charged impurities in graphene", *Appl. Phys. Lett*., vol. 91, pp. 233108, 2007.

[93] A. Das, S. Pisana, B. Chakraborty, S. Piscanec, S. K. Saha, U. V. Waghmare, K. S. Novoselov, H. R. Krishnamurthy, A. K. Geim, A. C. Ferrari and A. K. Sood, "Monitoring dopants by Raman scattering in an electrochemically top-gated graphene transistor", *Nature Nanotechnol*., vol. 3, pp. 210-215, 2008.

[94] M. Bruna, A. K. Ott, M. Ijas, D. Yoon, U. Sassi and A. C. Ferrari, "Doping dependence of the Raman spectrum of defected graphene", *ACS Nano*, vol. 8 (7), pp. 7432-7441, 2014.

[95] L. H. Zhang, J. P. Wang and H. Gong, "Laser and thermal induced micro-structural changes and decomposition of hydrogenated carbon films", J. Phys.: Condens. Matter, vol. 13, pp. 2989-2999, 2001.

[96] Z. Cheng, Q. Zhou, C. Wang, Q. Li, C. Wang and Y. Fang, "Toward intrinsic graphene surfaces: A systematic study on thermal annealing and wet-chemical treatment of SiO2-supported graphene devices", *Nano Lett*., vol. 11, pp. 767-771, 2011.

[97] F. Xia, V. Perebeinos, Y. Lin, Y. Wu and P. Avouris, "The origins and limits of metal-graphene junction resistance", Nature Nanotechnol., vol. 6, pp. 179-184, 2011.

[98] K. I. Bolotin, K. J. Sikes, Z. Jiang, M. Klima, G. Fudenberg, J. Hone, P. Kim and H. L. Stormer, "Ultrahigh electron mobility in suspended graphene", Solid State Commun., vol. 146, pp. 351-355, 2008.

[99] I. Childres, L. A. Jauregui, M. Foxe, J. Tian, R. Jalilian, I. Jovanovic and Y. P. Chen, "Effect of electron-beam irradiation on graphene field effect devices", *Appl. Phys. Lett*., vol. 97, pp. 173109, 2010.

[100] H. Y. Chiu, V. Perebeinos, Y. M. Lin and P. Avouris, "Controllable p-n junction formation in monolayer graphene using electrostatic substrate engineering", *Nano Lett*., vol. 10, pp. 4634-4639, 2010.

[101] H. Sojoudi, J. Baltazar, L. M. Tolbert, C. L. Henderson and S. Graham, "Creating graphene p-n junctions using self-assembled monolayers", *ACS Appl. Mater. Interfaces*, vol. 4 (9), pp. 4781-4786, 2012.

[102] T. O. Wehling, M. I. Katsnelson and A. I. Lichtenstein, "Impurities on graphene: Midgap states and migration barriers", *Phys. Rev. B*, vol. 80, pp. 085428, 2009.

[103] C. Ataca and S. Ciraci, "Perpendicular growth of carbon chains on graphene from first-principles", *Phys. Rev. B*, vol. 83, pp. 235417, 2011.

[104] L. Wang, I. Meric, P. Y. Huang, Q. Gao, Y. Gao, H. Tran, T. Taniguchi, K. Watanabe, L. M. Campos, D. A. Muller, J. Guo, P. Kim, J. Hone, K. L. Shepard and C. R. Dean, "One-dimensional electrical contact to a two-dimensional material", *Science*, vol. 342, pp. 614-617, 2013.

[105] M. R. Henry, S. Kim, K. Rykaczewski and A. G. Fedorov, "Inert gas jets for growth control in electron beam induced deposition", *Appl. Phys. Lett.*, vol. 98 (26), pp. 263109, 2011.

[106] M. Burghard, G. Duesberg, G. Philip, J. Muster and S. Roth, "Controlled adsorption of carbon nanotubes on chemically modified electrode arrays", *Adv. Mater.*, vol. 10 (8), pp. 584-587, 1998.

[107] K. Lee, M. Duchamp, G. Kulik, A. Magrez, J. W. Seo, S. Jeney, A. J. Kulik, L. Forró, R. S. Sundaram and J. Brugger, "Uniformly dispersed deposition of colloidal nanoparticles and nanowires by boiling", *Appl. Phys. Lett.*, vol. 91 (17), pp. 173112-173115, 2007.

[108] Y. C. Tseng, P. Xuan, A. Javey, R. Malloy, Q. Wang, J. Bokor and H. Dai, "Monolithic integration of carbon nanotube devices with silicon MOS technology", *Nano Lett.*, vol. 4 (1), pp. 123-127, 2003.

[109] V. V. Tsukruk, H. Ko and S. Peleshanko, "Nanotube surface arrays: weaving, bending, and assembling on patterned silicon", *Phys. Rev. Lett.*, vol. 92 (6), pp. 065502-065502, 2004.

[110] S. G. Rao, L. Huang, W. Setyawan and S. Hong, "Nanotube electronics: Large-scale assembly of carbon nanotubes", *Nature*, vol. 425, pp. 36-37, 2003.

[111] T. Fukuda, F. Arai and L. Dong, "Assembly of nanodevices with carbon nanotubes through nanorobotic manipulations", *Proc. IEEE* , vol. 91 (11), pp. 1803-1811, 2003.

[112] M. Duchamp, K. Lee, B. Dwir, J. W. Seo, E. Kapon, L. Forró and A. Magrez, "Controlled positioning of carbon nanotubes by dielectrophoresis: Insights into the solvent and substrate role", *ACS Nano*, vol. 4 (1), pp. 279-284, 2010.

[113] J. Chung, K. H. Lee, J. Lee and R. S. Ruoff, "Toward large-scale integration of carbon nanotubes", *Langmuir*, vol. 20 (8), pp. 3011-3017, 2004.

[114] R. Krupke, F. Hennrich, H. V. Löhneysen and M. M. Kappes, "Separation of metallic from semiconducting single-walled carbon nanotubes", *Science*, vol. 301 (5631), pp. 344-347, 2003.

[115] C. W. Marquardt, S. Blatt, F. Hennrich, H. V. Löhneysen and R. Krupke, "Probing Dielectrophoretic force fields with metallic carbon nanotubes", *Appl. Phys. Lett.*, vol. 89 (18), pp. 183117, 2006.

[116] S. Banerjee, B. White, L. Huang, B. J. Rego, S. O'Brien and I. P. Herman, "Precise positioning of single-walled carbon nanotubes by ac dielectrophoresis", *J. Vac. Sci. Technol. B*, vol. 24 (6), pp. 3173-3178, 2006.

[117] T. J. Morrow, M. Li, J. Kim, T. S. Mayer and C. D. Keating, "Programmed assembly of DNA-coated nanowire devices", *Science*, vol. 323 (5912), pp. 352, 2009.

[118] W. Gao, L. B. Alemany, L. Ci and P. M. Ajayan, "New insights into the structure and reduction of graphite oxide", *Nature Chem.*, vol. 1, pp. 403-408, 2009.

[119] Y. Zhu, S. Murali, W. Cai, X. Li, J. W. Suk, J. R. Potts and R. S. Ruoff, "Graphene and graphene oxide: Synthesis, properties, and applications", *Adv. Mater.*, vol. 22, pp. 3906-3924, 2010.

[120] K. Hu, D. D. Kulkarni, I. Choi and V. V. Tsukruk, "Graphene-polymer nanocomposites for structural and functional applications", *Prog. Polym. Sci.*, in press, 2014.

[121] D. D. Kulkarni, S. Kim, M. Chyasnavichyus, K. Hu, A. G. Fedorov and V. V. Tsukruk, "Chemical reduction of individual graphene oxide sheets as revealed by electrostatic force microscopy", *J. Am. Chem. Soc.*, vol. 136 (18), pp. 6546-6549, 2014.

[122] D. W. Boukhvalov and M. I. Katsnelson, "Modeling of graphite oxide", *J. Am. Chem. Soc.*, vol. 130, pp. 10697-10701, 2008.

[123] R. J. W. E. Lahaye, H. K. Jeong, C. Y. Park and Y. H. Lee, "Density functional theory study of graphite oxide for different oxidation levels", *Phys. Rev. B*, vol. 79, pp. 125435, 2009.